Internally generated circulation and variability in the tropical Atlantic Ocean

Dissertation

zur Erlangung des Doktorgrades
der Mathematisch-Naturwissenschaftlichen Fakultät
der Christian-Albrechts-Universität zu Kiel

vorgelegt von
Swantje Bastin

Kiel, 2021

Erster Gutachter: Prof. Dr. Martin Claus

Zweiter Gutachter: Prof. Dr. Peter Brandt

Tag der mündlichen Prüfung: 03.11.2021

Abstract

In the subthermocline tropical Atlantic Ocean, the circulation is dominated by strong zonal current bands which can be divided into two different current systems. The first one of these consists of the vertically alternating, downward propagating Equatorial Deep Jets (EDJ) which vary on interannual time scales, have small vertical scales of a few hundred metres and are located on the equator. The second current system is sometimes called Equatorial Intermediate Current System (EICS) and is composed of latitudinally alternating zonal jets that are quasi steady in time, have large vertical scales and extend to at least 15°S/N, although here the focus is on the central part of the EICS only which consists of mean westward equatorial flow and mean eastward flow at 2°S/N. Both the EDJ and the EICS have amplitudes of up to $25\,\mathrm{cm\,s^{-1}}$, and are thus among the most energetic ocean currents below the thermocline, after the deep flows in the Southern Ocean and along the western boundaries. Despite the fact that these zonal current systems are quite important for the transport of water masses and tracers in the subthermocline tropical ocean, and the EDJ have even been suggested to cause interannual variability in the tropical Atlantic surface climate, observations of them remain scarce, their generation and maintenance mechanisms are still not completely understood, and they remain poorly represented or absent in global general circulation models. However, they have been successfully simulated with idealised models of the tropical ocean.

This thesis investigates different dynamical and statistical aspects of the Atlantic EDJ and the central Atlantic EICS. One of these is the maintenance mechanism of the EDJ and the central EICS. It is shown that the convergence of the meridional flux of intraseasonal zonal momentum that is associated with the deformation of intraseasonal waves by the equatorial currents can maintain them against dissipation in an idealised ocean model of the tropical Atlantic. Another point that is investigated is the energy transfer between the EDJ and the central EICS. It is shown that the interannually varying EDJ nonlinearly transfer energy to the time mean currents at intermediate depth, strenghtening the central EICS in the western part of the basin and weakening or reversing it in the eastern basin. In addition, a new comprehensive analysis of the spatial and temporal scales of the Atlantic EDJ from Argo float observations is presented, which adds significantly to the available knowledge about the appearance of the Atlantic EDJ in the real ocean. Furthermore, the origin of the enhanced meridional width of the EDJ compared to their theoretically expected width is investigated in a series of idealised ocean models. It is shown that instantaneous meridional widening of the EDJ due to stronger mixing of momentum than of tracers plays a larger role than averaging over intraseasonal meandering of the EDJ.

Zusammenfassung

Im tropischen Atlantik unter der Thermokline wird die Ozeanzirkulation von starken zonalen Strömungsbändern dominiert, die sich in zwei verschiedene Strömungssysteme einteilen lassen. Das erste dieser Systeme besteht aus sich vertikal abwechselnden ost- und westwärts fließenden Strömungen mit abwärts gerichteter Phasenausbreitung, den *Equatorial Deep Jets* (EDJ). Die EDJ variieren auf interannualen Zeitskalen, haben eine vertikale Wellenlänge von einigen hundert Metern und befinden sich direkt auf dem Äquator. Das zweite tiefe zonale Strömungssystem, das *Equatorial Intermediate Current System* (EICS), besteht aus sich mit der geografischen Breite abwechselnden ost- und westwärts fließenden Strömungen, die sich durch eine große vertikale Skala auszeichnen, zeitlich konstant sind und sich bis mindestens 15°S/N erstrecken. In dieser Arbeit liegt der Fokus allerdings nur auf dem zentralen Teil des EICS, bestehend aus westwärtiger Strömung auf dem Äquator und ostwärtiger Strömung bei 2°S/N. Sowohl die EDJ als auch das EICS haben Amplituden von bis zu $25\,\mathrm{cm\,s^{-1}}$ und gehören damit zu den stärksten Ozeanströmungen unter der Thermokline, nach den tiefen Strömen im südlichen Ozean und den tiefen westlichen Randströmen. Obwohl die EDJ und das EICS sehr wichtig für den Transport von Wassermassen und z.B. Sauerstoff sind und sogar vermutet wird, dass die EDJ interannuale Variabilität in der tropischen Atmosphäre antreiben, sind Messungen der Strömungen bis jetzt selten und ihre Entstehungs- und Erhaltungsmechanismen sind noch nicht vollständig verstanden. Globale Ozeanmodelle haben bis heute Schwierigkeiten, die EDJ und das EICS zu simulieren. Allerdings gibt es idealisierte Modelle der tropischen Ozeane, mit denen die Strömungen erfolgreich simuliert werden können.

In dieser Arbeit werden verschiedene dynamische und statistische Aspekte der EDJ und des zentralen EICS im Atlantik untersucht. Einer davon ist die Energieversorgung der Strömungen, die sie trotz Dissipation aufrechterhält. Es wird gezeigt, dass die Konvergenz des meridionalen Flusses von intrasaisonalem zonalem Impuls, die mit der Verformung intrasaisonaler Wellen durch die untersuchten Strömungen einhergeht, die Strömungen in einem idealisierten Ozeanmodell aufrechterhalten kann. Außerdem wird der Energietranfer zwischen EDJ und EICS untersucht. Es wird gezeigt, dass die EDJ nichtlinear Energie auf die zentralen Strömungen des EICS übertragen und sie dadurch im westlichen Teil des Atlantiks verstärken, sie aber im östlichen Atlantik abschwächen oder sogar umkehren. Des Weiteren wird eine neue umfassende Analyse der räumlichen und zeitlichen Skalen der atlantischen EDJ vorgestellt, die auf Messungen von Argo-Driftbojen beruht. Die Ergebnisse tragen wesentlich zum vorhandenen Wissen über das Erscheinungsbild der EDJ im Atlantik bei. Zusätzlich wird der Ursprung der meridionalen Breite der EDJ, die größer ist als theoretisch erwartet, in einer Reihe von idealisierten Ozeanmodellen erforscht. Es wird gezeigt, dass die instantane Verbreiterung der EDJ, die durch stärkere Vermischung von Impuls als von Dichte hervorgerufen wird, eine größere Rolle spielt als das Mitteln über intrasaisonales Mäandern der EDJ.

Contents

1 Introduction

This thesis is about the energetic zonal current systems at intermediate depths in the equatorial Atlantic Ocean, in particular the Equatorial Deep Jets (EDJ) and the central part of the Equatorial Intermediate Current System (EICS). Both of these zonal current systems have instantaneous amplitudes of up to $25\,\mathrm{cm\,s^{-1}}$ and are thus among the most energetic currents at intermediate depths in the world oceans, with only the deep currents in the Southern Ocean and along the western boundaries flowing faster (e.g. Ascani et al., 2010).

This chapter provides first an overview of the general circulation, mean state and variability in the tropical Atlantic Ocean where the EDJ and the EICS are located (Section 1.1). In Section 1.2, the Atlantic EDJ are described in detail, as well as theories on their dynamics and their importance for tracer transport and tropical Atlantic surface climate. This is followed by a description of the EICS and their dynamics in Section 1.3. Section 1.4 then provides a list of research questions answered by this thesis, and how this contributes to improved understanding of the deep zonal current systems in the tropical Atlantic Ocean.

1.1 The tropical Atlantic Ocean

The tropics are of large importance for the global climate system, because there the earth's radiative heat budget shows a net heat gain which has to be balanced by atmospheric and oceanic heat transport towards the polar latitudes which are characterised by a net radiative heat deficit (cf. e.g. Gill, 1982, Fig. 1.1). The Atlantic Ocean is special in that regard, because it is home to a meridional overturning circulation (MOC) that transports heat northward throughout the entire Atlantic, unlike in the other two oceans where the net heat flux is directed polewards in both hemispheres (Behera et al., 2013). The Atlantic MOC manifests itself in surface and deep western boundary currents in the tropical ocean (e.g. Behera et al., 2013; Schott et al., 2003). In addition, a large part of the tropical Atlantic ocean circulation is driven by the easterly trade winds of the atmospheric Hadley cell that lead to strong zonal current bands in the surface and thermocline layers around the equator. A dynamical peculiarity of the equatorial ocean is of course the vanishing Coriolis parameter, which makes the equator act as a waveguide for Kelvin waves, Rossby waves, mixed Rossby-gravity or Yanai waves and gravity waves (Gill, 1982). In the following, some of the most important features of the tropical Atlantic Ocean circulation, mean state and variability will be described.

1.1.1 Large scale surface circulation and climate modes

The circulation in the surface layer of the tropical Atlantic Ocean is shown schematically by the solid arrows in Figure 1.1. Towards the north and south, the tropical circulation is bounded by the

equatorward flanks of the subtropical gyres in both hemispheres (Talley et al., 2011). These are the westward flowing North Equatorial Current (NEC) and South Equatorial Current (SEC). The SEC is not limited to the Southern Hemisphere, but actually extends across the equator into the Northern Hemisphere, including westward flow directly on the equator that is driven by the easterly trade winds. Between the SEC and NEC, the winds associated with the Intertropical Convergence Zone (ITCZ) force the strong eastward flowing North Equatorial Countercurrent (NECC, Talley et al., 2011).

The seasonal migration of the ITCZ and the associated variation in strength of the equatorial easterly trade winds lead to a strong seasonal cycle particularly in the upper ocean. In general, the easterly trade winds push the equatorial surface water westward, leading to warmer sea surface temperature (SST) and a deeper thermocline in the western part of the tropical Atlantic basin, and colder SST and a shallower thermocline in the eastern part. The zonal pressure gradient associated with this drives the eastward Equatorial Undercurrent (EUC) at the depth level of the thermocline, shown as a dashed arrow in Figure 1.1. The EUC can reach flow velocities of almost $1\,\mathrm{m\,s^{-1}}$, and is thus one of the strongest currents in the world oceans (e.g. Brandt et al., 2021). These processes are amplified in boreal spring and summer, when the ITCZ moves northwards, leading to strong vertical shear between the intensified surface westward flow and the likewise intensified eastward EUC below. The associated diapycnal mixing causes a cooling of the equatorial surface ocean in the central and eastern part of the tropical Atlantic, leading to the emergence of the Atlantic cold tongue in boreal summer (Behera et al., 2013; Hummels et al., 2014). The cold tongue can be seen in the colour shading in Figure 1.1, where a region of relatively cold SST extends from the eastern boundary into the basin along the equator.
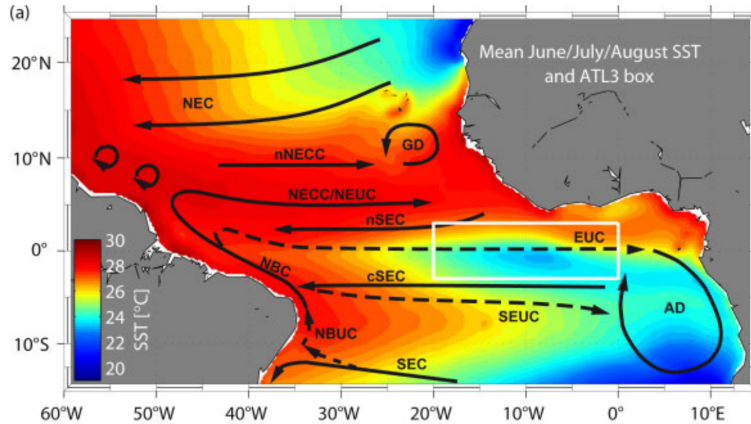
Figure 1.1: Mean boreal summer sea surface temperature (SST, colour shading) and schematic of the surface currents (solid lines) and thermocline currents (dashed lines) in the tropical Atlantic Ocean. The current bands shown in the figure are: North Equatorial Current (NEC), North Equatorial Undercurrent (NEUC), North Equatorial Countercurrent (NECC) with northern branch (nNECC), Equatorial Undercurrent (EUC), South Equatorial Current (SEC) with northern branch (nSEC) and central branch (cSEC), South Equatorial Undercurrent (SEUC), North Brazil Current (NBC), North Brazil Undercurrent (NBUC), and cylonic circulations around the Guinea Dome (GD) and Angola Dome (AD). *From Brandt et al. (2011a).*

In addition to the strong seasonal cycle, the upper tropical Atlantic Ocean also varies on interannual time scales, although contrary to the tropical Pacific the interannual variations are small compared to the seasonal variations in the Atlantic. There are two main modes of interannual coupled

atmosphere-ocean variability in the tropical Atlantic that together are referred to as Tropical Atlantic Variability (TAV): the zonal mode, and the meridional mode (Behera et al., 2013). The zonal mode of the TAV is often called Atlantic Niño because of its dynamic similarity to the Pacific El Niño. It manifests itself as interannual variations of the boreal summertime SSTs in the cold tongue region (the white box in Figure 1.1 is the ATL3 region over which SSTs are usually averaged to produce an Atlantic Niño index). The zonal TAV mode is driven by the Bjerknes feedback, i.e. a feedback between the zonal SST gradient and the strength of the atmospheric Walker circulation (e.g. Lübbecke et al., 2018). The meridional mode of tropical Atlantic variability is connected to the thermodynamic wind-evaporation feedback, and manifests itself as a meridional temperature gradient between Northern and Southern Hemisphere associated with wind anomalies blowing from the cold to the warm hemisphere, evolving in boreal spring (e.g. Joyce et al., 2004; Behera et al., 2013). Both the zonal and the meridional TAV mode influence rainfall over parts Africa and South America, and are thus of large importance for the local population (Behera et al., 2013).

1.1.2 Deep circulation and mean state

At intermediate depths, the circulation of the tropical oceans is dominated by two systems of zonal currents. Directly on the equator, the Equatorial Deep Jets (EDJ) are located, which are the main focus of this thesis and are therefore described in more detail in Section 1.2. The EDJ take the form of vertically stacked, alternating currents with downward phase propagation on interannual time scales, and can be seen schematically on the equator in Figure 1.2.
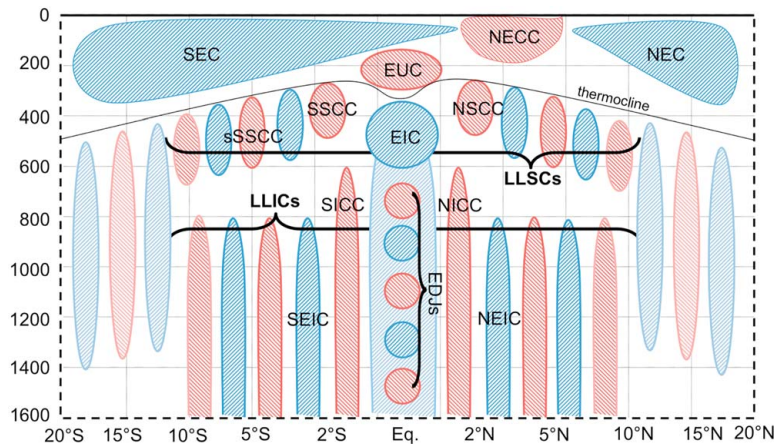
Figure 1.2: Schematic of the zonal current systems of the tropical oceans, including the subther-mocline currents. Red shading indicates eastward currents, blue shading westward currents. The abbreviations used in the figure stand for: South Equatorial Current (SEC), North Equatorial Countercurrent (NECC), North Equatorial Current (NEC), Equatorial Undercurrent (EUC), South Subsurface Countercurrent (SSCC) with secondary South Subsurface Countercurrent (sSSCC), North Subsurface Countercurrent (NSCC), Equatorial Intermediate Current (EIC), Low-Latitude Subsurface Countercurrents (LLSCs), Low-Latitude Intermediate Currents (LLICs), South Intermediate Countercurrent (SICC), North Intermediate Countercurrent (NICC), South Equatorial Intermediate Current (SEIC), North Equatorial Intermediate Current (NEIC), Equatorial Deep Jets (EDJs). *From Ménesguen et al. (2019).*

The other intermediate depth tropical zonal current system is called Low-Latitude Intermediate Currents (LLICs) in Figure 1.2. They appear as latitudinally alternating zonal current bands with

very large vertical scales, and are quasi-steady in time. The name of this current system is not very consistent across the literature; in this thesis, the name Equatorial Intermediate Current System (EICS) will be used to refer to these currents, as for example in Ascani et al. (2015). Since also the maintenance mechanism of the EICS is a research topic of this thesis, more details on the EICS are given in Section 1.3.

At intermediate depths between 300 m and 700 m, an Oxygen Minimum Zone (OMZ) is located in the eastern tropical Atlantic (Stramma et al., 2009; Hahn et al., 2014). Such open ocean OMZs are located in the eastern parts of all three tropical basins as the result of low ventilation (Luyten et al., 1983) combined with high biological oxygen consumption (Karstensen et al., 2008). In the Atlantic Ocean, a tongue of higher oxygen concentration extends along the equator into the eastern OMZ (Karstensen et al., 2008; Brandt et al., 2012), due to the presence of strong thermocline and subthermocline eastward currents including the eastward jets of the EDJ and EICS (Brandt et al., 2012, 2015).

1.1.3 Intraseasonal variability

While the zonal velocity variability in the tropical Atlantic Ocean is dominated by seasonal and interannual time scales, the meridional velocity is dominated by variability on intraseasonal time scales which is generated by instabilities in the upper ocean currents or the western boundary currents and propagates into the deep ocean as Yanai/mixed Rossby-gravity waves (e.g. Tuchen et al., 2018). It has been suspected for some time that the intraseasonal variability plays an important role for the generation and maintenance of the mean and slowly varying tropical circulation at intermediate depths, i.e. the EDJ and the EICS (d'Orgeville et al., 2007; Hua et al., 2008; Ascani et al., 2010, 2015; Greatbatch et al., 2018), a topic that is further explored in Chapters 2 and 5 of this thesis.
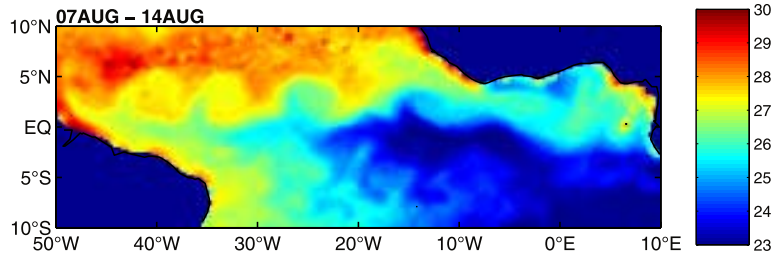
Figure 1.3: Tropical Atlantic sea surface temperature (SST) in °C from satellite measurements in early August 2002. A tropical instability wave (TIW) is visible at the northern edge of the cold tongue. *From Grodsky et al. (2005).*

Especially in boreal summer, the shear between the strong zonal currents in the upper tropical Atlantic Ocean leads to the growth of Tropical Instability Waves (TIWs). They can be clearly seen in satellite images of SST, where they appear as trains of large eddies along the SST fronts along the northern and southern edges of the cold tongue (see Figure 1.3). In the Northern Hemisphere, the TIWs are generated through both baroclinic instability and barotropic instability, the former due to the vertical shear of the nSEC and the latter due to the horizontal shear between EUC, nSEC and NECC, whereas in the Southern Hemisphere the generation of TIWs happens only through baroclinic instability due to the vertical shear of the cSEC (von Schuckmann et al., 2008). Atlantic TIWs have periods between 20 and 40 days (von Schuckmann et al., 2008), and horizontal

scales of 600–1200 km (Weisberg and Weingartner, 1988; Tuchen et al., 2018). While some TIWs stay confined to the surface of the tropical Atlantic Ocean, it also regularly happens that the TIW energy propagates downwards to depths below the EUC as intraseasonal Yanai wave beams (Brandt et al., 2006; von Schuckmann et al., 2008; Ascani et al., 2010; Tuchen et al., 2018). Such an event can be seen in the moored meridional velocity observations from 0°N, 23°W shown in Figure 1.4. For the location of the mooring, Tuchen et al. (2018) showed that the intraseasonal variability associated with these Yanai wave beams appears as an important peak in the spectrum down to depths of 2000 m. Below this depth, the intraseasonal variability peak suddenly shifts to other frequencies, suggesting different generation mechanisms such as Kelvin wave interaction with the Mid-Atlantic Ridge below this depth (Tuchen et al., 2018).
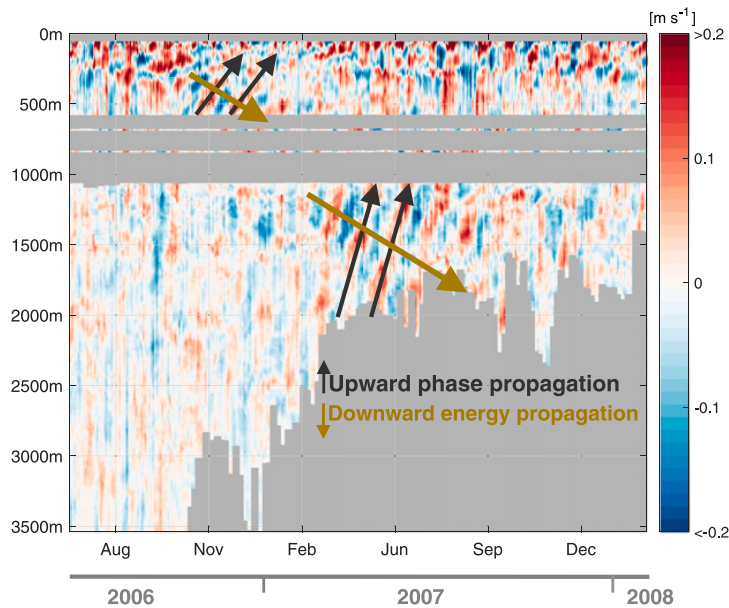
Figure 1.4: Meridional velocity measured by moored current metres on the equator at 23°W. Red colours indicate northward velocities, blue colours southward velocities. A Yanai wave beam with upward phase propagation and downward energy propagation is visible and marked with arrows. *From Tuchen et al. (2018).*

1.2 Equatorial deep jets

The main focus of this thesis are the Atlantic Equatorial Deep Jets (EDJ). In the following sections, they are therefore described in more detail, and theories on their dynamics and generation mechanisms are explained.

1.2.1 Historical overview and description

Luyten and Swallow (1976) first identified vertically stacked equatorial zonal currents in the Indian Ocean. A few years later, EDJ were measured also in the Pacific Ocean (Eriksen, 1981). In the Atlantic Ocean, the existence of EDJ was indirectly inferred already by Eriksen (1982) assuming that the jets were in geostrophic balance, but only later confirmed observationally by Ponte et al. (1990). They measured a vertical profile of the zonal velocity on the equator and at approximately

30°W, and from this estimated the Atlantic EDJ to extend down to a depth of 2500 m and have amplitudes of 10–20 cm s^{-1}. In the following years, their scales became better known thanks to more measurements. Gouriou et al. (1999) could show from several shipboard velocity profiles that the Atlantic EDJ have a vertical scale of 400–600 m and a meridional scale of about 1°. Gouriou et al. (2001) analysed velocity sections measured across the equator at three different longitudes (the central one is shown in Figure 1.5, where the vertically stacked EDJ can be clearly seen on the equator). With these they could show that the Atlantic EDJ are zonally coherent over at least 25°, which was confirmed by Johnson and Zhang (2003) who analysed the signature of the approximately geostrophic EDJ in CTD data and estimated their zonal wavelength to be 70°. Johnson and Zhang (2003) also examined the meridional structure of the Atlantic EDJ, which they found to be consistent with a first meridional mode Rossby wave. However, they noted that the meridional width of the EDJ is enhanced by a factor of 1.5 compared to theoretically expected. A similar widening had been found for the Pacific EDJ before, and Muench et al. (1994) suggested it might originate from averaging over EDJ that meander on short time scales due to meridional advection by mixed Rossby-gravity waves. Greatbatch et al. (2012), however, showed that the EDJ widening could also be attributed to much stronger mixing of momentum than tracers in the equatorial ocean.
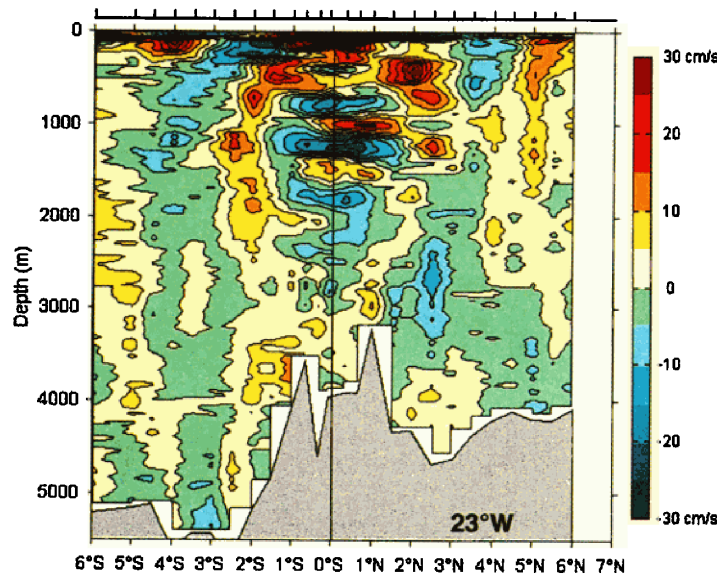
Figure 1.5: Shipboard section of zonal velocity along 23°W, measured in 1999. Positive values indicate eastward currents, negative values westward currents. The contour interval is 5 cm s^{-1}, and station positions are shown in black along the line above the figure. *From Gouriou et al. (2001).*

The temporal variability of the EDJ was difficult to access, although it became clear from the comparison of shipboard velocity profiles from different years that the EDJ change with time (e.g. Gouriou et al., 1999). Johnson and Zhang (2003) could show from CTD data that the Atlantic EDJ propagate downwards with a time scale of approximately 5 years. With the help of moored velocity measurements at 0°N, 23°W, Bunge et al. (2008) and Brandt et al. (2011b) could confirm the downward phase propagation of the Atlantic EDJ, and reestimate their period to be approximately 4.5 years. The equatorial mooring at 23°W has since been maintained and used in further studies to improve insight into the Atlantic EDJ scales and dynamics. In Figure 1.6, the zonal velocity measurements from the mooring up to 2019 can be seen. The EDJ are clearly visible

as vertically alternating current bands that propagate downwards with time. Recently, Youngs and Johnson (2015) updated the analysis of available CTD data by Johnson and Zhang (2003). They found for the Atlantic EDJ a vertical wavelength of 467.5 (with a 95% confidence interval between 373 and 635) stretched dbar, a meridional scale of 1.08°, a zonal wavelength of 68° (between 56° and 89°) and a period of 4.8 (between 4.6 and 5.0) years.
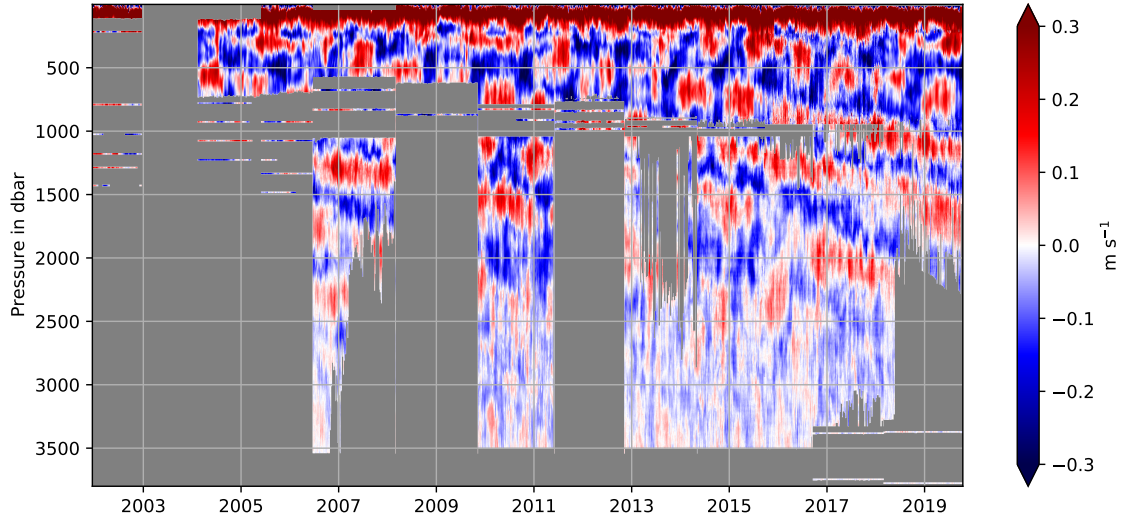
Figure 1.6: Hovmöller diagram of zonal velocity measured by moored current metres on the equator at 23°W. Positive values indicate eastward velocity, negative values westward velocity. *Updated from e.g. Brandt et al. (2011b); Greatbatch et al. (2018).*

1.2.2 EDJ dynamics

The EDJ show many characteristics of low frequency resonant equatorial basin modes for a high baroclinic vertical mode (e.g. d'Orgeville et al., 2007; Ascani et al., 2015; Matthießen et al., 2017). Resonant equatorial basin modes consist of the sum of an eastward propagating equatorial Kelvin wave and its reflection as westward propagating long odd-meridional-mode Rossby waves (Cane and Moore, 1981). The gravest of the basin modes is characterised by a zonal velocity amplitude maximum in the centre of the basin, and a period T_n of

$$T_n = \frac{4L}{c_n} \tag{1.1}$$

where L is the width of the equatorial ocean basin and c_n is the gravity wave speed of the nth baroclinic mode; i.e. the period of the gravest basin mode corresponds to the time it takes the Kelvin wave to cross the basin, L/c_n, plus the crossing time for the first meridional mode Rossby wave, $3L/c_n$ (Cane and Moore, 1981). The resonance frequency of the gravest equatorial basin mode for the Atlantic Ocean can be seen in Figure 1.7, indicated by the solid grey line, for the first 20 baroclinic modes. Also shown in the figure is the amplitude spectrum of the equatorial zonal velocity at 23°W, separately for each baroclinic mode and computed using mooring data. Four distinct peaks are visible: the time mean flow (zero frequency) for baroclinic modes 1 to 8, which is not associated with basin mode resonance; an annual peak around baroclinic mode 4; a semiannual peak at baroclinic mode 2, which both lie on the basin mode resonance curve (see also Brandt et al., 2016); and an interannual peak around baroclinic modes 16 and 17. The latter are

7

the Atlantic EDJ, and they also clearly lie on the resonance curve of the gravest equatorial basin mode.

Figure 1.7: Amplitude spectrum of the zonal velocity at 0°N, 23°W as shown in Figure 1.6, calculated after the decomposition of the zonal velocity into vertical normal modes. The dashed line marks the frequency of the Atlantic equatorial deep jets (EDJ), the solid line indicates the resonance frequency of the gravest equatorial basin mode. *From Greatbatch et al. (2018).*

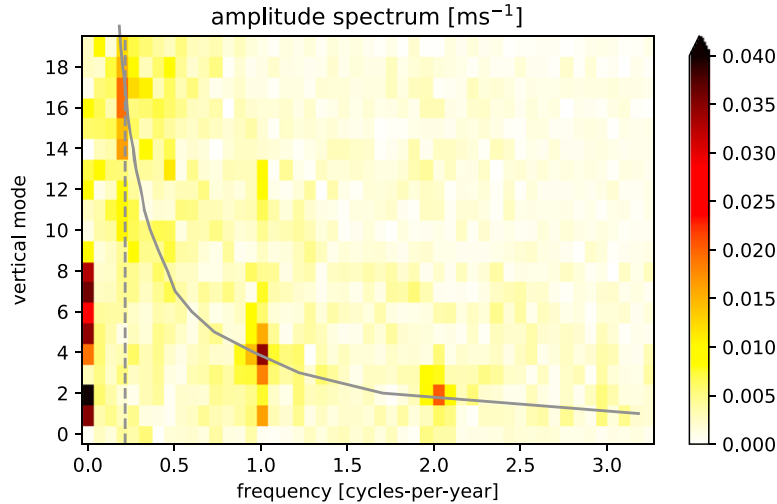Concerning the question of how the EDJ are excited and supplied with energy, there have been different theories over the years, adding to a slowly emerging understanding of the complicated cascade of processes involved in the formation of the EDJ. So far, no complete theory of the EDJ generation mechanisms exists (Ménesguen et al., 2019). Although Pedlosky (2002) claimed to have developed a complete theory of the EDJ, Pedlosky's theory was conclusively refuted by Ascani et al. (2004).

An important role in the EDJ generation and maintenance seems to be played by intraseasonal variability that is excited by instabilities at the ocean surface or at the western boundary and propagates into the deep ocean as intraseasonal mixed Rossby-gravity or Yanai waves, as described in Section 1.1.3. It has been suggested by quite a few studies that the EDJ emerge from the rectification of deep intraseasonal variability (d'Orgeville et al., 2007; Hua et al., 2008; Ménesguen et al., 2009). Hua et al. (2008), for example, showed analytically and in model experiments how a mixed Rossby-gravity wave can become unstable and generate vertically stacked, alternating zonal currents like the EDJ. All these studies, however, relied on unrealistic forcing of deep intraseasonal variability unconnected to what is really observed in the ocean. Ascani et al. (2015) presented model experiments that could simulate EDJ that, more realistically, originated from deep intraseasonal variability generated by instabilities of the upper ocean currents in the model. In a budget analysis of the zonal energy equation, Ascani et al. (2015) found that energy transfer to the EDJ happens through the meridional advection term, and identified the waves responsible for this energy transfer as intraseasonal Yanai waves with large vertical scales originally generated as TIWs at the surface, together with intraseasonal Yanai waves with small vertical scales generated intrinsically at depth through wave interaction.

A plausible physical explanation for the energy flux from intraseasonal Yanai waves into the EDJ through the meridional advection term was suggested by Greatbatch et al. (2018): the deformation

of intraseasonal waves by the EDJ. The mechanism is illustrated in Figure 1.8. If a slowly varying zonal current $\overline{u}$ with small meridional scale encounters an intraseasonal wave with larger meridional scale (e.g. a Yanai wave as described in Section 1.1.3 associated with low baroclinic modes or the barotropic mode), it will distort the wave in such a way that the net convergence of the meridional flux of intraseasonal zonal momentum, or

$$-\frac{\partial(\overline{u'v'})}{\partial y} \tag{1.2}$$

becomes non-zero. Here, u and v are zonal and meridional velocity, respectively, y denotes the distance from the equator measured positive northward, and Reynolds averaging has been done with a separation of time scales between intraseasonal (smaller than 70 days, denoted by a prime) and larger than intraseasonal (larger than 70 days, denoted by an overbar). Greatbatch et al. (2018) compare this proposed mechanism to the deformation of eddies by the atmospheric jet stream that also leads to momentum flux into, and thus reinforcement of, the jet stream. Indeed, they could show for the equatorial Atlantic in the depth range of the EDJ that the net equatorward flux of intraseasonal zonal momentum is positively correlated with the slowly varying zonal velocity, both in their idealised model simulations and in observations from moored current metres at 23°W.
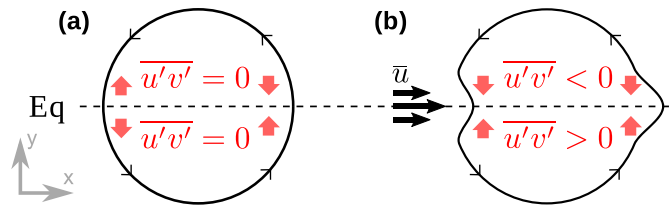
Figure 1.8: Schematic illustrating the EDJ maintenance mechanism proposed by Greatbatch et al. (2018). An initially circular (Panel a) intraseasonal Yanai or short Rossby wave of large meridional scale is distorted (Panel b) by a zonal jet of smaller meridional scale. The zonal jet is shown as thick black arrows. When the wave is undistorted (a), there is no net flux of intraseasonal zonal momentum towards the equator, but when it is distorted by the jet (b), the net flux of intraseasonal zonal momentum towards the equator becomes non-zero and reinforces the jet. *From Greatbatch et al. (2018).*

One important difference between the theories by Hua et al. (2008) compared to Ascani et al. (2015) and Greatbatch et al. (2018) is that Hua et al. (2008) examined the initial formation of the EDJ by destabilization of Yanai waves, while Ascani et al. (2015) and Greatbatch et al. (2018) investigated the EDJs' energy supply in a statistically steady state. It therefore seems likely that deep intraseasonal Yanai waves both rectify into the EDJ variability by becoming unstable, and maintain the EDJ in steady state through weak interaction, i.e. deformation of the waves leading to systematic momentum flux into the EDJ.

1.2.3 Importance of the EDJ

The Atlantic EDJ have been shown to contribute to the ventilation of the oxygen-poor regions in the eastern tropical Atlantic. Because of the zonal asymmetry in oxygen concentration at and below the thermocline (see Section 1.1.2), there is an enhanced oxygen concentration in the eastward jets compared to the westward jets of the EDJ (Brandt et al., 2008). This leads to interannual

variability in oxygen concentration, as well as a net eastward flux of oxygen along the equator through the EDJ (Brandt et al., 2012). The EDJ thus contribute to the supply of oxygen to the oxygen-poor regions of the intermediate depth eastern equatorial Atlantic.
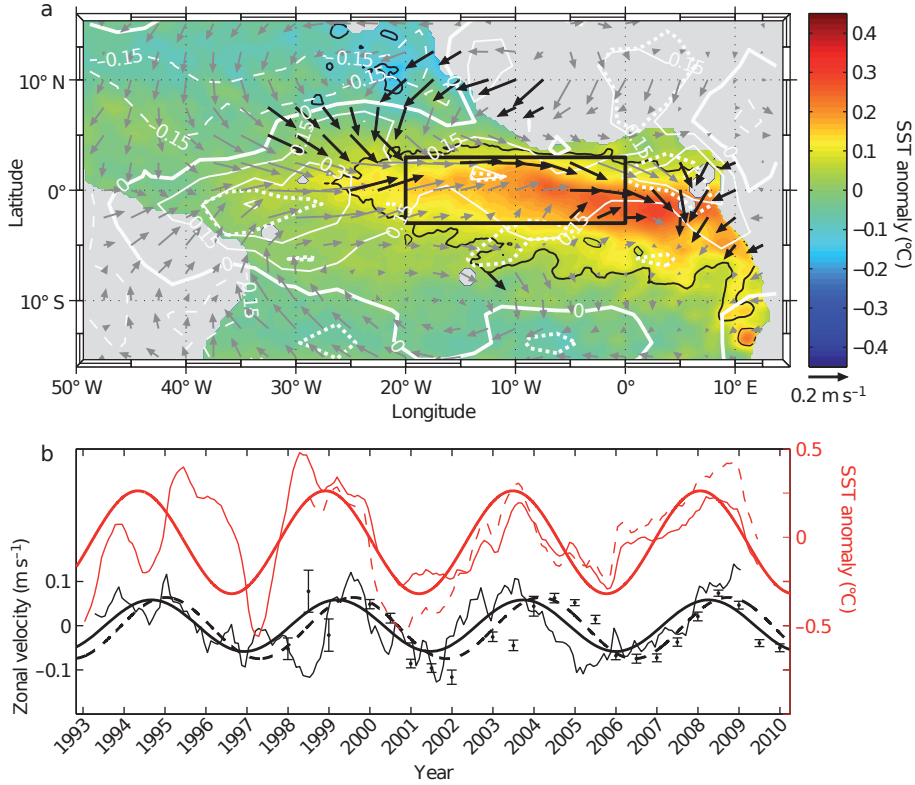
Figure 1.9: Interannual variability in the tropical Atlantic associated with the 1670-day (approximately 4.5-year) cycle of the equatorial deep jets (EDJ). Upper panel: Anomalies of sea surface temperature (SST, colour shading), surface wind (arrows) and rainfall (white contours, in $\mathrm{mm\,d^{-1}}$) as determined through regression on the 1670-day harmonic fit to the SST anomalies averaged within the black box (ATL3). Significant correlations are marked with black lines for SST, black arrows for wind and white dotted lines for rainfall. Lower panel: ATL3 SST anomaly (thin red lines, from two different products), with 1670-day harmonic fit (red thick line). Also shown is the surface zonal velocity anomaly on the equator between 35°W and 15°W (thin black line), with a 1670-day harmonic fit (thick black solid line), as well as the zonal velocity at 1000 m depth between 1°S and 1°N and 35°W and 15°W (black dots with standard errors), with a 1670-day harmonic fit (thick black dashed line). *From Brandt et al. (2011b).*

Additionally, the Atlantic EDJ have been suggested to influence both the surface ocean and the atmosphere above. Brandt et al. (2011b) found that the equatorial zonal surface currents vary with the 4.5-year cycle of the EDJ, and also with a similar amplitude (see Figure 1.9, lower panel), suggesting that the EDJ extend all the way up to the ocean surface. Since their energy propagation is directed upwards (Matthießen et al., 2015), this is plausible, although it is still an open question how the EDJ pass through the strong flow of the EUC without being dissipated. Through this influence on the surface zonal velocity, the EDJ also affect the SST around the equator, especially in the eastern part of the basin where the cold tongue is located. This can be seen in Figure 1.9a in the colour shading, as well as in Figure 1.9b. Furthermore, the 4.5-year cycle of the EDJ can also be found in surface winds and rainfall, consistent with their dependence on SST; see Figure 1.9a,

arrows and white contours. This makes the EDJ potentially valuable for improving interannual to decadal prediction, for example of rainfall at the western coast of Africa.

1.2.4 EDJ in ocean models

The EDJ are generally not faithfully, or not at all, simulated by ocean general circulation models (OGCMs). One known problem is the lack of horizontal, and especially vertical, resolution in these models, but this is not the only issue (e.g. Ascani et al., 2015; Matthießen, 2017, see also Chapter 4). Although the Atlantic EDJ have been simulated in a realistic high-resolution general circulation model by Eden and Dengler (2008), in that model the EDJ have an unrealistically small amplitude, lack vertical propagation, and do not show characteristics of a resonant equatorial basin mode but instead only consist of eastward propagating Kelvin waves without reflection into long Rossby waves. The lack of EDJ (and also a realistic EICS, see Section 1.3) in OGCMs poses a serious challenge for the modelling of the nutrient and oxygen distributions of the tropical oceans. As shown by Dietze and Loeptien (2013) and Getzlaff and Dietze (2013), the inaccurately simulated zonal current systems at intermediate depth in coupled global biogeochemical ocean models cause large errors in the oxygen and nutrient fields in the models.

However, the EDJ have been simulated in a number of idealised model simulations, both in rectangular or zonal channel primitive equation models (d'Orgeville et al., 2007; Hua et al., 2008; Ménesguen et al., 2009; Ascani et al., 2015; Matthießen et al., 2015, 2017; Greatbatch et al., 2018), and in multi-mode shallow water models (Greatbatch et al., 2012; Claus et al., 2014, 2016). In this thesis, the effort to learn about EDJ dynamics from idealised models is continued, and a possible way to develop an EDJ parameterisation for more realistic, global ocean models is suggested that could help improve the simulation of the mid-depth tropical oceans and interannual tropical Atlantic climate variability.

1.3 Equatorial intermediate current system

The Equatorial Intermediate Current System (EICS) has first been found and studied from shipboard velocity sections, but can also be well seen in mean velocity fields at intermediate depth from Argo float displacement data, as shown in Figure 1.10. There, the mean zonal velocity at 1000 m depth in the world ocean is shown, as computed from available Argo float data. In the tropical Pacific and Atlantic Oceans, narrow zonal currents can be seen that alternate with latitude and extend at least to 15°N/S from the equator. Vertically, they are coherent from about 500 m depth to 2000 m depth, and apart from small modulation by seasonal and annual Rossby waves, they seem to be quasi-steady in time at least over the few decades where observations are available (Ménesguen et al., 2019).

It is not entirely clear so far whether the entire EICS is really one current system, maybe even including the EDJ, with uniform dynamical origins (Ménesguen et al., 2019). So far, however, it looks as if the central part of the EICS close to the equator is excited by intraseasonal short Rossby or mixed Rossby-gravity, i.e. Yanai, waves that become unstable and form layered zonal current systems with either small vertical wavelength (EDJ) or small meridional wavelength (EICS, e.g. Hua et al., 2008; Ascani et al., 2010, 2015; Ménesguen et al., 2019), whereas the currents of the EICS that are located further away from the equator are likely generated by nonlinear triad
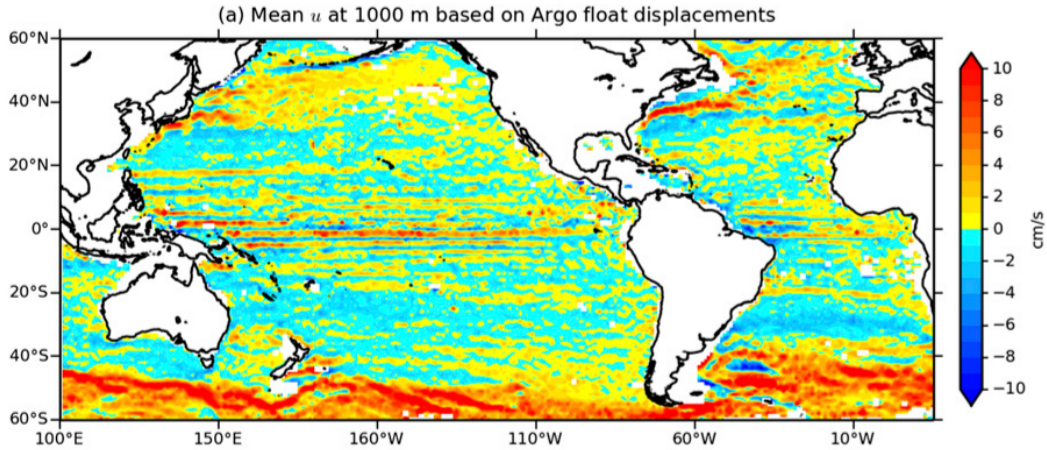
Figure 1.10: Mean zonal velocity at 1000 m depth from Argo float displacement data. *From Ascani et al. (2015).*

interaction of annual Rossby waves (e.g. Qiu et al., 2013; Ménesguen et al., 2019). The focus of this thesis is on the central part of the Atlantic EICS, especially the (mostly) westward flow on the equator and the flanking eastward South and North Intermediate Countercurrent (SICC and NICC) at 1.5 to 2°S/N (see Figure 1.2). Hua et al. (2008) and Ascani et al. (2010) showed that currents resembling this central part of the EICS can be generated by the destabilisation (and, in the case of Ascani et al., 2010, dissipation) of an idealised intraseasonal Yanai wave beam. On the other hand, Ascani et al. (2015) studied the generation of the central EICS in a model with more realistic deep intraseasonal variability and found that mostly short intraseasonal Rossby waves were responsible for the energy transfer to the EICS. Interestingly, Ascani et al. (2015) noticed in their kinetic energy budget analysis that also the EDJ transfer energy to the EICS.

Like the EDJ, the eastward jets of the EICS contribute to oxygen transport towards the OMZ in the eastern tropical Atlantic. Especially the SICC and NICC, the two eastward current bands flanking the equator at approximately 2°S and 2°N, are characterised by enhanced oxygen concentrations compared to the water around them in the eastern part of the basin (Brandt et al., 2008, 2015). Also like the EDJ, the EICS is often not well represented in ocean general circulation models, leading to deficiencies in the simulation of nutrient and oxygen distributions in the tropical oceans (Dietze and Loeptien, 2013; Getzlaff and Dietze, 2013).

1.4 Contribution of this thesis

This thesis contributes to improved understanding of the dynamics of the EDJ, the energy transfer from equatorial intraseasonal waves to the EDJ and EICS, as well as the energy transfer from the EDJ to the EICS. It also provides a new, comprehensive description of the EDJ in the Atlantic Ocean that might possibly be used for the development of an EDJ parameterisation to improve the simulation and prediction of tropical Atlantic climate.

The research questions that are answered are the following:

Is the momentum flux convergence that is associated with the deformation of intraseasonal waves by the EDJ enough to maintain them against dissipation?

Greatbatch et al. (2018) showed that there is a positive correlation between the Atlantic EDJ and the meridional convergence of the intraseasonal zonal momentum flux, suggesting that the momentum flux convergence arises because the EDJ distort intraseasonal waves. In Chapter 2, the question whether the thus generated momentum flux convergence is enough to maintain EDJ with a reasonable amplitude is answered with the help of an idealised model of the tropical Atlantic Ocean.

How do the EDJ modify the time mean circulation around the equator, i.e. the central part of the EICS?

Ascani et al. (2015) suggested that energy transfer takes place not only from intraseasonal variability to the EDJ, but also from the EDJ to the time mean zonal currents, i.e. the EICS. In Chapter 2, the time mean zonal flow that is generated by the EDJ is simulated in a model of the tropical Atlantic, and in Chapter 3, the energy transfer from the EDJ to the central EICS is investigated using Argo float measurements, corroborating the findings from the model.

What are the exact scales of the Atlantic EDJ?

Because of their vertical and temporal variability, as well as their location in the subthermocline ocean, measurements of the EDJ have been scarce and their scales not well quantified. In Chapter 3, a comprehensive new scale estimation of the Atlantic EDJ using the increasing amount of Argo float data is presented.

Is the enhanced meridional width of the EDJ due to averaging over meandering jets, or a widening through enhanced momentum dissipation?

Observations of the EDJ have shown that their time mean cross-equatorial width is larger by a factor of 1.5 than theoretically expected. Muench et al. (1994) suggested that this might be caused by time averaging over jets that meander due to meridional advection by intraseasonal waves, whereas Greatbatch et al. (2012) showed that the EDJ could also be widened by an enhanced lateral mixing of momentum combined with small diapycnal mixing of density in the tropical oceans. In Chapter 4, the contributions of the two suggested processes to the mean meridional width of the EDJ are investigated using different idealised models of the tropical Atlantic.

Does the meridional momentum flux convergence due to the deformation of intraseasonal waves also maintain the central part of the EICS?

The mechanism suggested by Greatbatch et al. (2018) to be responsible for maintaining the EDJ against dissipation theoretically works for all equatorial zonal currents that are slowly varying or steady in time. Therefore, idealised model configurations of the tropical Atlantic Ocean are also used here to investigate the role of the intraseasonal momentum flux convergence for the central part of the EICS. The results are presented in Chapter 5.

2 Equatorial deep jets and their influence on the mean equatorial circulation in an idealized ocean model forced by intraseasonal momentum flux convergence

The candidate's contributions to the publication (including the Supporting Information, provided on the pages following the main article) are as follows:

- She contributed to shaping the research questions that are answered in the paper.

- She ran all model experiments described in the paper.

- She performed all analyses.

- She produced all figures.

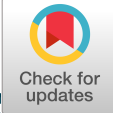- She authored the manuscript from the first draft to the final version.

Equatorial Deep Jets and Their Influence on the Mean Equatorial Circulation in an Idealized Ocean Model Forced by Intraseasonal Momentum Flux Convergence

Swantje Bastin[1] [ID], **Martin Claus[1,2]** [ID], **Peter Brandt[1,2]** [ID], and **Richard J. Greatbatch[1,2]** [ID]

[1]GEOMAR Helmholtz Centre for Ocean Research, Kiel, Germany, [2]Faculty of Mathematics and Natural Sciences, Kiel University, Kiel, Germany

Abstract Equatorial deep jets (EDJ) are vertically stacked, downward propagating zonal currents that alternate in direction with depth. In the tropical Atlantic, they have been shown to influence both surface conditions and tracer variability. Despite their importance, the EDJ are absent in most ocean models. Here we show that EDJ can be generated in an idealized ocean model when the model is driven only by the convergence of the meridional flux of intraseasonal zonal momentum diagnosed from a companion model run driven by steady wind forcing, corroborating the recent theory that intraseasonal momentum flux convergence maintains the EDJ. Additionally, the EDJ in our model nonlinearly generate mean zonal currents at intermediate depths that show similarities in structure to the observed circulation in the deep equatorial Atlantic, indicating their importance for simulating the tropical ocean mean state.

Plain Language Summary In the tropical Atlantic Ocean between 500 and 2,000 m depth, a system of ocean currents called *equatorial deep jets* (EDJ) can be found. This current system consists of multiple currents or *jets* stacked on top of each other and flowing along the equator, alternately (in the vertical) to the east and to the west. The entire system of currents moves slowly downward, such that at a fixed depth, the flow direction reverses periodically. The EDJ are suggested to influence the weather at the ocean surface, as well as the transport of substances in the deep ocean, for example, oxygen that is essential for much of oceanic life. Despite this, their driving mechanisms are not yet fully understood, and they are not yet present in most ocean model simulations. We show here an idealized ocean model experiment that strongly supports the recently developed theory that the EDJ draw most of their flow energy from the interaction with oceanic equatorial waves with a period of about a month. We also show that, when the EDJ are included in our simulation, a set of mean ocean currents develops that shows similarities to what has been measured in the deep tropical Atlantic Ocean.

1. Introduction

The tropical oceans are characterized by strong zonal current systems. One example are the equatorial deep jets (EDJ) that were first discovered in the Indian Ocean in the 1970s by Luyten and Swallow (1976). Later, it was found that there are EDJ in all three ocean basins (Firing, 1987; Gouriou et al., 1999; Hayes & Milburn, 1980; Johnson et al., 2002; Johnson & Zhang, 2003; Leetmaa & Spain, 1981). The EDJ take the form of vertically stacked zonal currents along the equator that alternate in direction with depth. Whereas their vertical wavelength is on the order of a few hundred meters, their zonal structure is coherent over scales comparable to the width of the ocean basins (Gouriou et al., 1999; Johnson & Zhang, 2003; Youngs & Johnson, 2015). Their meridional structure is that of equatorially trapped waves with exponential amplitude decay away from the equator, although there has been some debate about the length scale of this decay, which is larger than expected based on inviscid theory (Greatbatch et al., 2012; Johnson & Zhang, 2003). Their vertical scale is thought to be set by the instability, or resonant triad interaction, of intraseasonal waves (Hua et al., 2008) that are, in turn, excited through instabilities in the western boundary currents (d'Orgeville et al., 2007) or in the upper ocean currents (Ascani et al., 2015). Much of the variability at the equator, especially in the Atlantic, is resonant at frequencies corresponding to basin modes (Brandt et al., 2016; Cane & Moore, 1981), which is also true for the EDJ (e.g., Ascani et al., 2015; d'Orgeville et al., 2007;

Matthießen et al., 2015; Matthießen et al., 2017). The period of the gravest of these resonant basin modes, T_n, is set by the time it takes for a Kelvin wave to propagate across the basin, be reflected as the gravest long Rossby wave and propagate back to the western boundary, that is,

$$T_n = \frac{4L}{c_n},\qquad(1)$$

where L is the width of the basin, n is the vertical normal mode in question, and c_n is the gravity wave phase speed for that vertical normal mode. Because of the dependence on the width of the basin, the EDJ in the Pacific vary on considerably longer time scales than those in the Indian or Atlantic Oceans (Youngs & Johnson, 2015). We will focus on the Atlantic EDJ in this article, where, in observations, the EDJ period is approximately 4.5 years (Bunge et al., 2008; Brandt et al., 2011) and their vertical structure is best described by the 15th baroclinic mode (Brandt et al., 2008).

Observations of the Atlantic EDJ show that their vertical phase propagation is directed downward. Assuming linear wave theory, this implies upward group velocity, that is, upward energy propagation, also shown in a nonlinear model simulation by Matthießen et al. (2015). Consistent with this, variability at the dominant EDJ period has been found in different surface parameters in the eastern equatorial Atlantic region, including the sea surface temperature, winds, rainfall, and geostrophic surface currents (Brandt et al., 2011). Additionally, the EDJ influence oxygen concentrations in the intermediate and deep ocean, both the variability and the mean state (Brandt et al., 2012, 2015). Finally, the EDJ seem to have an influence on the time mean equatorial circulation. Ascani et al. (2015) have shown that there is nonlinear energy transfer between variability at EDJ scales and the mean zonal currents, possibly enhancing the zonal exchange in the equatorial belt. The presence of zonal currents also strengthens the meridional gradients of potential vorticity (Claus et al., 2014), thereby reducing the meridional exchange of momentum, tracers, and particles (Kiko et al., 2017; Ménesguen et al., 2009).

Despite the EDJs' importance for ocean surface variables and deep ocean tracer distribution and variability, their driving mechanisms are not yet completely understood. Claus et al. (2016) showed that, apart from the excitation of the EDJ by barotropic instability of intraseasonal waves, as suggested by Hua et al. (2008), there must also be a mechanism maintaining the EDJ against dissipation directly in their depth range. They argue that given realistic dissipation values, in the absence of forcing, the EDJ energy cannot vertically propagate a much larger distance than the EDJs' vertical wavelength (Claus et al., 2016). A likely mechanism for the EDJ maintenance at depth has recently been proposed by Greatbatch et al. (2018). They showed that there is a positive correlation of the slowly varying zonal velocity associated with the EDJ and the convergence of the meridional flux of intraseasonal zonal momentum. The explanation they propose is that the EDJ deform intraseasonal waves such that the convergence of the intraseasonal momentum flux becomes nonzero and reinforces the deep jets, comparable to the deformation of eddies in the atmospheric jet stream and the accompanying momentum flux convergence.

In this study, we explore the effect of introducing the intraseasonal momentum flux convergence (IMFC) associated with the EDJ, which we diagnose from an idealized, wind-forced model of the tropical Atlantic, as the only momentum forcing into the same model without wind. We can show that it is possible to generate EDJ with realistic amplitude by prescribing the IMFC, corroborating the theory put forward by Greatbatch et al. (2018) that the IMFC likely is the key mechanism responsible for the EDJ maintenance at depth. Additionally we can show that, in our idealized model, the EDJ nonlinearly generate time mean zonal flow in the EDJ depth range, confirming the results of Ascani et al. (2015). The mean zonal circulation that is driven by the EDJ in our model exhibits similarities in structure to the observed mean flow at intermediate depth in the equatorial Atlantic. Section 2 provides a description of the model and our experiment setup. The results are presented in section 3 and summarized and discussed in section 4.

2. Model and Methods
2.1. Model Description and Setup
The results shown in this study have been obtained with an idealized ocean model of the tropical Atlantic basin. We use the Nucleus for European Modelling of the Ocean (NEMO) Version 3.6 (Madec et al., 2017). Our basic setup is inspired by the model setups described in Ascani et al. (2015) and Matthießen et al. (2015).

Our rectangular model basin with closed boundaries extends from 20°S to 20°N and over a width of 55°, mimicking the width of the Atlantic Ocean at the equator. The basin is 5,000 m deep with a flat bottom.
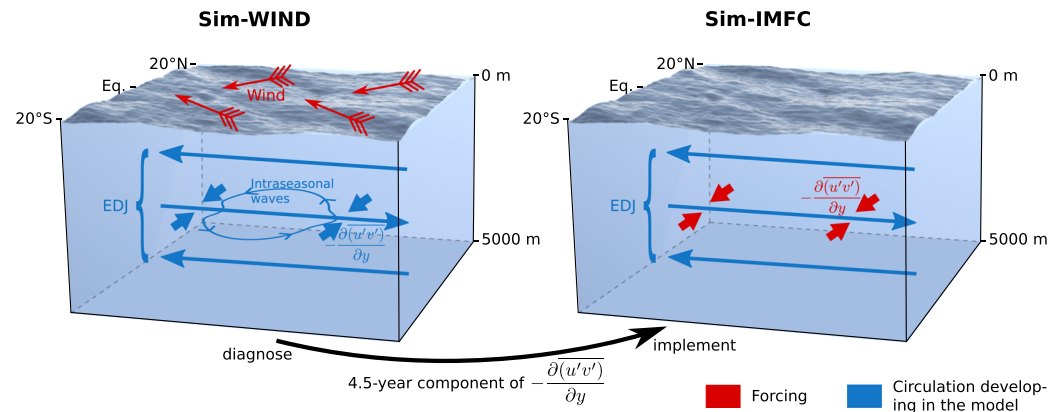
Figure 1. Schematic depiction of the model experiment design.

The horizontal resolution is 0.25° × 0.25°, whereas the vertical resolution is, with 200 levels, considerably finer at depth than that usually employed in ocean models to enable the simulation of EDJ. The vertical mixing scheme is Richardson number dependent, following Pacanowski and Philander (1981). We initialize the model with vertical temperature and salinity profiles from the World Ocean Atlas 2018 (Locarnini et al., 2019; Zweng et al., 2019). For more details see the supporting information.

2.2. Experiment Design

We run this idealized model configuration twice (summarized in Figure 1). For the first run, named Sim-WIND in the following, we force the model at the surface with steady, zonally averaged wind stress calculated from NCEP/NCAR reanalysis data (Kalnay et al., 1996; Kistler et al., 2001). With the wind forcing, both intraseasonal waves and EDJ with the same period as found in observations (4.5 years) are present in the model, and the suggested mechanism for maintaining the EDJ through distortion of the intraseasonal waves from Greatbatch et al. (2018) can come into effect (see left panel of Figure 1). From Sim-WIND we diagnose at every grid point in the basin the intraseasonal momentum flux convergence (IMFC) that is associated with the EDJ (i.e., the 4.5-year Fourier component of $-\partial(\overline{u'v'})/\partial y$, where the overbar/prime denotes variability on time scales larger/smaller than 70 days). The second model run, named Sim-IMFC, is only forced with the diagnosed IMFC; that is, the term is added to the zonal momentum equation at every time step (see right panel of Figure 1). By adding the term to the equation rather than applying a relaxation scheme, we ensure that our forcing does not interfere with other model dynamics.

2.3. Argo Analysis

We use deep velocity data calculated from Argo float measurements by Lebedev et al. (2007), covering a time period of nearly 20 years (2000–2019), for an estimation of the mean zonal flow field at 1,000 m depth in the equatorial Atlantic. The Argo data have been spatially smoothed and corrected for sampling bias associated with the presence of EDJ before taking the time mean, using methods of Edelson and Krolik (1988), Lomb (1976), and Scargle (1982). For details see the supporting information.

3. Results

3.1. Generation of EDJ by Intraseasonal Momentum Flux Convergence

The characteristics of the EDJ that develop in our idealized model simulations can be seen in Figure 2. For a comparison of the modeled EDJ to observations, the reader is referred to the supporting information; here, it is sufficient to say that the main characteristics of the Atlantic EDJ are well represented in our model. The EDJ that emerge through our internal forcing with the intraseasonal momentum flux convergence are very similar to those in the wind-forced simulation, at least between approximately 400 and 1,800 m depth (below that, the diagnosed IMFC is weak, resulting in weak EDJ in Sim-IMFC). The most striking differences between the simulations are the missing near-surface circulation (e.g., the Equatorial Undercurrent) due to the lack of wind forcing, and the strong reduction of variability on frequencies other than the EDJ frequency in Sim-IMFC. Both differences are intended and due to our experiment design (recall, in particular, that Sim-IMFC is forced at a single period of 4.5 years). Figures 2c and 2d show the time series of zonal velocity projected onto the dominant vertical mode. The EDJ in both model simulations have similar amplitudes,
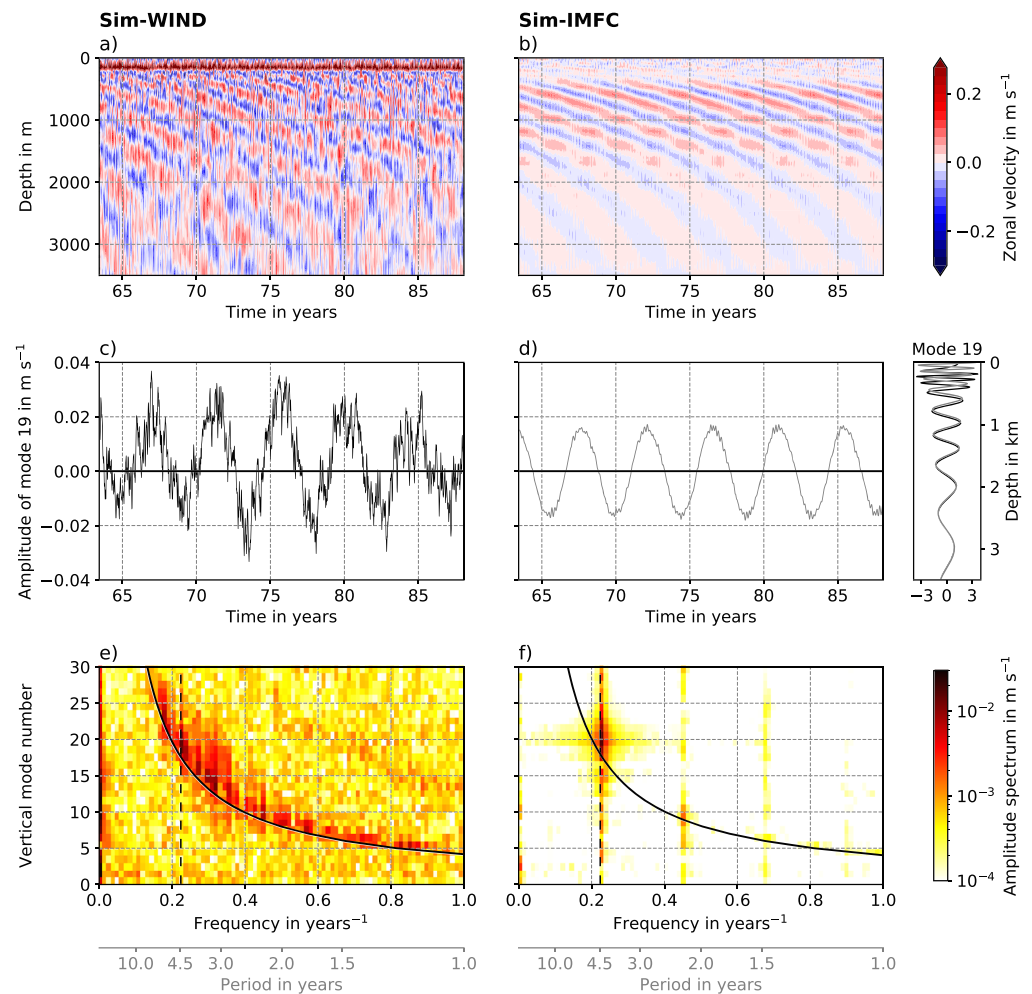
Figure 2. EDJ in the two model runs; Sim-WIND on the left (a, c, and e) and Sim-IMFC on the right (b, d, and f). Panels a and b show Hovmöller diagrams of zonal velocity on the equator in the center of the model basin. Panels c and d show time series of zonal velocity projected onto the 19th vertical normal mode (one of the dominant modes of the EDJ, cf. Panels e and f) at the center of the basin. The associated structure functions from both model runs are shown on the right. Panels e and f show amplitude spectra of zonal velocity at the center of the basin, calculated after the decomposition of the velocity into vertical normal modes. The gravest equatorial basin mode resonance curve is drawn in solid black. The dashed black line indicates the dominant EDJ frequency.

although the amplitude shows more fluctuation in Sim-WIND because of the superposition with variability on different time scales. In Figures 2e and 2f, amplitude spectra of the zonal velocity, projected onto vertical normal modes, at the center of the model basin are shown. The spectral energy is clearly centered around the gravest equatorial basin mode (cf. equation (1) and the solid black line in the figure), and the EDJ (cf. dashed black line) represent a prominent peak.

Although the temporal and vertical (and zonal, not shown) structures of the EDJ in both simulations are similar, the meridional structure is different—in Sim-IMFC, the EDJ are significantly narrower than in Sim-WIND. We attribute the difference in EDJ width to the missing influence of the wind and associated variability in Sim-IMFC and the related changes in effective momentum viscosity (cf. Greatbatch et al., 2012), because it is not connected to the structure of the forcing itself. However, this is a topic that requires further research.

It was already noted by Greatbatch et al. (2018) that the structure and magnitude of the intraseasonal momentum flux convergence agree well with the estimates of Claus et al. (2016) regarding the forcing necessary to maintain the EDJ at depth. This is also true for our simulations: The IMFC varying at the EDJ

20

frequency that we diagnosed from Sim-WIND has an amplitude of up to $4 \cdot 10^{-9}$ m s^{-2} at the equator, which is consistent with both Claus et al. (2016) and Greatbatch et al. (2018). The fact that this IMFC forcing alone can, in our model, drive and maintain EDJ that are realistic in amplitude and structure strongly supports the idea proposed by Greatbatch et al. (2018) based on theoretical considerations that the IMFC is the key process maintaining the EDJ at depth.

3.2. Influence on the Time Mean Zonal Flow

As can be seen from Figure 2f, variability on frequencies different from the forcing frequency is generated nonlinearly in Sim-IMFC. Particularly interesting is the generation of time mean zonal flow from the EDJ variability (at the zero frequency in the spectrum). Figures 3a–3c show the time mean zonal velocity at 1,000 m depth, from both model runs and Argo float data (Lebedev et al., 2007). Note that the color range is scaled by a factor of 5 for Sim-IMFC. In the model, the structure of the mean zonal flow is very similar at all depths where the EDJ are strong, that is, between approximately 400 and 1,800 m. The mean zonal flow at depth in Sim-WIND is dominated by westward flow on the equator and eastward flow approximately 2° north and south of the equator in the western half of the basin. This structure is also found from Argo data in the western basin. The strong westward flow on the equator and the flanking eastward jets at about 2°N/S are usually described as the central part of the equatorial intermediate current system both in the Atlantic and the Pacific Ocean (EICS, cf., e.g., Ascani et al., 2010; Cravatte et al., 2012, 2017; Ménesguen et al., 2019) and have been suggested to originate from dissipation associated with the breaking of downward propagating equatorial Yanai waves by Ascani et al. (2010).

The mean zonal flow that is generated nonlinearly by the EDJ in Sim-IMFC also displays this characteristic structure with one jet on the equator flanked by reversed jets to the north and south: here, however, including a midbasin change of sign that has also been noted by Ascani et al. (2015). In the western part of the basin between 45°W and about 30°W, the generated mean flow is westward on the equator and eastward to the north and south, whereas in the central and eastern parts of the basin between about 25°W and 5°W, there is eastward flow on the equator, flanked by weak westward current bands. The EDJ thus seem to strengthen the equatorial westward and flanking eastward flow that Ascani et al. (2010) attributed to downward propagating Yanai wave beams in the west of the basin but counteract it in the central and eastern basin.

Interestingly, a similar midbasin change of current direction can also be seen in the Argo data. The westward flow on the equator only extends into about one third of the basin and is superseded by eastward flow in some regions close to the center of the basin, resembling the structure of the mean zonal flow generated by the EDJ in Sim-IMFC. This suggests that the Atlantic EDJ play a role in establishing the mean zonal current direction on the equator, in the central basin possibly even reversing the otherwise predominantly westward flow that has so far been considered the central branch of the EICS.

The magnitude of the flow generated by the EDJ in our model only amounts to at most half of the total time mean zonal velocity measured by Argo around the equator in the center of the basin. This is therefore not enough to explain the Argo mean velocity field. However, it is difficult from our idealized model study to infer the exact magnitude of the mean flow that would be generated from the EDJ in the real ocean—for example, the amplitude of the EDJ in our model simulations is rather small (see Figure S5 in the supporting information). Because of the nonlinearity of the time mean zonal flow generation, the real Atlantic EDJ might, with a slightly larger amplitude, generate much stronger mean currents. We have tested the effect of different IMFC forcing amplitudes and thus different EDJ strengths in additional model runs, confirming a larger than linear increase of the mean flow amplitude with linearly increasing EDJ amplitude (shown in the supporting information). The structure of the generated mean flow, however, stays the same for different EDJ amplitudes.

Figures 3d/3e show the dominant terms of the nonlinear energy transfer from the EDJ to the time mean zonal circulation in Sim-IMFC, averaged over different areas around the equator. Consistent with the results of Ascani et al. (2015), the transfer of energy from EDJ to mean zonal flow mainly occurs through the term $-\partial(\overline{u'u'})/\partial x$, whereas some, but less, energy is transferred from the mean flow to the EDJ through $-\partial(\overline{u'v'})/\partial y$ (the overbar denoting the time mean, the prime deviations from the time mean including mainly the EDJ; not to be confused with the IMFC, where the separation of time scales was between intraseasonal and longer than intraseasonal). The energy transfer is largest close to the equator, but the sign is consistent over almost all averaging areas. The fact that $-\partial(\overline{u'u'})/\partial x$ is the responsible term for the energy transfer from

21
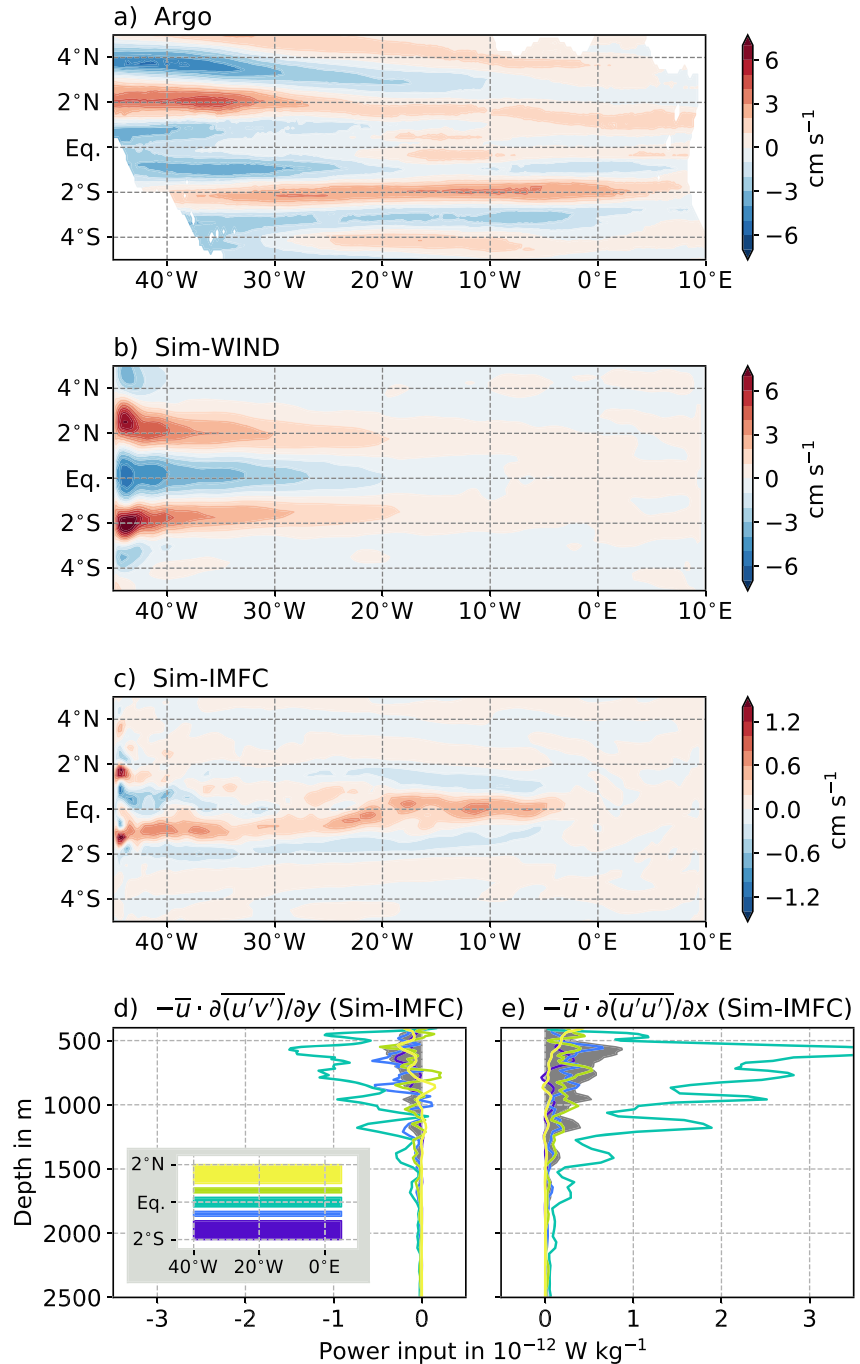
Figure 3. Time mean zonal velocity at 1,000 m depth from Argo (Lebedev et al., 2007, Panel a) and from the model runs (Panels b and c). Panels d and e show the time and space averaged nonlinear power input from EDJ into mean zonal flow from Sim-IMFC. The power input through $-\partial\overline{(u'w')}/\partial z$ (not shown) is negligible compared to the other two terms. The overline here denotes a time average, whereas the prime denotes all deviations from this time average (i.e., mainly the EDJ). The inset in Panel d shows the averaging areas corresponding to the color-coded curves in Panels d and e; the filled dark gray curve is the average over all five colored areas.

22

EDJ to mean flow agrees with the zonal structure of the generated mean flow, in particular its midbasin change of direction.

4. Summary and Discussion

In this study, we have shown that it is possible to drive realistic EDJ in an idealized ocean model by forcing only with the convergence of the meridional flux of intraseasonal zonal momentum that is associated with the EDJ in the momentum equation. We have also shown that, in our model, the EDJ nonlinearly generate time mean zonal flow that shows similarities in structure to the mean flow measured by Argo floats at 1,000 m depth along the equator.

The EDJ are stacked zonal jets with large vertical and small zonal wave numbers in the deep equatorial oceans that propagate downward with time, the entire system resembling a resonant equatorial basin mode associated with high vertical baroclinic modes. Apart from their excitation mechanisms that have been the topic of research for some time, one interesting feature of the EDJs' dynamics is the question of how they are maintained against dissipation after their initial generation. Claus et al. (2016) argued that there must be a local forcing process at work in the depth range of the EDJ in order for the EDJ to retain their amplitude over several vertical wavelengths. Greatbatch et al. (2018) suggested that this process could be the deformation of intraseasonal waves by the EDJ, which they argue leads to convergence of the meridional flux of intraseasonal zonal momentum (referred to as intraseasonal momentum flux convergence, IMFC, here), reinforcing the EDJ. As shown by Greatbatch et al. (2018), the magnitude of the IMFC associated with the EDJ agrees well with that of the necessary local forcing amplitude as derived by Claus et al. (2016), making this mechanism a plausible candidate for the EDJ maintenance at depth.

With this study, we were able to confirm the theory proposed by Greatbatch et al. (2018) by showing that the IMFC can actually drive sufficiently strong EDJ in an idealized ocean model. We diagnosed the IMFC varying at the EDJ frequency from a model configuration that is able to simulate EDJ; a rectangular tropical Atlantic basin model driven by steady wind forcing. Applying the diagnosed IMFC as momentum forcing to a companion model without any other forcing (i.e., without wind) yields EDJ that are very similar in their main characteristics to those arising in the wind-forced model, in particular, they reach a similar amplitude. Our results thus strongly corroborate the theory put forward by Greatbatch et al. (2018) that the IMFC is largely responsible for maintaining the EDJ.

One thing to bear in mind concerning our modeling approach is that the generation of the EDJ, in reality, does not happen through IMFC as in our simulation. In the real ocean, the momentum forcing through the IMFC only kicks in when the EDJ are already there and strong enough to distort intraseasonal equatorial waves. How the EDJ are generated in the first place is an ongoing topic of research, but it is generally thought that they originate from a number of different mechanisms that involve instabilities in the upper ocean currents and the deep western boundary currents, which excite deep equatorial intraseasonal variability that rectifies into the EDJ basin modes (e.g., Ascani et al., 2010, 2015; d'Orgeville et al., 2007; Hua et al., 2008; Ménesguen et al., 2019).

Interestingly, in the model configuration that we forced only with IMFC varying at the EDJ frequency, variability also on other time scales appears—in particular there is time mean flow that is generated nonlinearly from the EDJ variability. This has already been shown by Ascani et al. (2015) for specific EDJ basin modes, and indeed, we can show that in our simulation the energy is transferred from EDJ to mean zonal flow mainly through the zonal self-advection of the EDJ, corroborating their results.

The mean zonal flow at intermediate depths that is generated by the EDJ in our model is westward in the western third of the basin, but otherwise predominantly eastward on the equator, in the opposite direction to the mean westward equatorial flow that has been suggested to be driven by downward propagating, dissipating Yanai wave beams (Ascani et al., 2010) and usually thought to be the central part of the system of low-mode, latitudinally alternating zonal jets in the tropical oceans often called the equatorial intermediate current system (EICS, e.g., Ascani et al., 2010; Cravatte et al., 2017; Ménesguen et al., 2019). Indeed, Argo observations from 1,000 m depth in the Atlantic show that on the equator, the mean zonal velocity is clearly westward only in approximately the western third of the basin and becomes eastward in some places around the basin center. Our results thus suggest that the Atlantic EDJ play a role in establishing the mean zonal current direction on the equator. However, this effect might be important only in the equatorial Atlantic

Ocean. In the Pacific, the mean zonal flow at intermediate depth appears to be westward throughout most of the basin (e.g., Cravatte et al., 2017), indicating that here, the influence of the EDJ is not strong enough to reverse the current direction. This is consistent with the fact that the Atlantic EDJ are significantly stronger than those in the Pacific and Indian Oceans (e.g., Youngs & Johnson, 2015). It is also consistent with the much larger basin width, that is, zonal extent of the EDJ, in the Pacific, because the transfer of energy to the mean flow depends on the zonal gradient of EDJ strength, which is likely small over a larger part of the central Pacific compared to the central Atlantic. Eastward flow along the equator as part of the system of latitudinally alternating zonal jets has also been simulated by Qiu et al. (2013) as the result of nonlinear triad interactions of annual baroclinic Rossby waves. However, it should be noted that they used a $1\frac{1}{2}$-layer reduced-gravity model designed to simulate the off-equatorial zonal jets, not the equatorial circulation. Also, the observed westward equatorial flow in the Pacific suggests that the mechanism that is at work in their model is of minor importance directly on the equator.

It is known that many global biogeochemical ocean models struggle with oxygen and nutrient distributions in the deep tropical oceans. In general, the oxygen minimum zones in the deep eastern ocean basins are larger in models than in reality, likely because the correct ventilation by the equatorial current system is missing (Dietze & Loeptien, 2013; Getzlaff & Dietze, 2013). Associated with this, there is an excess of nutrients in these regions, usually termed "Nutrient Trapping" (Najjar et al., 1992). It has been shown before that the EDJ are responsible for ventilation of the eastern oxygen minimum zones (OMZ), albeit because of the asymmetry in oxygen production and consumption leading to a net eastward oxygen flux due to advection by the EDJ themselves (Brandt et al., 2012). Our results make clear that the Atlantic EDJ likely additionally contribute to OMZ ventilation by generating eastward time mean flow along the equator. The fact that the EDJ are not usually represented in global ocean models thus constitutes a serious shortcoming, and we suggest that including them in ocean models could not only lead to a better representation of the variability, but also of the mean state of the equatorial current system.

References

Ascani, F., Firing, E., Dutrieux, P., McCreary, J. P., & Ishida, A. (2010). Deep equatorial ocean circulation induced by a forced-dissipated Yanai beam. *Journal of Physical Oceanography*, 40, 1118–1142. https://doi.org/10.1175/2010JPO4356.1

Ascani, F., Firing, E., McCreary, J. P., Brandt, P., & Greatbatch, R. J. (2015). The deep equatorial ocean circulation in wind-forced numerical solutions. *Journal of Physical Oceanography*, 45, 1709–1734. https://doi.org/10.1175/JPO-D-14-0171.1

Bastin, S., Claus, M., Brandt, P., & Greatbatch, R. J. (2020). Supplementary dataset for Bastin et al. (2020), Geophysical Research Letters. (Version 0.1), [data set], Zenodo. https://doi.org/10.5281/zenodo.3689335

Brandt, P., Bange, H. W., Banyte, D., Dengler, M., Didwischus, S.-H., Fischer, T., et al. (2015). On the role of circulation and mixing in the ventilation of oxygen minimum zones with a focus on the eastern tropical North Atlantic. *Biogeosciences*, 12, 489–512. https://doi.org/10.5194/bg-12-489-2015

Brandt, P., Claus, M., Greatbatch, R. J., Kopte, R., Toole, J. M., Johns, W. E., & Böning, C. W. (2016). Annual and semiannual cycle of equatorial Atlantic circulation associated with basin-mode resonance. *Journal of Physical Oceanography*, 46, 3011–3029. https://doi.org/10.1175/JPO-D-15-0248.1

Brandt, P., Funk, A., Hormann, V., Dengler, M., Greatbatch, R. J., & Toole, J. M. (2011). Interannual atmospheric variability forced by the deep equatorial Atlantic Ocean. *Nature*, 473, 497–500. https://doi.org/10.1038/nature10013

Brandt, P., Greatbatch, R. J., Claus, M., Didwischus, S.-H., Hormann, V., Funk, A., et al. (2012). Ventilation of the equatorial Atlantic by the equatorial deep jets. *Journal of Geophysical Research*, 117, C12015. https://doi.org/10.1029/2012JC008118

Brandt, P., Hormann, V., Bourlès, B., Fischer, J., Schott, F. A., Stramma, L., & Dengler, M. (2008). Oxygen tongues and zonal currents in the equatorial Atlantic. *Journal of Geophysical Research*, 113, C04012. https://doi.org/10.1029/2007JC004435

Bunge, L., Provost, C., Hua, B. L., & Kartavtseff, A. (2008). Variability at intermediate depths at the equator in the Atlantic Ocean in 2000–06: Annual cycle, equatorial deep jets, and intraseasonal meridional velocity fluctuations. *Journal of Physical Oceanography*, 38, 1794–1806. https://doi.org/10.1175/2008JPO3781.1

Cane, M. A., & Moore, D. W. (1981). A note on low-frequency equatorial basin modes. *Journal of Physical Oceanography*, 11, 1578–1584. https://doi.org/10.1175/1520-0485(1981)011h1578:ANOLFEi2.0.CO;2

Claus, M., Greatbatch, R. J., & Brandt, P. (2014). Influence of the barotropic mean flow on the width and the structure of the Atlantic equatorial deep jets. *Journal of Physical Oceanography*, 44, 2485–2497. https://doi.org/10.1175/JPO-D-14-0056.1

Claus, M., Greatbatch, R. J., Brandt, P., & Toole, J. M. (2016). Forcing of the Atlantic equatorial deep jets derived from observations. *Journal of Physical Oceanography*, 46, 3549–3562. https://doi.org/10.1175/JPO-D-16-0140.1

Cravatte, S., Kessler, W. S., & Marin, F. (2012). Intermediate zonal jets in the Tropical Pacific Ocean observed by argo floats. *Journal of Physical Oceanography*, 42, 1475–1485. https://doi.org/10.1175/JPO-D-11-0206.1

Cravatte, S., Kestenare, E., Marin, F., Dutrieux, P., & Firing, E. (2017). Subthermocline and intermediate zonal currents in the Tropical Pacific Ocean: Paths and vertical structure. *Journal of Physical Oceanography*, 47, 2305–2324. https://doi.org/10.1175/JPO-D-17-0043.1

d'Orgeville, M., Hua, B. L., & Sasaki, H. (2007). Equatorial deep jets triggered by a large vertical scale variability within the western boundary layer. *Journal of Marine Research*, 65, 1–25. https://doi.org/10.1357/002224007780388720

Dietze, H., & Loeptien, U. (2013). Revisiting "nutrient trapping" in global coupled biogeochemical ocean circulation models. *Global Biogeochemical Cycles*, 27, 265–284. https://doi.org/10.1002/gbc.20029

Edelson, R. A., & Krolik, J. H. (1988). The discrete correlation function: A new method for analyzing unevenly sampled variability data. *The Astrophysical Journal*, 333, 646–659. https://doi.org/10.1086/166773

24

Firing, E. (1987). Deep zonal currents in the central equatorial Pacific. *Journal of Marine Research*, *45*, 791–812. https://doi.org/10.1357/002224087788327163

Getzlaff, J., & Dietze, H. (2013). Effects of increased isopycnal diffusivity mimicking the unresolved equatorial intermediate current system in an Earth system climate model. *Geophysical Research Letters*, *40*, 2166–2170. https://doi.org/10.1002/grl.50419

Gouriou, Y., Bourlès, B., Mercier, H., & Chuchla, R. (1999). Deep jets in the equatorial Atlantic Ocean. *Journal of Geophysical Research*, *104*, 21,217–21,226. https://doi.org/10.1029/1999JC900057

Greatbatch, R. J., Brandt, P., Claus, M., Didwischus, S.-H., & Fu, Y. (2012). On the width of the equatorial deep jets. *Journal of Physical Oceanography*, *42*, 1729–1740. https://doi.org/10.1175/JPO-D-11-0238.1

Greatbatch, R. J., Claus, M., Brandt, P., Matthießen, J.-D., Tuchen, F. P., Ascani, F., et al. (2018). Evidence for the maintenance of slowly varying equatorial currents by intraseasonal variability. *Geophysical Research Letters*, *45*, 1923–1929. https://doi.org/10.1002/2017GL076662

Hayes, S. P., & Milburn, H. B. (1980). On the vertical structure of velocity in the eastern equatorial Pacific. *Journal of Physical Oceanography*, *10*, 633–635. https://doi.org/10.1175/1520-0485(1980)010h0633:OTVSOVi2.0.CO;2

Hua, B. L., d'Orgeville, M., Fruman, M. D., Ménesguen, C., Schopp, R., Klein, P., & Sasaki, H. (2008). Destabilization of mixed Rossby gravity waves and the formation of equatorial zonal jets. *Journal of Fluid Mechanics*, *610*, 311–341. https://doi.org/10.1017/S0022112008002656

Hunter, J. D. (2007). Matplotlib: A 2D graphics environment. *Computing in Science & Engineering*, *9*(3), 90–95. https://doi.org/10.1109/MCSE.2007.55

Johnson, G. C., Kunze, E., McTaggart, K. E., & Moore, D. W. (2002). Temporal and spatial structure of the equatorial deep jets in the Pacific Ocean. *Journal of Physical Oceanography*, *32*, 3396–3407. https://doi.org/10.1175/1520-0485(2002)032<3396:TASSOT>2.0.CO;2

Johnson, G. C., & Zhang, D. (2003). Structure of the Atlantic Ocean equatorial deep jets. *Journal of Physical Oceanography*, *33*, 600–609. https://doi.org/10.1175/1520-0485(2003)033<0600:SOTAOE>2.0.CO;2

Kalnay, E., Kanamitsu, M., Kistler, R., Collins, W., Deaven, D., Gandin, L., et al. (1996). The NCEP/NCAR 40-year reanalysis project. *Bulletin of the American Meteorological Society*, *77*, 437–471. https://doi.org/10.1175/1520-0477(1996)077<0437:TNYRP>2.0.CO;2

Kiko, R., Biastoch, A., Brandt, P., Cravatte, S., Hauss, H., Hummels, R., et al. (2017). Biological and physical influences on marine snowfall at the equator. *Nature Geoscience*, *10*, 852–858. https://doi.org/10.1038/NGEO3042

Kistler, R., Kalnay, E., Collins, W., Saha, S., White, G., Woollen, J., et al. (2001). The NCEP/NCAR 50-year reanalysis: Monthly means CD-ROM and documentation. *Bulletin of the American Meteorological Society*, *82*, 247–268. https://doi.org/10.1175/1520-0477(2001)082<0247:TNNYRM>2.3.CO;2

Lebedev, K. V., Yoshinari, H., Maximenko, N. A., & Hacker, P. W. (2007). YoMaHa'07: Velocity data assessed from trajectories of Argo floats at parking level and at the sea surface (*IPRC Technical Note No. 4(2) 16 p*). updated as of November 2019.

Leetmaa, A., & Spain, P. F. (1981). Results from a velocity transect along the equator from 125 to 159° W. *Journal of Physical Oceanography*, *11*, 1030–1033. https://doi.org/10.1175/1520-0485(1981)011<1030:RFAVTA>2.0.CO;2

Locarnini, R. A., Mishonov, A. V., Baranova, O. K., Boyer, T. P., Zweng, M. M., Garcia, H. E., et al. (2019). World Ocean Atlas 2018, Volume 1: Temperature (*A. Mishonov, Technical Ed.*): NOAA Atlas NESDIS.

Lomb, N. R. (1976). Least-squares frequency analysis of unequally spaced data. *Astrophysics and Space Science*, *39*, 447–462. https://doi.org/10.1007/BF00648343

Luyten, J. R., & Swallow, J. C. (1976). Equatorial undercurrents. *Deep-Sea Research*, *23*, 999–1001. https://doi.org/10.1016/0011-7471(76)90830-5

Madec, G., Bourdallé-Badie, R., Bouttier, P.-A., Bricaud, C., Bruciaferri, D., Calvert, D., et al. (2017). NEMO ocean engine. *Notes du Pôle de modélisation de l'Institut Pierre-Simon Laplace (IPSL), 27*. https://doi.org/10.5281/zenodo.3248739

Matthießen, J.-D., Greatbatch, R. J., Brandt, P., Claus, M., & Didwischus, S.-H. (2015). Influence of the equatorial deep jets on the north equatorial countercurrent. *Ocean Dynamics*, *65*, 1095–1102. https://doi.org/10.1007/s10236-015-0855-5

Matthießen, J.-D., Greatbatch, R. J., Claus, M., Ascani, F., & Brandt, P. (2017). The emergence of equatorial deep jets in an idealised primitive equation model: An interpretation in terms of basin modes. *Ocean Dynamics*, *67*, 1511–1522. https://doi.org/10.1007/s10236-017-1111-y

Ménesguen, C., Delpech, A., Marin, F., Cravatte, S., Schopp, F., & Morel, Y. (2019). Observations and mechanisms for the formation of deep equatorial and tropical circulation. *Earth and Space Science*, *6*, 370–386. https://doi.org/10.1029/2018EA000438

Ménesguen, C., Hua, B. L., Fruman, M. D., & Schopp, R. (2009). Dynamics of the combined extra-equatorial and equatorial deep jets in the Atlantic. *Journal of Marine Research*, *67*, 323–346. https://doi.org/10.1357/002224009789954766

Najjar, R. G., Sarmiento, J. L., & Toggweiler, J. R. (1992). Downward transport and fate of organic matter in the ocean: Simulations with a general circulation model. *Global Biogeochemical Cycles*, *6*, 45–76. https://doi.org/10.1029/91GB02718

Pacanowski, R. C., & Philander, S. G. H. (1981). Parameterization of vertical mixing in numerical models of tropical oceans. *Journal of Physical Oceanography*, *11*, 1443–1451. https://doi.org/10.1175/1520-0485(1981)011<1443:POVMIN>2.0.CO;2

Qiu, B., Chen, S., & Sasaki, H. (2013). Generation of the north equatorial undercurrent jets by triad baroclinic Rossby wave interactions. *Journal of Physical Oceanography*, *43*, 2682–2698. https://doi.org/10.1175/JPO-D-13-099.1

Scargle, J. D. (1982). Studies in astronomical time series analysis. II. Statistical aspects of spectral analysis of unevenly spaced data. *The Astrophysical Journal*, *263*, 835–853. https://doi.org/10.1086/160554

Youngs, M. K., & Johnson, G. C. (2015). Basin-wavelength equatorial deep jet signals across three oceans. *Journal of Physical Oceanography*, *45*, 2134–2148. https://doi.org/10.1175/JPO-D-14-0181.1

Zweng, M. M., Reagan, J. R., Seidov, D., Boyer, T. P., Locarnini, R. A., Garcia, H. E., et al. (2019). World Ocean Atlas 2018, Volume 2: Salinity (*A. Mishonov, Technical Ed.*): NOAA Atlas NESDIS.

25

Supporting Information for "Equatorial deep jets and their influence on the mean equatorial circulation in an idealized ocean model forced by intraseasonal momentum flux convergence"

Swantje Bastin[1], Martin Claus[1,2], Peter Brandt[1,2], Richard J. Greatbatch[1,2]

[1]GEOMAR Helmholtz Centre for Ocean Research, Kiel, Germany

[2]Faculty of Mathematics and Natural Sciences, Kiel University, Kiel, Germany

Contents of this file

1. Texts S1 to S4

2. Figures S1 to S7

Corresponding author: Swantje Bastin, GEOMAR Helmholtz Centre for Ocean Research, Düsternbrooker Weg 20, 24105 Kiel, Germany, sbastin@geomar.de, sbastin@posteo.de

April 19, 2020, 1:58pm

Introduction

This Supporting Information contains a more detailed description of the model param-
eters used in the study than it was possible to give in the main article, and a detailed
description of the analysis of the Argo data. Additionally, a brief comparison of the
modelled EDJ and EDJ observed at a current meter mooring at the equator at 23°W is
given to justify our analysis of EDJ in a simplified model study. Finally, two figures that
show the robustness of the generated mean flow pattern for different EDJ amplitudes are
included.

April 19, 2020, 1:58pm

Text S1. Extended model description

Our model is set up as an idealized tropical Atlantic basin. It is rectangular, with a uniform depth of 5000 m, extending from 20°S to 20°N and over 55° longitude, mimicking the width of the Atlantic at the equator which is an important factor for simulating the Atlantic EDJ because of their resemblance to an equatorial resonant basin mode. The horizontal resolution is set to 0.25° in both latitude and longitude. The vertical resolution is higher than usually employed in ocean models – we use 200 model levels that are spaced 5 m apart close to the surface and 50 m apart close to the bottom. The level spacing in the entire water column can be seen in Figure S1.

The vertical mixing formulation is Richardson number dependent, following Pacanowski and Philander (1981); in the horizontal, biharmonic diffusivity is used for both tracers and momentum. For a complete list of parameters used see the model namelist that is provided as part of the supplemental dataset (URL in Acknowledgments in the main text). Most of our parameter choices follow Ascani et al. (2015) and Matthießen et al. (2015).

The model is initialized with basin-averaged vertical profiles of temperature and salinity from the World Ocean Atlas (WOA) 2018 (Locarnini et al., 2019; Zweng et al., 2019). Given as in-situ temperature and practical salinity in the WOA, they are converted into conservative temperature and absolute salinity using the TEOS-10 Gibbs Sea Water library Python implementation (gsw 3.3.1) to be compatible with the NEMO implementation of the equation of state. Throughout the simulations, temperature and salinity at the model ocean surface are restored towards the initial values with a time scale of 30 days to at least partly sustain the original density stratification in the water column. In

April 19, 2020, 1:58pm

fact, the model thermocline does diffuse a little in the course of our simulations, but over the time of a little less than 150 years over which we run the model the change is small enough that the effect can be neglected.

All simulations are started from rest and run until a quasi-steady circulation has developed, which takes about 60 years in the Sim-WIND case and less than 10 years in the Sim-IMFC case. After this spin-up phase, the model is run for 80 years, and these 80 years are then analyzed.

Text S2. Argo analysis

The dataset of velocities from Argo float data that we used for this study is the YoMaHa'07 dataset (Lebedev et al., 2007). It is updated regularly; our version has been downloaded on November 4, 2019 (covering a time period of approximately 20 years, from 2000 to October 2019). The velocities at the floats' parking depth have been calculated from the positions of the float's descent, ascent and the time it spent at depth. For more details on this please see Lebedev et al. (2007) directly.

From this dataset, we used only the zonal velocity, and we chose only the data points that are located in the tropical Atlantic and at a nominal float parking depth of 1000 m, i.e. well inside the main depth interval of the EDJ. Luckily for us, 1000 m is the most abundant parking depth in the Argo float data; although other depths are available, the data coverage is much sparser there. A first impression of the data coverage and the time mean zonal velocity field (binned spatially into $0.1° \times 0.1°$ areas) can be seen in Figure S2. Although the resulting field has a lot of regions with missing data, it gives a

April 19, 2020, 1:58pm

generally good first impression of what the time mean velocity field looks like. Away from the equator, the zonal velocity is arranged in narrow zonal bands, alternately flowing to the west and to the east with increasing distance from the equator. These current bands have been termed the Equatorial Intermediate Current System and have been described in many other studies (cf. e.g. Ascani et al., 2010; Cravatte et al., 2012). Very close to the equator, however, in the region that is of interest in the context of this study, the structure of the mean velocity field is not very clear - the noise due to the periodically reversing EDJ is strongly apparent.

If we look at the temporal coverage of the data, the sampling is generally not evenly distributed over positive and negative EDJ phases, leading to a potential bias in the time mean. Hence, if we want to find the structure of the time mean zonal flow close to the equator, we have to remove the harmonic associated with the EDJ before taking the time average. However, the sampling is not only unevenly distributed, but even at 1000 m depth still relatively sparse, such that we have to spatially smooth the time mean field to be able to fit temporal harmonics to the data, and also to clearly see the dominant structures. For this purpose, we first calculate the spatial decorrelation scales of the raw time mean zonal velocity field, such that we do not apply smoothing on scales larger than those on which the velocity field can be assumed to be coherent.

To calculate the decorrelation scales of the mean velocity field, we use the technique of correlation slotting (Edelson & Krolik, 1988). This is a technique to obtain an estimate of the autocorrelation function of irregularly sampled data. First, the product of every possible combination of two data points is calculated, to be then binned according to the

April 19, 2020, 1:58pm

temporal lag or spatial separation of the two data points (in our case this is applied in two spatial dimensions). The resulting autocovariance field can be normalized, yielding the estimated autocorrelation as a function of spatial distance in latitude and longitude (shown for the Argo zonal velocity data from 1000 m depth in Figure S3). We calculated the spatial autocorrelation of the mean velocity field from all data points between 7°S and 7°N, i.e. all data shown in Figure S2.

As we only look at points that are less than 7° away from the equator, we calculate the spatial separation in degrees and neglect the changing length of one degree of longitude with increasing latitude, the scaling factor with the maximum deviation from one being $\cos(7°) \approx 0.99$.

In Figure S3, the e-folding scale of the autocorrelation is indicated with the black line. The field is too noisy to obtain an exact estimate, but it seems safe to assume that the decorrelation scales are at least 7.5° in the x-direction and 0.3° in the y-direction, consistent with the much larger zonal than meridional coherence of the zonal flow field.

In order to remove the EDJ harmonic and smooth the resulting time mean field, we first bin the Argo velocity data into spatial bins of $0.1° \times 0.1°$ and temporal bins of 7 days. Taking such relatively small bin sizes ensures that we do not lose too much information. We then construct a time series for every point (x_0, y_0) on a $0.2° \times 0.2°$ grid by, for each time step, calculating the weighted average of the velocities over a spatial influence ellipse $w(x, y)$ defined by a two-dimensional normal distribution with standard deviations of half our estimated decorrelation scales, i.e. $\sigma_x = 3.75°$, $\sigma_y = 0.15°$:

$$w(x, y) = \exp\left(-\left(\frac{(x - x_0)^2}{2\sigma_x^2} + \frac{(y - y_0)^2}{2\sigma_y^2}\right)\right) \cdot \frac{1}{W} \tag{1}$$

April 19, 2020, 1:58pm

The edge of the influence ellipse is defined by $w(x, y) = \exp(-3) \approx 0.05$; values that lie outside this are not considered for the average. The weights are given by the Gaussian function $w(x, y)$ itself, such that measurements are given less weight the further they are away from the point (x_0, y_0). To retain the physical amplitude of the average, w has to be normalized at each point separately, because due to the sparsity of our dataset the number and distribution of measurements available for the average varies. W is the sum of values of w at all points where $w > \exp(-3)$ and the velocity field u is defined. The spatially averaged velocity $u_{smoothed}$ at (x_0, y_0) and at time t is then just given as

$$u_{smoothed}(x_0, y_0, t) = \sum_{x,y}(u(x, y, t) \cdot w(x, y)) \tag{2}$$

We now have a spatially smoothed zonal velocity field, and with this also time series at every point that are much less sparse than in the unsmoothed data, enabling us to fit harmonics to the velocity field. For this, we use a Python implementation (from astropy 3.2.3) of the Lomb-Scargle periodogram (Lomb, 1976; Scargle, 1982), which fits sinusoidal curves at frequencies corresponding to a discrete fourier transform to unevenly sampled time series. The EDJ, here at a period of 4.57 years, appear as the dominant interannual peak in the spectrum.

At every point (x_0, y_0), we apply the Lomb-Scargle harmonic fit to the smoothed time series and remove the EDJ harmonic before calculating the final time average.

In Figure S4, the effect of the smoothing with the help of the spatial influence ellipse can be seen in Panel a. There, the EDJ harmonic has not been removed. The time mean velocity field without the EDJ harmonic is shown in Panel b. Panel c shows the time mean (non-zero due to the effect of irregular sampling) of the removed EDJ harmonic.

April 19, 2020, 1:58pm

We have additionally tried a different method to remove the bias in the time average due to irregular sampling of the EDJ phases, where we calculated the ratio of measurements taken during positive EDJ phases to measurements taken during negative EDJ phases for each point. We then used this ratio to upweight measurements taken during the undersampled phase and downweight measurements taken during the oversampled phase. This method, however, increases the amount of noise in our data, so that we do not use it here. Nevertheless, we obtained very similar results as those shown in Figure S4, increasing confidence in our resulting time mean velocity field.

Text S3. Validation of model EDJ against observations

Because our model setup is highly idealized, we think it important to show a comparison of the main characteristics of the EDJ in our model to the EDJ measured in the real ocean, justifying our choice of a simplified model for studying the EDJ. Figure S5 shows Hovmöller diagrams and normal mode spectra for our two model experiments (Sim-WIND and Sim-IMFC, as also shown in the main text), as well as for observations from 23°W, obtained from different moorings and shipboard measurements (cf. Bunge et al., 2008; Brandt et al., 2011; Claus et al., 2016). The analysis of the observational data is updated from e.g. Claus et al. (2016); Greatbatch et al. (2018).

Overall, the EDJ in the model simulations exhibit similar characteristics as the observed EDJ, both being the dominant interannual peak in the spectrum at a period of roughly 4.5 years, and lying approximately on the equatorial basin mode resonance curve. However, the observed EDJ peak at mode 17, whereas the simulated EDJ have their maximum at

April 19, 2020, 1:58pm

mode 19. Also, the modal distribution is much broader in observations, where the EDJ peak in the spectrum spans at least modes 14 to 20, if not 10 to 20, than in the model runs, where the EDJ are only comprised of modes 18 to 20. The amplitude of the EDJ in the models is a bit too small compared to observations. This might pose a problem in the analysis of the nonlinear effects of the EDJ, as discussed in the main text. In the observations, there is a clear annual signal (as well as a semi-annual signal, not shown in the spectrum), both of which are not present in the model simulations. This is due to the steady, time averaged wind forcing applied to Sim-WIND, and it is intentional, since we are only interested in the interannual flow variability in this study.

Text S4. Dependence of generated mean flow strength on EDJ amplitude

We have done an additional model run where we changed the amplitude of the IMFC forcing. Although this is not the focus of the main article (where we deliberately did not tune the strength of the IMFC forcing but kept it at the amplitude that we diagnosed from Sim-WIND), we show two figures here because they add some confidence to the mean zonal flow field at intermediate depths that is generated by the EDJ in Sim-IMFC.

Figure S6 shows the mean zonal flow field at 1000 m depth from Sim-IMFC, as shown in the main article, as well as from the additional model run (Sim-doubledIMFC) that we forced with doubled IMFC amplitude, resulting in an approximate doubling of the EDJ amplitude. As in Sim-IMFC, no other forcing (e.g. wind) has been applied to Sim-doubledIMFC. The structure of the generated mean flow stays the same with increasing EDJ amplitude.

<center>April 19, 2020, 1:58pm</center>

The amplitude of the generated mean flow, however, obviously depends strongly on the EDJ amplitude. Figure S7 shows the mean zonal flow along the equator, averaged over all depths between 500 and 1800 m (the structure of the mean flow is very similar on all depths over this range) from the two model runs. One can see that the increase is considerably larger than linear, in some places exceeding quadratic. This is not surprising given that the energy transfer from the EDJ to the mean flow happens through $-\partial \overline{(u'u')}/\partial x$ (the overline denoting the time mean, the prime denoting deviations from the time mean), as shown in the main article.

References

Ascani, F., Firing, E., Dutrieux, P., McCreary, J. P., & Ishida, A. (2010). Deep Equatorial Ocean Circulation Induced by a Forced-Dissipated Yanai Beam. *Journal of Physical Oceanography*, *40*, 1118–1142. doi: 10.1175/2010JPO4356.1

Ascani, F., Firing, E., McCreary, J. P., Brandt, P., & Greatbatch, R. J. (2015). The Deep Equatorial Ocean Circulation in Wind-Forced Numerical Solutions. *Journal of Physical Oceanography*, *45*, 1709–1734. doi: 10.1175/JPO-D-14-0171.1

Brandt, P., Funk, A., Hormann, V., Dengler, M., Greatbatch, R. J., & Toole, J. M. (2011). Interannual atmospheric variability forced by the deep equatorial Atlantic Ocean. *Nature*, *473*, 497–500. doi: 10.1038/nature10013

Bunge, L., Provost, C., Hua, B. L., & Kartavtseff, A. (2008). Variability at Intermediate Depths at the Equator in the Atlantic Ocean in 2000–06: Annual Cycle, Equatorial Deep Jets, and Intraseasonal Meridional Velocity Fluctuations. *Journal of Physical Oceanography*, *38*, 1794–1806. doi: 10.1175/2008JPO3781.1

April 19, 2020, 1:58pm

Claus, M., Greatbatch, R. J., Brandt, P., & Toole, J. M. (2016). Forcing of the Atlantic Equatorial Deep Jets Derived from Observations. *Journal of Physical Oceanography*, *46*, 3549–3562. doi: 10.1175/JPO-D-16-0140.1

Cravatte, S., Kessler, W. S., & Marin, F. (2012). Intermediate Zonal Jets in the Tropical Pacific Ocean Observed by Argo Floats. *Journal of Physical Oceanography*, *42*, 1475–1485. doi: 10.1175/JPO-D-11-0206.1

Edelson, R. A., & Krolik, J. H. (1988). The discrete correlation function: A new method for analyzing unevenly sampled variability data. *The Astrophysical Journal*, *333*, 646–659. doi: 10.1086/166773

Greatbatch, R. J., Claus, M., Brandt, P., Matthießen, J.-D., Tuchen, F. P., Ascani, F., . . . Farrar, J. T. (2018). Evidence for the Maintenance of Slowly Varying Equatorial Currents by Intraseasonal Variability. *Geophysical Research Letters*, *45*, 1923–1929. doi: 10.1002/2017GL076662

Lebedev, K. V., Yoshinari, H., Maximenko, N. A., & Hacker, P. W. (2007). YoMaHa'07: Velocity data assessed from trajectories of Argo floats at parking level and at the sea surface. *IPRC Technical Note No. 4(2)*, 16 p. (updated as of November 2019)

Locarnini, R. A., Mishonov, A. V., Baranova, O. K., Boyer, T. P., Zweng, M. M., Garcia, H. E., . . . Smolyar, I. V. (2019). World Ocean Atlas 2018, Volume 1: Temperature. *NOAA Atlas NESDIS*, *81*, 52 pp. (A. Mishonov, Technical Ed.)

Lomb, N. R. (1976). Least-squares frequency analysis of unequally spaced data. *Astrophysics and Space Science*, *39*, 447–462. doi: 10.1007/BF00648343

Matthießen, J.-D., Greatbatch, R. J., Brandt, P., Claus, M., & Didwischus, S.-H. (2015).

April 19, 2020, 1:58pm

Influence of the equatorial deep jets on the north equatorial countercurrent. *Ocean Dynamics*, *65*, 1095–1102. doi: 10.1007/s10236-015-0855-5

Pacanowski, R. C., & Philander, S. G. H. (1981). Parameterization of Vertical Mixing in Numerical Models of Tropical Oceans. *Journal of Physical Oceanography*, *11*, 1443–1451. doi: 10.1175/1520-0485(1981)011⟨1443:POVMIN⟩2.0.CO;2

Scargle, J. D. (1982). Studies in astronomical time series analysis. II. Statistical aspects of spectral analysis of unevenly spaced data. *The Astrophysical Journal*, *263*, 835–853. doi: 10.1086/160554

Zweng, M. M., Reagan, J. R., Seidov, D., Boyer, T. P., Locarnini, R. A., Garcia, H. E., . . . Smolyar, I. V. (2019). World Ocean Atlas 2018, Volume 2: Salinity. *NOAA Atlas NESDIS*, *82*, 50 pp. (A. Mishonov, Technical Ed.)

April 19, 2020, 1:58pm
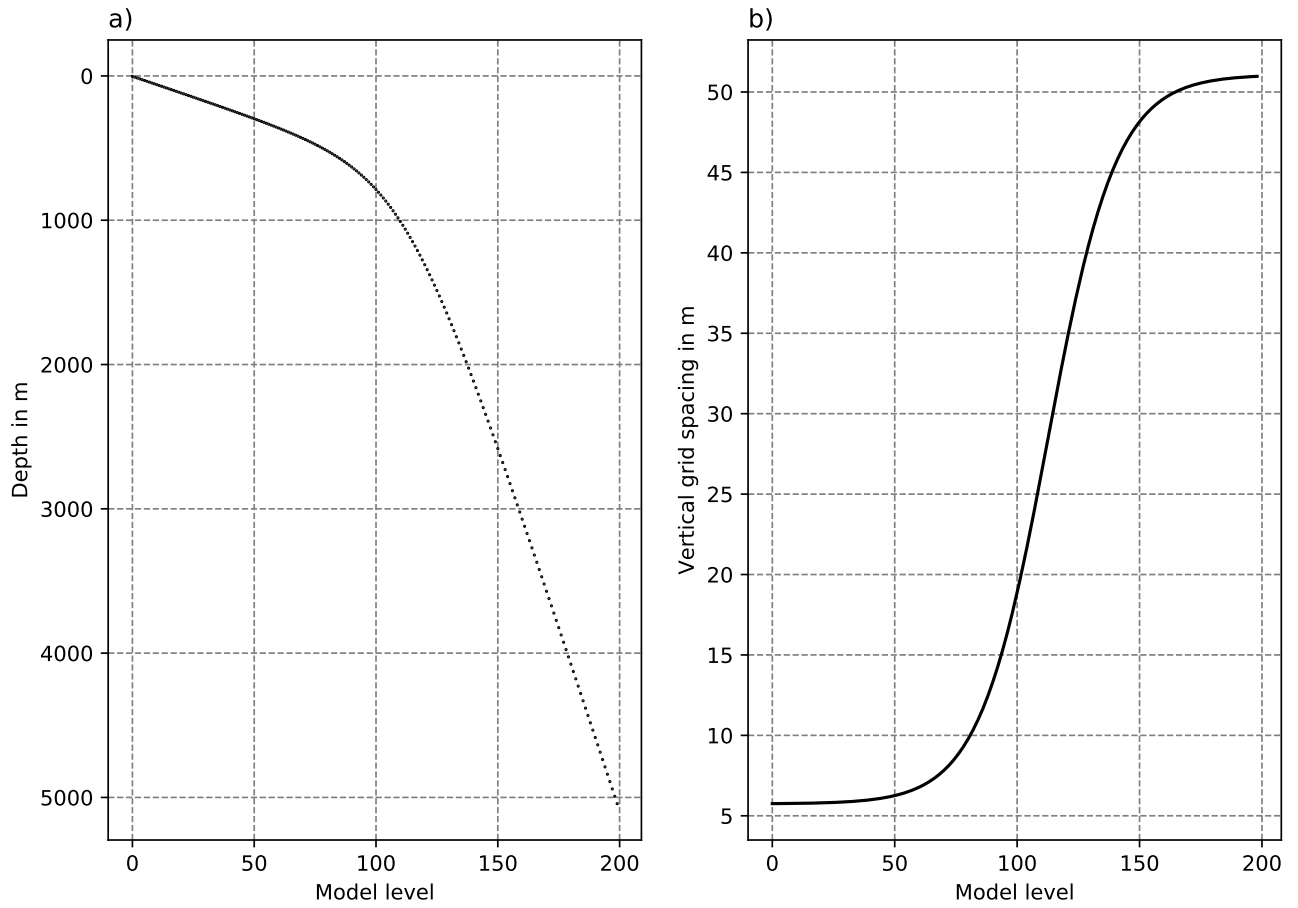
Figure S1.   Setup of the vertical axis. In the left panel, the placement of each model level along the depth axis is shown (each level indicated by a black dot). In the right panel, the resulting vertical grid spacing is shown.

April 19, 2020, 1:58pm
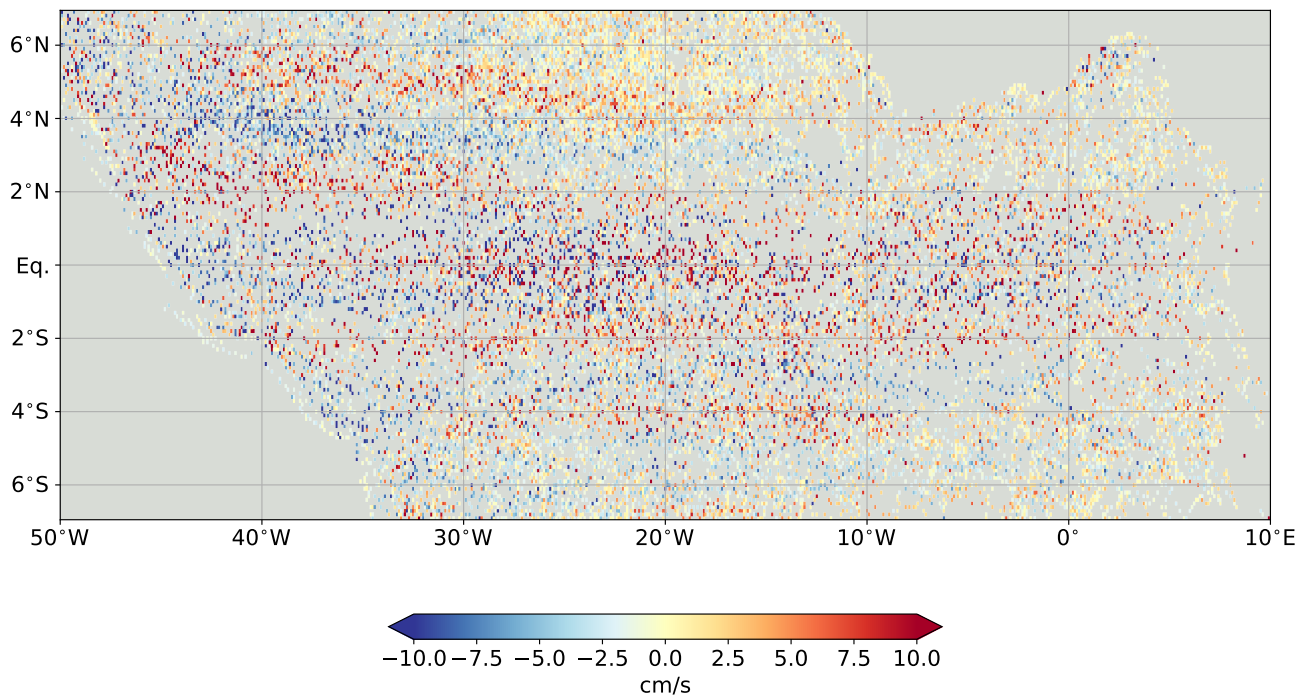
Figure S2.   Time mean zonal velocity at $1000\,\mathrm{m}$ depth from Argo data, binned into $0.1° \times 0.1°$ spatial bins

April 19, 2020, 1:58pm
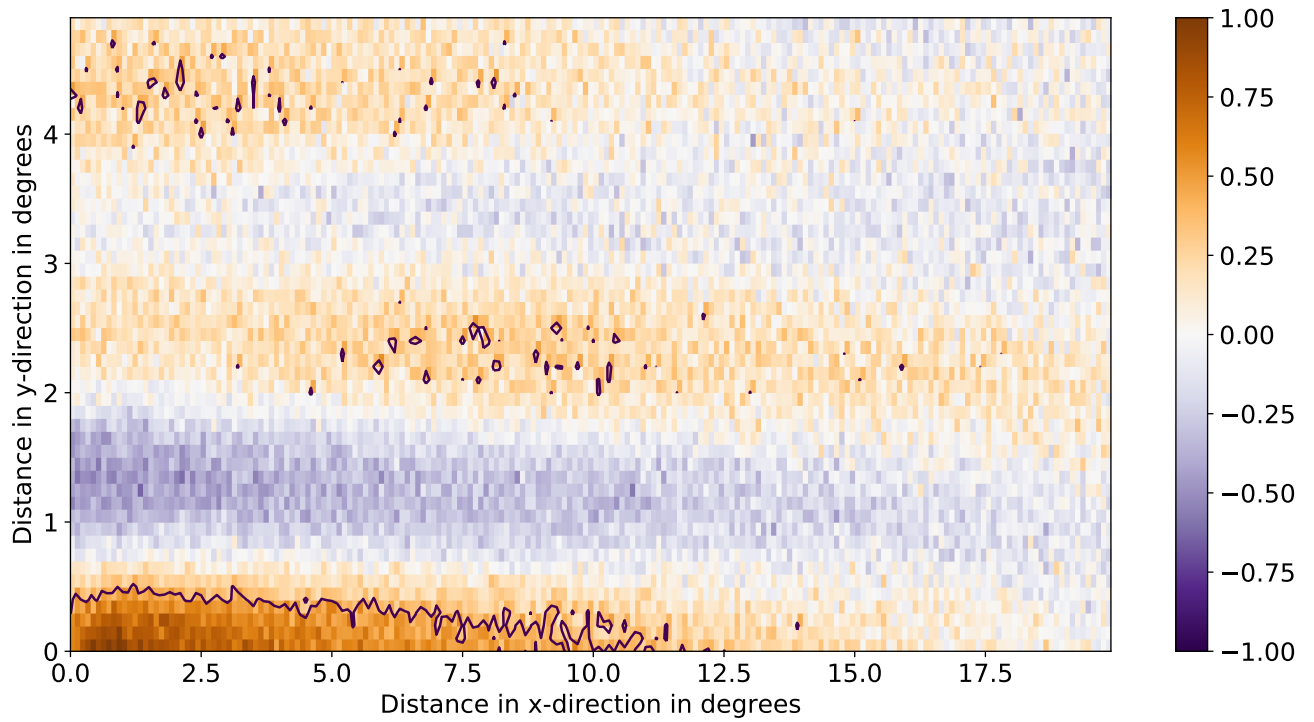
Figure S3.   Spatial decorrelation scales of time mean zonal velocity at $1000\,\mathrm{m}$ depth in the tropical Atlantic between 7°S and 7°N from Argo data. The color shading shows the autocorrelation (details see text), the black contour at a value of 0.37 indicates the e-folding scale.

April 19, 2020, 1:58pm
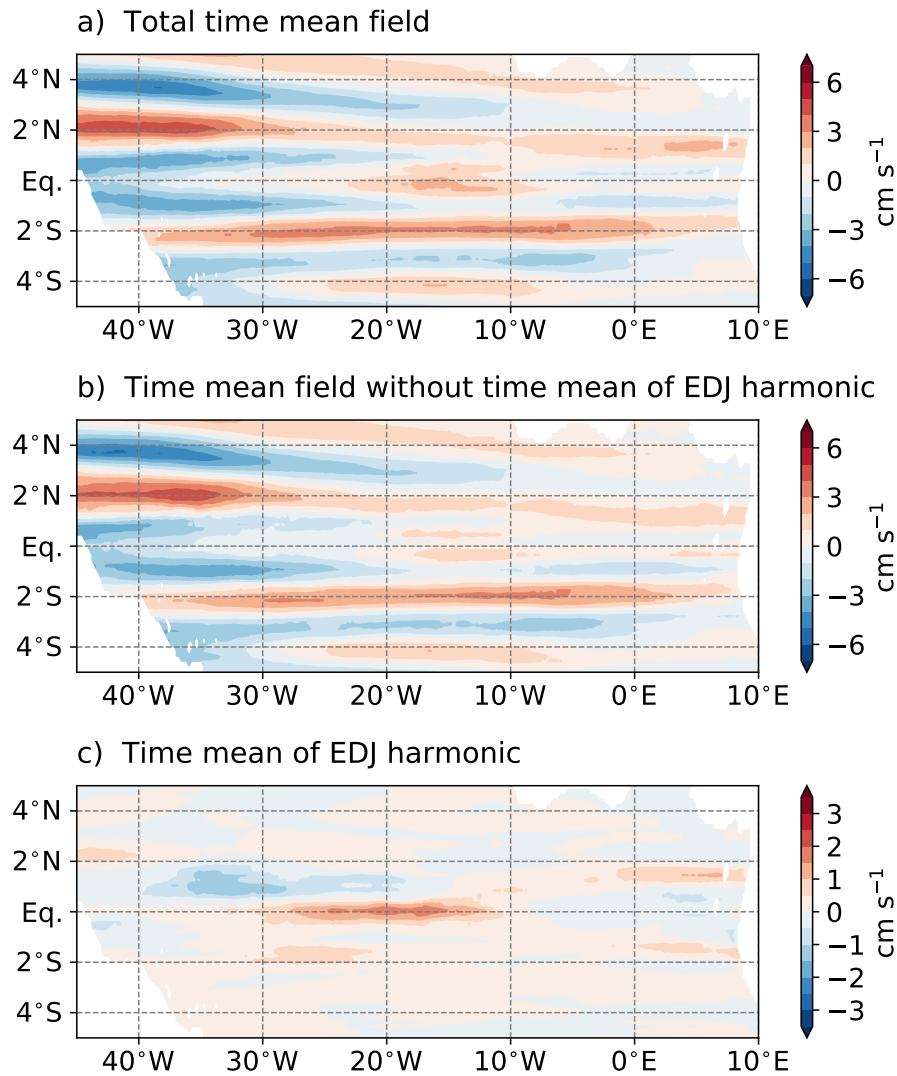
Figure S4.   Effects of the removal of the EDJ bias on the time mean field of zonal velocity at 1000 m depth from Argo data. For details see text.

April 19, 2020, 1:58pm
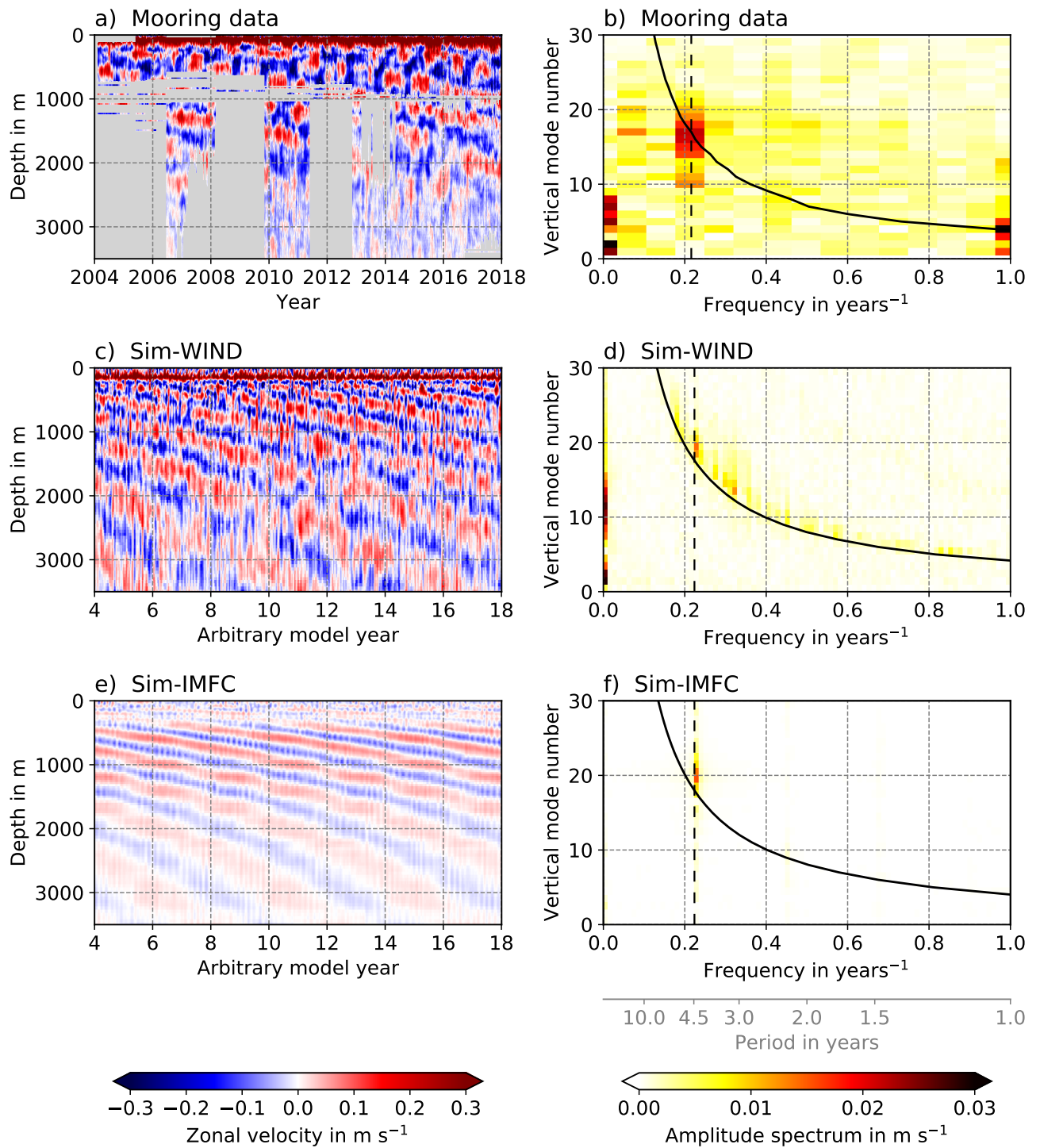
Figure S5. Comparison of observed Atlantic EDJ and the simulated EDJ. (Cont. next page)

April 19, 2020, 1:58pm

43

Figure S5.   (previous page.) Panels a, c, and e show Hovmöller diagrams of zonal velocity at 23°W, Panels b, d and f show amplitude spectra of the zonal velocity after its decomposition into vertical normal modes. The dashed black lines indicate the dominant EDJ frequency, the solid black line the resonance curve of equatorial basin modes (see main text, Eq. 1). The difference in frequency resolution between mooring data and model output is due to the fact that we only have 14 years of observational data compared to 80 years of model output. Panels a and b are updated from e.g. Claus et al. (2016); Greatbatch et al. (2018).
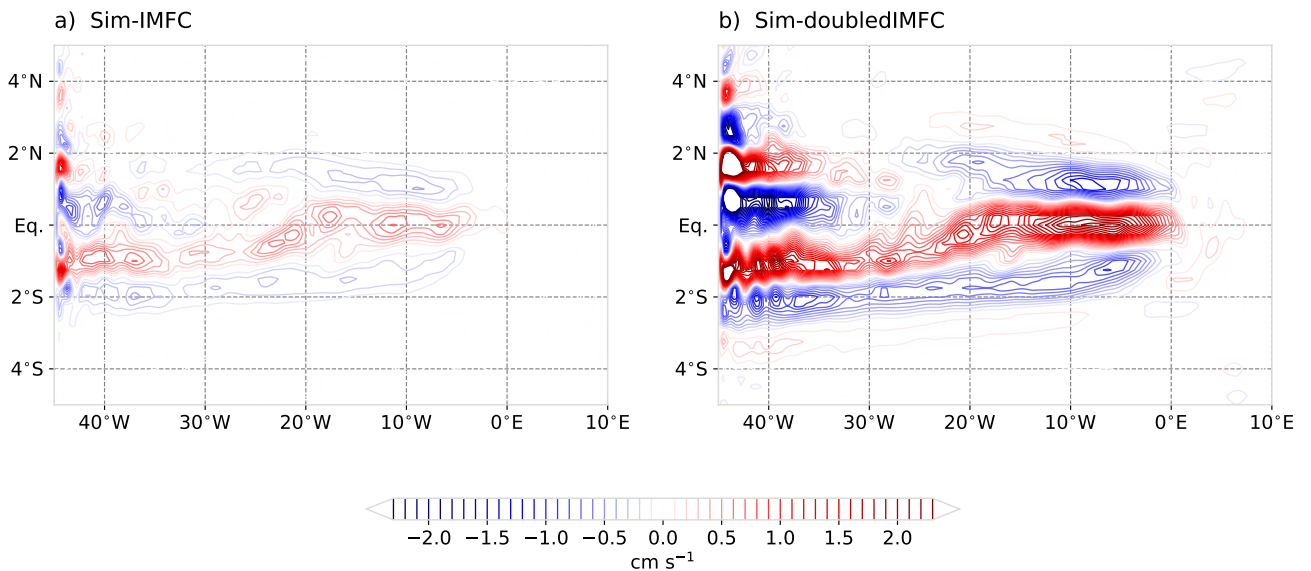
Figure S6.   Time mean zonal flow at 1000 m depth generated by EDJ in a model forced by different amplitudes of IMFC (details see text). The EDJ in Sim-doubledIMFC have approximately twice the amplitude of the EDJ in Sim-IMFC.

April 19, 2020, 1:58pm
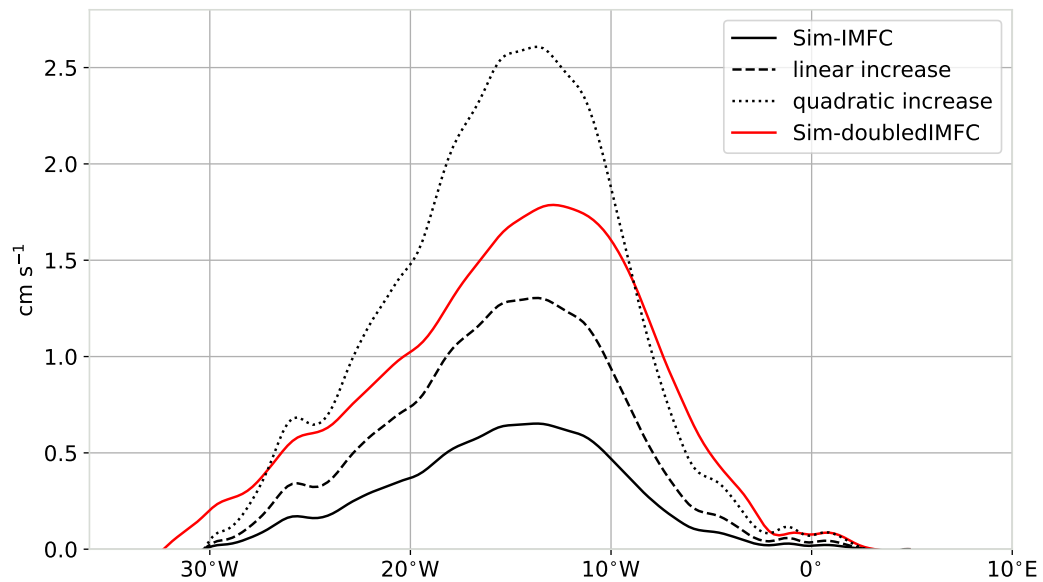
Figure S7.   Increase of mean flow generated by EDJ when IMFC forcing amplitude is doubled. Shown is the time mean zonal flow along the equator, averaged over all depths between 500 and 1800 m. The dashed respectively dotted line are twice respectively four times the Sim-IMFC mean flow, meaning linear respectively quadratic increase of mean flow with increasing EDJ amplitude.

April 19, 2020, 1:58pm

3 Atlantic equatorial deep jets in Argo float data

To be published as: **Bastin, S., Claus, M., Brandt, P., and Greatbatch, R. J.: Atlantic equatorial deep jets in Argo float data.** *Submitted to: Journal of Physical Oceanography.*

The candidate's contributions to the publication are as follows:

- She developed the research question and conceptual design of the article.

- She performed all analyses.

- She produced all figures.

- She authored the manuscript from the first draft to the final (submitted) version.

Atlantic equatorial deep jets in Argo float data

Swantje Bastin*

GEOMAR Helmholtz Centre for Ocean Research, Kiel, Germany

Martin Claus, Peter Brandt, and Richard J. Greatbatch

GEOMAR Helmholtz Centre for Ocean Research, Kiel, Germany; Faculty of Mathematics and Natural Sciences, Kiel University, Kiel, Germany

ABSTRACT

Equatorial deep jets (EDJ) are zonal currents along the equator in all three ocean basins that alternate in direction with depth and time. In the Atlantic below the thermocline, they are the dominant variability on interannual timescales. They propagate energy upwards and are suggested to impact surface climate variables. They are also important for the distribution of tracer in the mid-depth tropical ocean, for example by enhanced oxygen ventilation of the eastern oxygen minimum zones. Observations of equatorial deep jets are available but scarce, given the EDJs' location at depth and their long periodicity of several years. In the last few years, Argo floats have added a significant amount of measurements at intermediate depth. In this study we therefore revise estimates of the EDJ scales based on Argo float data. Mostly, we use velocity data at 1000 m depth. Very weak or no EDJ signals can be detected in the Indian and Pacific Oceans. In the Atlantic, however, the EDJ signal is strong at 1000 m depth, allowing us to obtain robust estimates of their frequency, amplitude, phase, zonal wavelength, and meridional structure. Additionally, we present a new estimation of their vertical structure throughout the Atlantic basin, based on an equatorial geostrophic velocity reconstruction from hydrographic Argo float measurements from depths between 400 and 2000 m. Earlier studies have mostly estimated the Atlantic EDJ scales from shipboard data. Our new estimates from Argo float data thus provide an independent EDJ scale assessment, as well as having smaller uncertainties than those from earlier studies.

1. Introduction

The circulation in the tropical oceans is characterized by energetic zonal currents. Below the thermocline, there are two main current systems with flow speeds of up to $20\,\mathrm{cm\,s^{-1}}$: one takes the form of zonal jets alternating in direction with latitude (also called Equatorial Intermediate Current System, EICS, e.g. Ascani et al. 2010; Cravatte et al. 2012, 2017; Ménesguen et al. 2019; Delpech et al. 2020, 2021), which are characterized by a large vertical scale and extend to at least 15°N/S. The other consists of vertically alternating, downward propagating zonal jets that are located directly on the equator with small latitudinal extent; these are called Equatorial Deep Jets (EDJ, e.g. Youngs and Johnson 2015; Ménesguen et al. 2019). It is not entirely clear whether these current systems merely coexist separately in the equatorial oceans, or whether they share a common dynamical origin. So far, however, no attempt at a unified theory of their generation mechanisms has been successful (Ménesguen et al. 2019). Because of their large vertical extent and their temporal consistency, the EICS can be easily seen in time mean velocity data derived from Argo float measurements, and have also been well studied from shipboard measurement sections (e.g. Cravatte et al. 2012, 2017). Of the EDJ, however, we have

a less clear picture, mainly because of their vertical and temporal variability.

Equatorial Deep Jets were first identified in the Indian Ocean (Luyten and Swallow 1976), and later also in the Pacific and Atlantic Oceans (Hayes and Milburn 1980; Leetmaa and Spain 1981; Eriksen 1982). They take the form of stacked zonal jets with downward phase propagation and, consistent with linear wave theory, exhibit upward energy propagation in an idealized model simulation (Matthießen et al. 2015). Associated with the latter, the EDJ in the Atlantic Ocean have been suggested to influence surface climate parameters like wind, rainfall and sea surface temperature on interannual time scales (Brandt et al. 2011), potentially making the EDJ important for seasonal to interannual prediction in the equatorial regions. Furthermore, the comparably fast-flowing jets advect tracers, and have been shown to contribute to the ventilation of the eastern tropical oxygen minimum zones from the highly oxygenated western boundary region (Brandt et al. 2012, 2015). In addition to this, the EDJ have been suggested to generate time mean zonal flow by nonlinear self-advection (Ascani et al. 2015; Bastin et al. 2020), which is relevant to e.g. nutrient and oxygen transport in the deep ocean.

Given the EDJs' relatively small vertical scale of a few hundred meters and their temporal variability on timescales of multiple years, it is challenging to observe them. Their vertical wavelength of a few hundred meters and their am-

Corresponding author: Swantje Bastin, sbastin@geomar.de, sbastin@posteo.de

1

plitude of up to $20\,\mathrm{cm\,s^{-1}}$ at specific locations have been among the first parameters that could be estimated, from several instantaneous shipboard velocity profiles or sections (e.g. Luyten and Swallow 1976; Leetmaa and Spain 1981; Ponte et al. 1990; Gouriou et al. 1999). Later, concurrent measurements at different longitudes showed that the EDJ are zonally coherent over several tens of degrees (Gouriou et al. 2001). Johnson et al. (2002) then combined historical CTD measurements from the equatorial Pacific to extract information on the Pacific EDJ and found a slow temporal evolution; but concluded that the period of the Pacific EDJ must be significantly longer than the time span where measurements were available. A similar analysis by Johnson and Zhang (2003) in the Atlantic yielded not only information about the period, which they estimated to be 5 ± 1 years, but also about the meridional structure of the Atlantic EDJ, which they described as roughly corresponding to the meridional structure of a first meridional mode Rossby wave, widened by a factor of 1.5 compared to that expected theoretically. The temporal variation of the EDJ subsequently became better known due to the usage of moored current meters to obtain time series of velocity measurements (e.g. Bunge et al. 2006, 2008; Brandt et al. 2008). Especially useful in this context is the equatorial mooring at 23°W, having provided high-resolution velocity measurements since 2006, and being still maintained today. This moored velocity dataset has been used in a number of studies concerned with the EDJ, and has given a thorough insight into the Atlantic EDJs' temporal and vertical structure in the centre of the basin (Brandt et al. 2008, 2011, 2012; Claus et al. 2016; Greatbatch et al. 2018). The latest analysis of the basin-wide signature of the EDJ has been provided by Youngs and Johnson (2015), who did an updated analysis of available shipboard CTD profiles for all three oceans (for the Indian and Pacific Ocean they also included Argo profiles). They supplied updated estimates of temporal and vertical scales, but also of the meridional structure and zonal wavelength of the EDJ, albeit still with sizeable uncertainties and as basin-wide averages. However, as we will show in this study, the amplitude, zonal wavelength and meridional structure of the Atlantic EDJ exhibit pronounced horizontal variations within the basin.

Dynamically, the EDJ have been suggested to originate from an instability of intraseasonal waves (Hua et al. 2008) shed either by tropical instability waves (Ascani et al. 2015) or by the western boundary currents (d'Orgeville et al. 2007). The strong similarity of the EDJ to a resonant equatorial basin mode (Cane and Moore 1981) for a high baroclinic mode has been noted by several studies (e.g. d'Orgeville et al. 2007; Ascani et al. 2015; Matthießen et al. 2015, 2017), although they are broader than theoretically expected, possibly because of enhanced momentum compared to tracer dissipation in the equatorial ocean (Greatbatch et al. 2012). Equatorial basin modes consist of an eastward propagating equatorial Kelvin wave, together with its reflection as westward propagating long equatorial Rossby waves: the sum of these waves becomes resonant, for the gravest basin mode, at a period equivalent to four times the time it takes the Kelvin wave to cross the entire basin (Cane and Moore 1981). Because of this dependence on the basin width, the time scale on which the Pacific EDJ vary has been found to be much longer than that of the Atlantic and Indian Ocean EDJ (e.g. Youngs and Johnson 2015). The nature of the EDJ as a resonant sum of multiple wave components of course complicates their structure. Although Cane and Moore (1981) have provided analytic solutions to the equatorial basin modes, these are only for a linear idealized ocean, leaving it unclear what exact form they would take in the real ocean including nonlinear effects. In several studies, especially the early ones that only had access to a very limited amount of measurements, attempts have been made to attribute the EDJ variability either to an equatorial Kelvin wave or to equatorial Rossby waves, leading to conflicting results. Youngs and Johnson (2015) provided combined estimates of the contributions of the Kelvin and Rossby waves to the EDJ and concluded that in the Indian and Pacific Oceans, the two are of similar importance, whereas the Atlantic EDJ seem to be dominated by the first meridional mode Rossby wave.

With this study, we provide an updated, independent, more accurate and comprehensive description of the EDJ using the growing amount of data from the deep equatorial oceans provided by Argo floats. The Argo program has, since its beginning in 1998, brilliantly fulfilled its original aim to provide world-wide real-time measurements of temperature and salinity (in later years also additional parameters like oxygen) from the upper $2000\,\mathrm{m}$ of the oceans. Through its implementation of a global network of autonomous measuring floats, it has now provided a much larger number of hydrographic profiles than shipboard measurements, and at a much lower cost (Jayne et al. 2017). In the equatorial oceans, the number of available Argo float measurements has increased especially in the last five to ten years – these data now give us the chance to compile a more comprehensive basin-wide description of the EDJ than available so far. However, we can provide this only for the Atlantic Ocean: It has been found before that the Atlantic EDJ are stronger and more regular than those in the Pacific and Indian Oceans (e.g. Youngs and Johnson 2015), a finding that is supported by the analysis of velocity data at $1000\,\mathrm{m}$ depth presented in this study. In fact, in this data, we were not able to detect the Indian and Pacific Ocean EDJ, such that the focus of this article will be on the Atlantic EDJ only.

This article is structured as follows: Section 2 describes the datasets and analysis methods that were used. In Section 3, we present our estimation of a) the Atlantic EDJs' frequency, b) their amplitude, c) their phase and zonal wavelength, d) their meridional structure and the relative

contributions of Kelvin and Rossby waves to the EDJ signal, and e) the Atlantic EDJs' vertical structure. The results are then summarized and discussed in Section 4.

2. Data and methods

a. Data

1) VELOCITY DATA AT 1000 M DEPTH

The main dataset that we used for this study is the YoMaHa'07 dataset of "velocity data assessed from trajectories of Argo floats at parking level and at the sea surface" (Lebedev et al. 2007). The deep velocity dataset is composed of one (zonal and meridional) velocity value at the parking depth per Argo float cycle consisting of a descent to the parking depth, a floating period at this depth, and an ascent back to the surface. The velocities have been estimated from the float location before descent and after ascent, and the time spent at depth; thus they are not instantaneous velocities but averages over typically around ten days (Lebedev et al. 2007). For the analysis of equatorial deep jets, this should not pose a problem, because the interest is on much longer time scales such that the information that is lost through the average would merely be regarded as noise in the context of this study. The YoMaHa'07 dataset is updated regularly; the data that we used has been downloaded from `http://apdrc.soest.hawaii.edu/projects/ Argo/data/trjctry/yomaha07.dat.gz` on July 1, 2020, and extends to June 2020.

From this dataset, we only used data from the equatorial oceans and restricted the analysis to data from floats with a nominal parking depth of 1000 m, because at this depth the data are most abundant. Although there are some Argo floats that dive to other parking depths, e.g. 500 or 2000 m, these are so few today that, at least concerning the EDJ, no meaningful statistical analysis is possible.

In Figure 1, the zonal velocity along the equator at 1000 m depth is shown for the Atlantic Ocean. Especially since 2014, the data coverage shows a pronounced increase at this depth.

2) HYDROGRAPHIC DATA

Because the Argo floats do not measure velocity directly (making it necessary to calculate the velocity indirectly from their travel time and displacement at depth), the YoMaHa'07 deep velocity dataset only contains data points at the floats' parking depth and therefore does not allow to examine the EDJs' vertical structure. However, the Argo floats directly measure hydrographic parameters during their descent and/or ascent, making it possible to compute the instantaneous vertical structure of the density field. Because the zonal velocity associated with the EDJ is almost entirely in geostrophic balance (Eriksen 1982), the density field contains information about the vertical structure of the Atlantic EDJ.
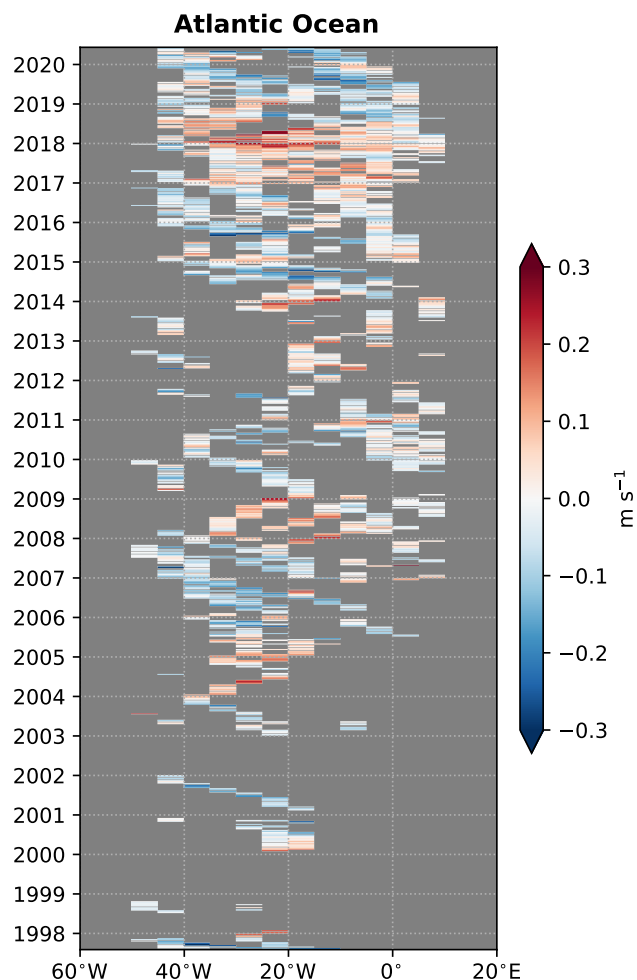
FIG. 1. Hovmöller diagram of zonal velocity at 1000 m depth along the equator in the Atlantic Ocean, from the YoMaHa'07 dataset (Lebedev et al. 2007). The shown zonal velocity values are averages between 1°S and 1°N, and over 5° longitude bins. Positive values mean eastward velocity, negative westward velocity.

We used all available Argo float profiles from the equatorial Atlantic, from between 2001 and June 2020 (Argo 2020). From these, we used the temperature, salinity and pressure data to calculate the in-situ density using a Python implementation of the Gibbs seawater library (*gsw 3.3.1*). If, from the variable in question, the "_ADJUSTED" version was present (meaning changes have been made to the raw data as part of quality control), we used it, otherwise we used the original, unchanged version. All values were checked in terms of their quality flags; only values flagged as *good data*, *probably good data*, *value changed* or *estimated value* were used (cf. Argo Data Management Team 2019, p.69).

Shown in Figure 2 is the second meridional derivative of the in-situ density, $\partial^2\rho/\partial y^2$, estimated from the equatorial Atlantic Argo float profiles between 1°S and 1°N wherever
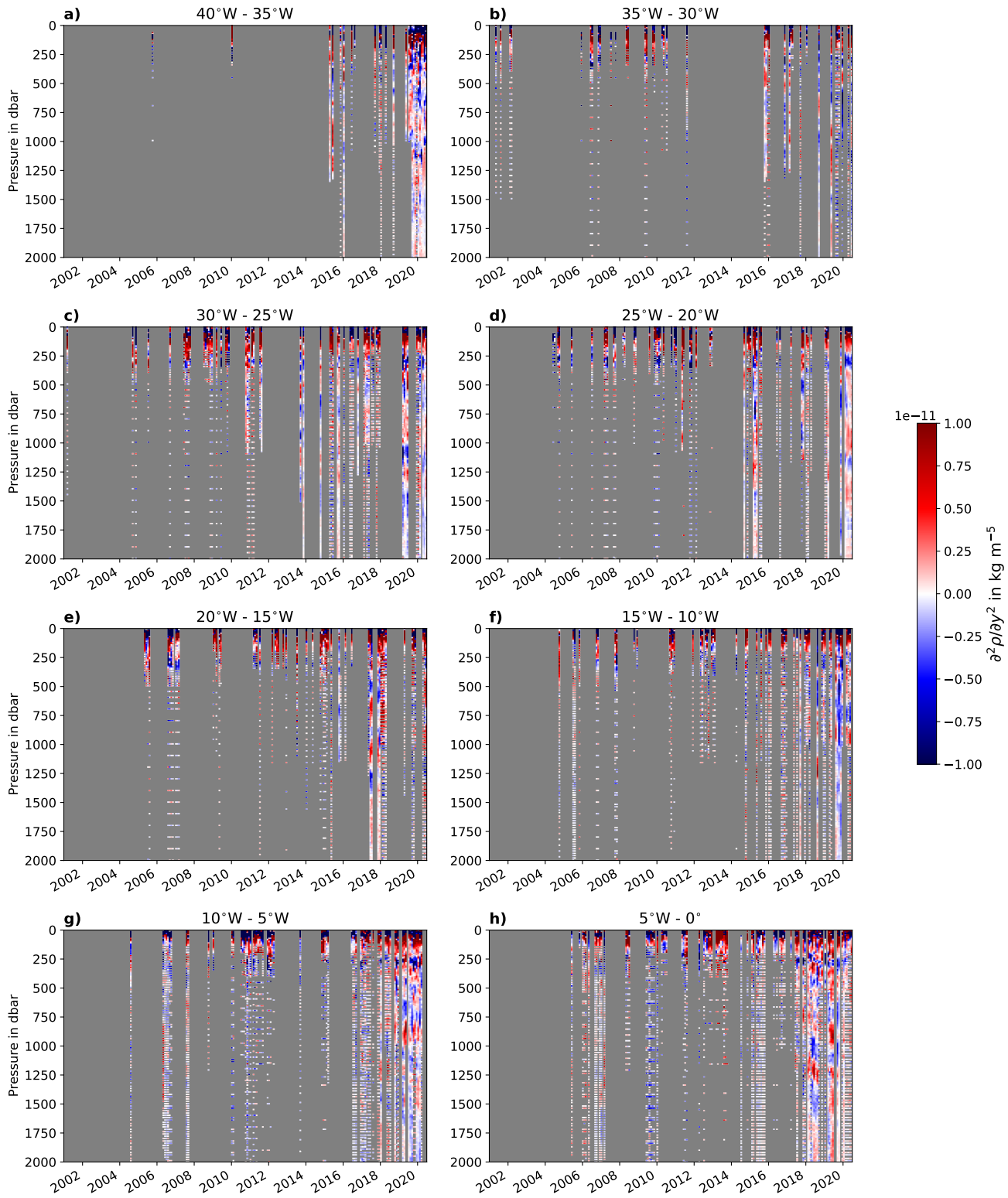
FIG. 2. Second meridional derivative of in-situ density, $\partial^2 \rho / \partial y^2$, from hydrographic Argo float data. The density ρ has been calculated from instantaneous Argo float profiles, then binned into 1 month $\times$ 5° longitude $\times$ 1° latitude bins (centered on the equator). $\partial^2 \rho / \partial y^2$ has then been calculated wherever three density values (one on the equator, one north and one south of the equator) were available for an individual month and longitude bin.
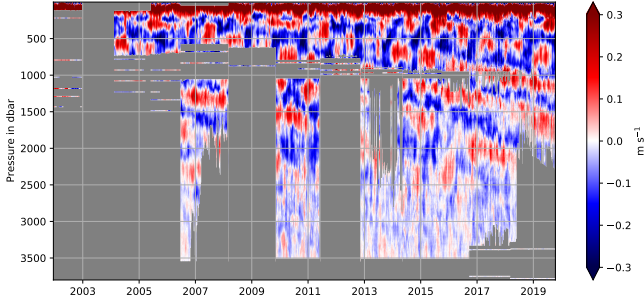
FIG. 3. Equatorial zonal velocity at 23°W measured by moored current meters (updated from e.g. Greatbatch et al. 2018). Positive values indicate eastward velocity, negative westward velocity.

FIG. 4. Spatial decorrelation scales of time mean zonal velocity at 1000 m depth in the tropical Atlantic between 7°S and 7°N. The color shading shows the autocorrelation (details see text), the black contour at a value of 0.37 indicates the e-folding scale. (This figure is a reproduction of Figure S3 in Bastin et al. 2020.)

possible, otherwise between 2°S and 2°N (for details on the relation between the EDJ and $\partial^2 \rho / \partial y^2$ please see the methods section). Indeed, EDJ-like structures are visible at all longitudes shown in Figure 2, as can be seen from a cursory comparison with Figure 3.

3) VALIDATION DATASET

The Atlantic EDJ characteristics have been estimated multiple times from the extensive deep velocity dataset from moored current meters at 23°W (Bunge et al. 2008; Brandt et al. 2011; Claus et al. 2016; Greatbatch et al. 2018). We want to use this dataset as an independent measurement of the EDJ to validate the parameters that we estimate from the Argo float data. Rather than just comparing our estimates to those from other studies, we use an updated version (extending to October 2019) here to get more robust estimates of the parameters. A detailed description of the dataset and measurement methods can be found in Tuchen et al. (2018). The zonal velocity measured by the moored instruments at 23°W is shown in Figure 3 (updated from e.g. Greatbatch et al. 2018).

b. Analysis methods

1) DETECTION OF PERIODIC SIGNALS – LOMB-SCARGLE PE-RIODOGRAMS

To detect the periodic signal of the EDJ, both in time and space, we used the Lomb-Scargle periodogram (cf. Lomb 1976; Scargle 1982). This is a useful method of detecting periodicity in cases where Fourier transformation cannot be applied because of uneven sampling or missing data. Calculating the Lomb-Scargle periodogram is equivalent to least-squares fitting of sine waves to the data for a given set of frequencies (Scargle 1982). The periodogram is given by the explained variance of the least-squares sine fit for each frequency. By normalizing with the number of observations N, an estimate of the power spectrum P_{pow}
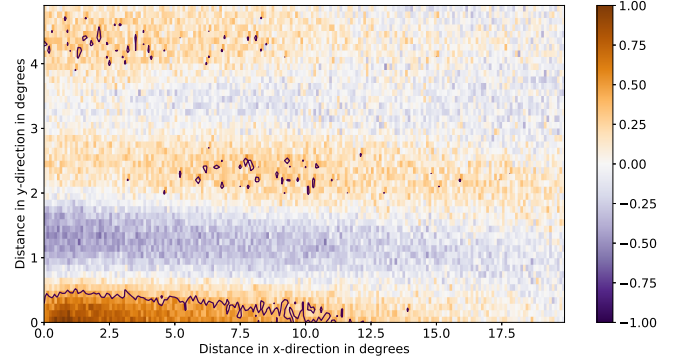
can be obtained (as well as the amplitude spectrum which is then $P_{amp} = \sqrt{P_{pow}}$):

$$P_{pow}(f) = \frac{\sum\limits_{j=1}^{N} \left[X(t_j) \right]^2 - \sum\limits_{j=1}^{N} \left[X(t_j) - X_f(t_j) \right]^2}{N^2} \quad (1)$$

where $X(t_j)$ are the data points, and $X_f(t_j)$ is the value of the fitted sine wave at time t_j for frequency f. For evenly spaced data, the result will be equal to the power spectrum obtained by Fourier transformation, if the frequencies for the sine wave fits are chosen accordingly.

2) SPATIAL SMOOTHING

Because the data are relatively sparse even at 1000 m depth, some spatial smoothing of the Argo velocity data is done with a 2D Gaussian filter, following Bastin et al. (2020). To make sure that we do not average over scales that are larger than the scales on which the zonal velocity field can be assumed to be coherent, we choose the filter scales based on the decorrelation scales of the zonal velocity at 1000 m depth (shown in Figure 4, for details see Bastin et al. 2020).

3) UNCERTAINTY QUANTIFICATION

We used bootstrapping to obtain uncertainties for our parameter estimations. Bootstrapping allows us to determine confidence intervals for estimated parameters without prior knowledge of the shape of the underlying distribution (e.g. Efron 1979). For each parameter of the Atlantic EDJ that we estimate, we take 10,000 resample sets with replacement of the original unsmoothed dataset used to estimate the parameter, then calculate the parameter again from each of these resample sets, such that we get a distribution for

the parameter in question. The sample size of each of the 10,000 resample sets is the same as the sample size available from the original data. We preserve the time and space information of each data point when resampling, such that the data are not shuffled in time or space, but some data points are omitted or included multiple times. From the resulting distribution, we then give a 95% confidence interval by taking the 2.5% and 97.5% quantiles. This method can give a measure of the error in our parameter estimation connected to sampling uncertainties. Additional errors, especially of a systematic kind, originating e.g. from measurement errors, are not considered.

4) ESTIMATION OF VERTICAL EDJ SCALE FROM HYDRO-GRAPHIC DATA

We make use of the fact that the EDJ are, approximately, in geostrophic balance (e.g. Eriksen 1982) to extract information about their vertical scale from the hydrographic data provided by the Argo floats. At the equator, the geostrophic balance for the zonal flow takes the form

$$\beta u = -\frac{1}{\rho_0} \frac{\partial^2 p}{\partial y^2} \quad \text{for} \ y \to 0 \quad (2)$$

where $\beta = df/dy$ is the meridional derivative of the Coriolis parameter, u is the zonal velocity, ρ_0 is a constant reference density, p is the pressure, and y indicates distance from the equator measured positive northward (e.g. Gill 1982, p. 461).

We can relate the geostrophic velocity to the density field by using the hydrostatic balance

$$-\rho g = \frac{\partial p}{\partial z} \quad (3)$$

where ρ is the (variable) in-situ density, g is the gravitational acceleration, p the pressure and z the water depth measured positive upward. Combining equations 2 and 3 leads to the equatorial form of the thermal wind equation:

$$\beta \frac{\partial u}{\partial z} = \frac{g}{\rho_0} \frac{\partial^2 \rho}{\partial y^2} \quad (4)$$

or, if using the pressure as vertical coordinate (with $\partial z/\partial p$ from Eq. 3):

$$\frac{\partial u}{\partial p} = -\frac{1}{\beta \rho_0 \rho} \frac{\partial^2 \rho}{\partial y^2} \quad (5)$$

It is thus possible to reconstruct the equatorial geostrophic velocity field from the density field, provided that we know the velocity at some reference pressure p_{ref}, as

$$u(p) = -\frac{1}{\beta \rho_0} \int_{p_{ref}}^{p} \left(\frac{1}{\rho} \frac{\partial^2 \rho}{\partial y^2} \right) dp' + u(p_{ref}) \quad (6)$$
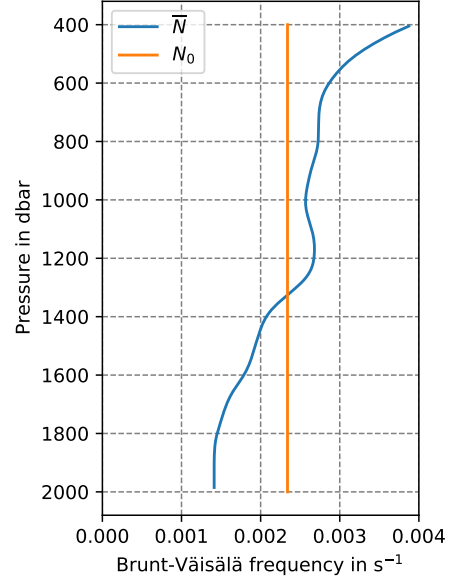
FIG. 5. Stratification profiles used for vertical WKBJ stretching and scaling. The data are provided as a supplementary dataset (see data availability statement).

As reference velocity, we use the YoMaHa'07 data at a pressure of 1000 dbar.

5) STRETCHING OF VERTICAL COORDINATE

The stratification of the water column affects the vertical wavelength and the amplitude of waves propagating through it. To correct for this effect when analyzing the vertical structure of the Atlantic EDJ, we apply scaling and stretching corresponding to the WKBJ approximation (Gill 1982). We stretch the vertical pressure coordinate p as described in Leaman and Sanford (1975):

$$dp^* = \frac{\overline{N}(p)}{N_0} dp \quad (7)$$

where p^* denotes stretched pressure. The zonal velocity u has been scaled, again following Leaman and Sanford (1975), as

$$u^*(p) = u(p) \cdot \left(\frac{N_0}{\overline{N}(p)} \right)^{1/2} \quad (8)$$

$\overline{N}(p)$ denotes a typical profile of the Brunt-Väisälä frequency N, N_0 the vertical average of $\overline{N}(p)$. Following Youngs and Johnson (2015), we calculated $\overline{N}(p)$ as the horizontally and temporally averaged N from hydrographic Argo data from the region of interest, in our case the equatorial Atlantic between 2.5°S and 2.5°N and between 400 and 2000 m depth. Additionally, $\overline{N}(p)$ has been smoothed vertically using a Hanning filter with a

half-width of 200 dbar as in Youngs and Johnson (2015). The resulting $\overline{N}$ and N_0 can be seen in Figure 5, and are provided as a supplementary dataset (see data availability statement).

3. Results

a. Frequency at 1000 m depth

In Figure 1, a Hovmöller diagram of the equatorial zonal velocity at 1000 m depth in the Atlantic from the YoM-aHa'07 deep velocity dataset is shown. The velocity values are averaged between 1°S and 1°N, as well as over 5° longitude bins. The EDJ are visible as a clear inter-annual variation of the zonal velocity, which also appears to be the strongest signal in the data. This is corroborated by the power spectrum of equatorial zonal velocity at 1000 m depth, again averaged between 1°S and 1°N and over 5° longitude bins, which is shown in Figure 6a. Since the EDJs' phase is not constant throughout the basin but depends on the longitude, separate Lomb-Scargle periodograms for each 5° longitude bin have been computed and are shown in Figure 6a as colored lines. The average of all these spectra is shown as the dashed black line. The Lomb-Scargle periodograms have been calculated at frequencies with a resolution of $2 \cdot 10^{-4}$ years^{-1}. Indeed, the interannual peak at a period of 4.6 years is the most energetic signal in the zonal velocity at 1000 m depth in the equatorial Atlantic. Additionally, a somewhat weaker annual signal can be seen, as well as an even weaker semi-annual peak. This fits well to previous estimates from the 23°W mooring (Claus et al. 2016; Greatbatch et al. 2018), although in these studies the annual peak appears stronger than the interannual peak, because variability at all depths instead of only 1000 m has been included in the analysis. The annual and semiannual cycles in the Atlantic Ocean are dominantly associated with the fourth and second baroclinic mode, respectively, as shown by Brandt et al. (2016), so the amplitude will show a strong dependence on depth.

In the averaged periodogram shown in Figure 6a, the interannual peak is located at a frequency of 0.2174 years^{-1}, corresponding to a period of 4.60 years. The location of this peak is consistent over all the periodograms, meaning that the time scale of the Atlantic EDJ is independent of longitude, as we would expect from their theoretical explanation as a resonant basin mode (Greatbatch et al. 2012).

The 95% confidence interval is found to be between 0.2156 and 0.2192 years^{-1}, shown in Figure 6b, corresponding to periods of 4.64 years and 4.56 years. Note that the periods are calculated as the reciprocal of the frequency values and not from an independent estimation via bootstrapping. All parameter estimates described in this paper are summarized in Table 1.

In Figure 6c, a comparison to the EDJ frequency estimated from the 23°W mooring dataset is shown, as well as a comparison to the estimate by Youngs and Johnson

(2015). The estimate from the YoMaHa'07 velocity data at 1000 m depth lies well within the much larger range of estimates from the mooring data, and just within the confidence interval from Youngs and Johnson (2015) which is shifted towards lower frequencies.

b. Amplitude at 1000 m depth

To estimate the shape that the EDJ assume in the basin, we calculate their amplitude at 1000 m depth on a $0.2° \times 0.2°$ grid in the equatorial Atlantic basin using the smoothing procedure described in the methods section and Bastin et al. (2020). The resulting amplitude field can be seen in Figure 7a. It is worth noting that the amplitude in this study always refers to the harmonic amplitude of the EDJ, because we calculate it by harmonic fitting of the data, using our EDJ frequency estimate of 0.2174 years^{-1}. This is likely the reason for the discrepancy between our amplitude estimates and the somewhat larger values that many instantaneous measurements suggest. In general, the EDJ are strongest directly on the equator, and their amplitude decreases quickly with increasing distance from the equator. This is in accordance with their appearance as a basin mode of a high baroclinic mode – the constituting parts, equatorial Kelvin and Rossby waves, are both characterised by a zonal velocity maximum on the equator and decreasing zonal velocity away from the equator. In the centre of the basin (and a bit to the west), the EDJ are narrowest and strongest; towards the east and west they become broader and eventually seem to split into two off-equatorial maxima. This is reminiscent of the zonal velocity amplitude fields of modelled basin modes shown in Greatbatch et al. (2012) and Claus et al. (2014), where β-dispersion leads to focussing of long off-equatorial Rossby waves in the centre of the basin (Schopf et al. 1981) and thus a narrowing of the basin mode amplitude field. Claus et al. (2014) suggest that this focussing effect is suppressed by the barotropic mean flow around the equator. However, from the EDJ amplitude field estimated here it appears that the equator is not entirely shielded by the barotropic mean flow, but that some focussing of energy in the centre of the basin does take place.

The amplitude of the EDJ clearly depends on longitude. To estimate the uncertainty of the EDJ amplitude on the equator, we therefore again separate the YoMaHa'07 zonal velocity data into 5° wide bins, and estimate the amplitude for each of these individually by fitting a sine wave with the frequency that we estimated in the previous section (0.2174 years^{-1}). The amplitude of the EDJ is quite sensitive to the distance to the equator, as is visible in Figure 7a, such that we restricted the bins to 0.5°S to 0.5°N for this calculation. The resulting EDJ amplitude values can be seen in Figure 7b and Table 1, together with the 95% confidence interval obtained by bootstrapping.

TABLE 1. Overview of the Atlantic EDJ characteristics. The bold value in the center is always the value estimated from the original data. Values in parentheses above and below are the 0.025 and 0.975 quantiles of the parameter distribution obtained by bootstrapping. Frequency and zonal wavelength have been estimated for the entire basin instead of for the different 5° longitude bins. The period is not a parameter that has been separately estimated, but is the reciprocal of the frequency and is included here for easier readability. The vertical wavelength is given in stretched decibars. For a comparison to other estimates, the exact profile of N that we used for vertical stretching is necessary: this can be found in the supporting dataset (see data availability statement).

| | YoMaHa'07 (1000 m depth) | | | | | | | |
	40°W - 35°W	35°W - 30°W	30°W - 25°W	25°W - 20°W	20°W - 15°W	15°W - 10°W	10°W - 5°W	5°W - 0°E
Frequency (years^{-1})				(0.2156) **0.2174** (0.2192)				
Period (years)				(4.64) **4.60** (4.56)				
Amplitude (cm s^{-1})	(6.0) **7.6** (9.3)	(7.6) **9.1** (10.7)	(8.4) **10.3** (12.2)	(9.1) **10.7** (12.4)	(8.5) **10.7** (12.9)	(8.3) **9.9** (11.6)	(3.3) **4.7** (6.3)	(2.4) **3.7** (5.1)
Phase (January 1, 2000)	(0.109) **0.285** (0.454)	(0.190) **0.374** (0.608)	(0.433) **0.567** (0.722)	(0.555) **0.727** (0.894)	(0.705) **0.833** (0.960)	(0.824) **0.984** (1.152)	(1.319) **1.583** (1.920)	(1.494) **1.797** (2.046)
Zonal wavelength (°)				(126.3) **146.7** (177.4)				
	hydrographic Argo data (400 m – 2000 m depth)							
Vertical wavelength (sdbar)	(629) **599** (435)	(490) **467** (450)	(508) **493** (478)	(498) **483** (472)	(581) **532** (463)	(495) **488** (459)	(505) **493** (483)	(610) **474** (452)

In Figure 7c, the EDJ amplitude estimated from the 23°W mooring dataset is shown for comparison. Around 1000 m depth, the data coverage from the mooring is sparse (cf. Figure 3), such that the amplitude estimation is relatively noisy. However, it agrees well with the estimate from the YoMaHa'07 data. The strong modulation of the EDJ amplitude with depth that is visible in the mooring data may be explained by a beat pattern created by the vertical structures of the normal modes that the EDJ are dominantly composed of (Claus et al. 2016).

c. Phase and zonal wavelength at 1000 m depth

From the equatorial zonal velocity data at 1000 m depth, we calculate the phase of the EDJ harmonic in the equatorial Atlantic. We do this by least-squares fitting of a cosine function of the form $A \cdot \cos(\omega \cdot t + \varphi)$, where the amplitude A and the phase φ are free parameters to be fitted, t is the time (chosen such that $t = 0$ corresponds to January 1, 2000), and the angular frequency $\omega = 2 \cdot \pi \cdot f_{EDJ}$ is fixed to the EDJ frequency with $f_{EDJ} = 0.2174$ years^{-1} (see section on frequency).

In Figure 8a, the EDJ phase estimated from the smoothed zonal velocity field at 1000 m depth is shown. The phase field is characterised by zonal bands with mostly westward phase propagation and sudden phase shifts by π between them, which shows the signature of a first meridional mode equatorial Rossby wave (for more details on this, see the next section). In Figure 8b, the EDJ phase on the equator is shown, together with the 95% confidence intervals from bootstrapping. All values appear as well in Table 1. For comparison, the EDJ phase values estimated from the 23°W mooring data are shown in Figure 8c, and they fit nicely to the estimate from the YoMaHa'07 data.

We can obtain the zonal propagation direction and wavelength by evaluating the change of EDJ phase with longitude. This is shown locally for every grid point in Figure 9a. Although the field is noisy, the EDJs' westward phase propagation on the equator is clearly visible. North and south of the equator, bands of eastward phase propagation appear where the equatorial Kelvin wave dominates the signal (for details see next section).
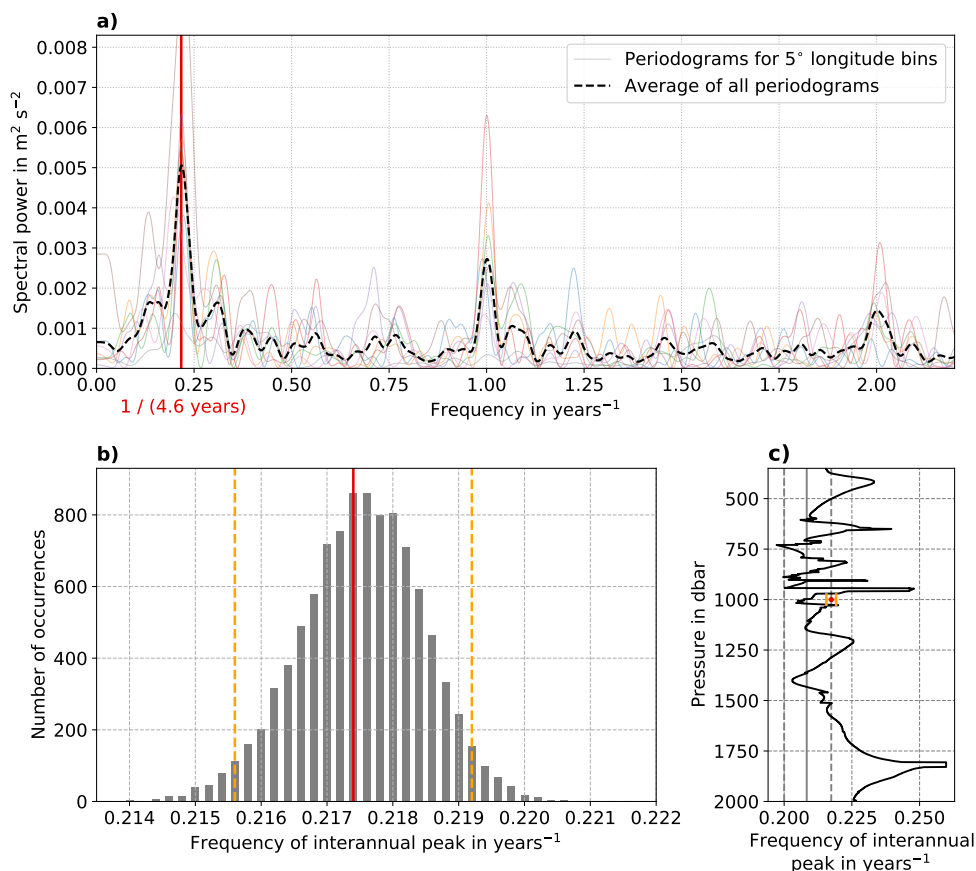
FIG. 6. Frequency of the Atlantic EDJ at 1000 m depth. Panel a: Lomb-Scargle periodograms of equatorial zonal velocity at 1000 m depth in the Atlantic Ocean, separated into 5°-wide bins (colored lines). The black dashed line is the average of all individual periodograms. Panel b: Distribution of interannual peak frequency of Atlantic Ocean equatorial zonal velocity at 1000 m depth as determined by bootstrapping. The red line indicates the value calculated from the original dataset, the orange dashed lines mark the 2.5% and 97.5% quantiles of the distribution. (All parameter estimations and confidence intervals are summarized in Table 1.) Panel c: Comparison with mooring data from 23°W, and estimate from Youngs and Johnson (2015). The interannual peak frequency from the mooring data is shown in black, with the corresponding value and confidence interval from the YoMaHa'07 dataset in red and orange for comparison. The estimate by Youngs and Johnson (2015) is indicated by the grey solid line, their 95% confidence interval by the dashed grey lines.

We calculate the Atlantic EDJs' zonal wavelength by linear regression of the phase-longitude relationship shown in Figure 8b; the result can be seen in Figure 9b. On the equator, the zonal wavelength of the Atlantic EDJ is 146.7° (indicated by the red marker, 95% confidence interval between 126.3° and 177.4°), which is between the wavelength of an equatorial Kelvin wave and that of a first meridional mode Rossby wave with the corresponding frequency and vertical mode of the EDJ (see Figure 9b). As visible in Figure 9b, the zonal wavelength of the variability at the EDJ frequency is very much dependent on latitude, because of the differences in the meridional structure of the Kelvin and Rossby waves that together constitute the EDJ. North of the equator, the zonal wavelength of the EDJ first increases, getting closer to the Kelvin wavelength, and then decreases to approximately the wavelength of the Rossby wave. South of the equator, the pattern is not as clear. Our

estimates are consistent with the model results from Claus et al. (2016; see their Figure 7a), and also with Youngs and Johnson (2015) who only estimated the zonal wavelength of the Rossby wave component of the Atlantic EDJ based on vertical strain at 1.5°S/N.

d. Meridional structure at 1000 m depth and contributions of Kelvin and Rossby wave signals

It has been noted by a number of earlier studies that the EDJ show characteristics of an equatorial basin mode (e.g. d'Orgeville et al. 2007; Greatbatch et al. 2012; Ascani et al. 2015; Matthießen et al. 2015, 2017). Equatorial basin modes consist of the resonant combination of an equatorial Kelvin wave and its reflection as a sum of odd meridional mode long equatorial Rossby waves (Cane and Moore 1981). To find out how large the contributions of the different equatorial waves are to the total EDJ amplitude,
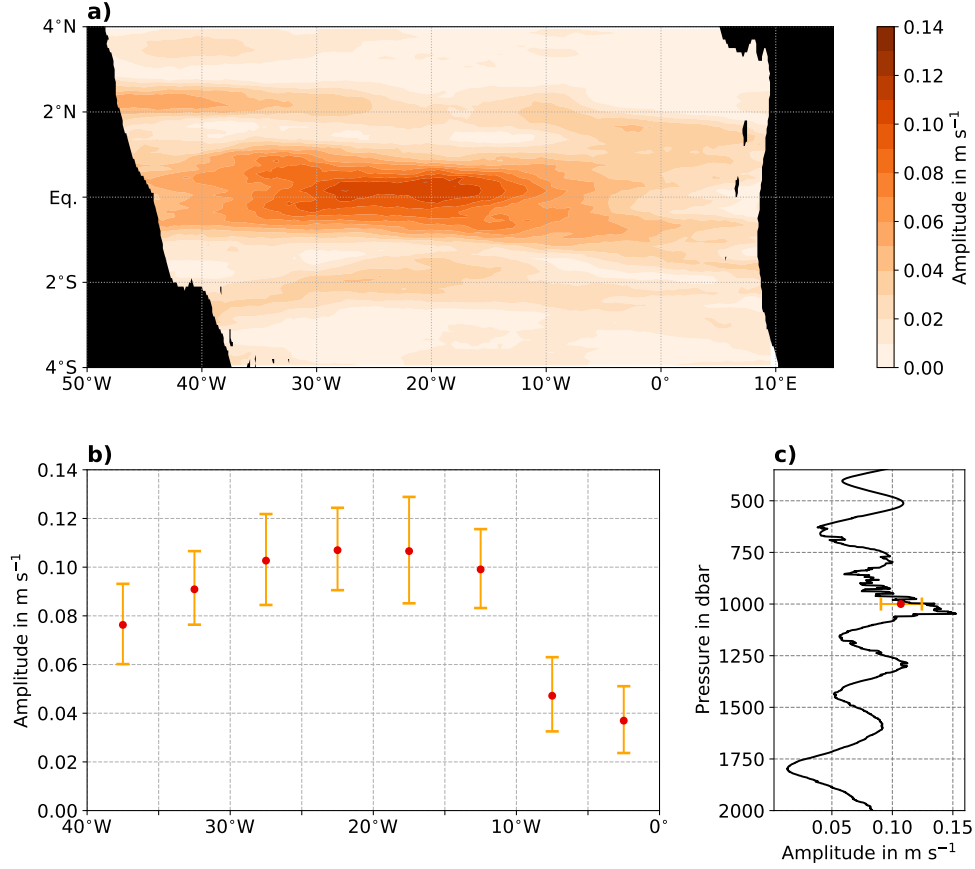
Fig. 7. Harmonic amplitude of the Atlantic equatorial deep jets at 1000 m depth. Panel a shows the amplitude of a harmonic fit at the estimated EDJ frequency of 0.2174 years^{-1} to the smoothed zonal velocity field from YoMaHa'07 (for details on the smoothing see the methods section). Panel b shows EDJ amplitude values along the equator in red, estimated from the original, unsmoothed data between 0.5°S and 0.5°N and from 5° longitude bins. The orange error bars mark the 2.5% and 97.5% quantiles of the distribution obtained by bootstrapping (these values can also be found in Table 1). Panel c shows a comparison with mooring data from 23°W. The harmonic EDJ amplitude from the mooring data is shown in black, with the corresponding value and confidence interval from the YoMaHa'07 dataset (from 25°W-20°W) in red and orange for comparison.

we separate the zonal velocity data from 1000 m depth into a Kelvin wave component and a Rossby wave component.

The meridional structure of the zonal velocity signature is given by (cf. Gill 1982, Chapter 11)

$$u_K(y) = u_{0\_K} \cdot \exp(-\frac{\beta y^2}{2c}) \qquad (9)$$

for an equatorial Kelvin wave, and by

$$
\begin{aligned}
u_{Rn}(y) = \ & u_{0\_Rn} \cdot \exp(-\frac{\beta y^2}{2c}) \cdot \\
& \left[\left(c - \frac{c}{2n+1} \right) \cdot 2^{-(n+1)/2} \cdot H_{n+1}\left(\sqrt{\frac{\beta}{c}} y \right) - \right. \\
& \left. \left(c + \frac{c}{2n+1} \right) \cdot n \cdot 2^{-(n-1)/2} \cdot H_{n-1}\left(\sqrt{\frac{\beta}{c}} y \right) \right]
\end{aligned}
\qquad (10)
$$

for long equatorial Rossby waves with meridional mode number n. u_{0_K} and u_{0_Rn} denote constant amplitude

values, y is the distance from the equator measured positive northward, $\beta = 2.3 \cdot 10^{-11}$ m^{-1} s^{-1} (Gill 1982, Chapter 11) is the change of the Coriolis parameter with latitude, and H_n denotes the nth Hermite polynomial. The dominant vertical mode and corresponding gravity wave speed $c = 0.16$ m s^{-1} of the EDJ has been estimated by a normal mode decomposition of the moored zonal velocity measurements from 23°W, using a mean stratification obtained from equatorial cruise data, as described in detail in Claus et al. (2016).

The meridional structure of the Atlantic EDJ amplitude field shown in Figure 7 is strongly reminiscent of the zonal velocity amplitude structure of a $n = 1$ Rossby wave, with the equatorial maximum, followed by a minimum and a second maximum with increasing distance from the equator. However, the distance from the equator of the off-equatorial amplitude minima of the EDJ in Figure 7 is larger by a factor of 1.5 than theoretically expected for the particular choice of c from Eq. 10, even in the center
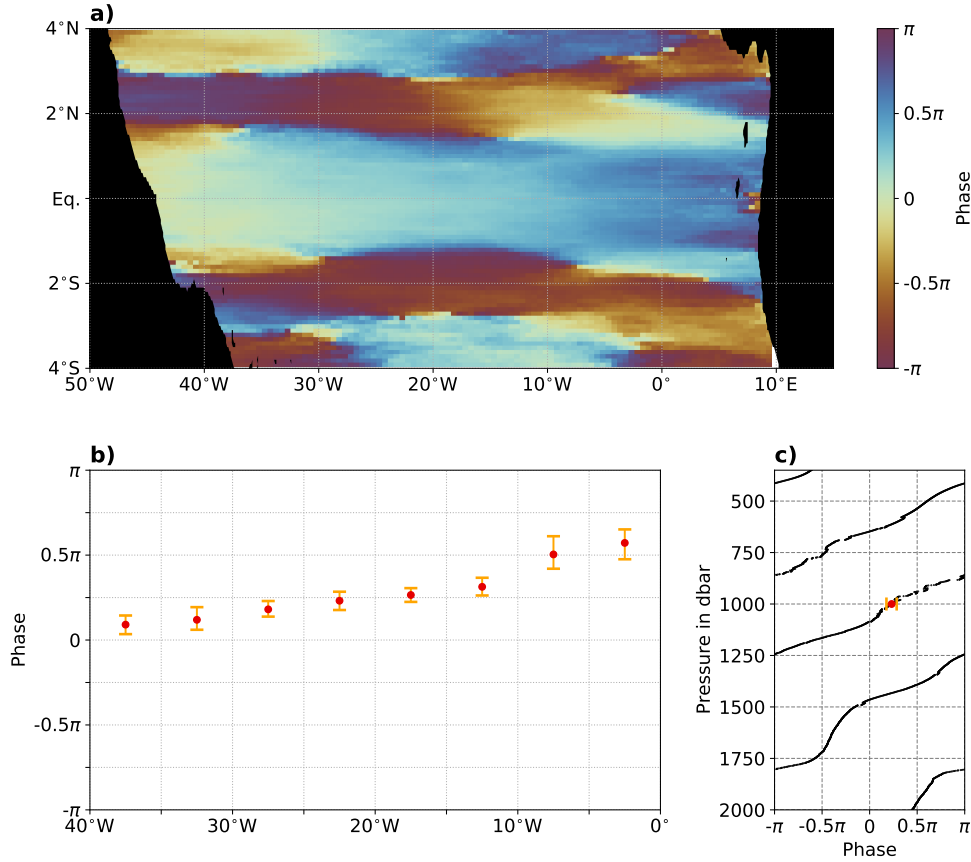
FIG. 8. Phase of the Atlantic EDJ at 1000 m depth. The phase values φ are calculated by least-square-fitting of a cosine function of the form $A \cdot \cos(\omega t + \varphi)$ to the YoMaHa'07 zonal velocity data. The time axis t for the fit has been chosen such that the origin ($t = 0$) is January 1, 2000. The angular frequency $\omega = 2 \cdot \pi \cdot 0.2174 \, \text{years}^{-1}$ has been fixed to the estimated EDJ frequency value. Panel a: Phase estimated from the smoothed zonal velocity field. Panel b: Phase values along the equator calculated from the original, unsmoothed data (from between 1°S and 1°N, and separated into 5° longitude bins) in red. The orange error bars mark the 2.5% and 97.5% quantiles obtained by bootstrapping (for all these values see also Table 1). Panel c: Comparison to mooring data from 23°W. The EDJ phase from the mooring data is shown in black, with the corresponding value and confidence interval from the YoMaHa'07 dataset (from 25°W-20°W) in red and orange for comparison.

of the basin (around 20°W) where the EDJ are narrowest. This fits very well to earlier studies that investigated the meridional width of the EDJ (e.g. Johnson and Zhang 2003; Greatbatch et al. 2012; Claus et al. 2014; Youngs and Johnson 2015). We therefore stretched the theoretical profiles given by Eqs. 9 and 10 meridionally by a factor of 1.5 before fitting them to the estimated EDJ amplitude profile.

At the latitudes where the zonal velocity signature of the Rossby wave has zero amplitude (at 1.35°S/N in the stretched version of Eq. 10), the Kelvin wave signal should dominate the EDJs' zonal velocity field. This is partly visible in Figure 9a, where the propagation direction of the EDJ harmonic is westward on and close to the equator (suggesting that here, the Rossby wave dominates the EDJ signal), but turns eastward at around 1.35°S/N. However, this is only clear between 20°W and 5°W, and not so obvi-

ous in the western half of the basin, where the field looks rather noisy.

To separate the contributions of the Kelvin wave and the $n = 1$ Rossby wave to the EDJ signal, we determined the amplitude and phase values in the center of the basin (averaged between 21°W and 19°W), and at 1.35°N where the Rossby wave amplitude vanishes (shown in Figure 10a,b). With these parameters, we then reconstructed the time-varying zonal velocity field of the Kelvin wave, and subtracted it from the original zonal velocity data at 1000 m depth. Fitting of the theoretical amplitude and phase profiles of a first meridional mode Rossby wave to the resulting meridional amplitude and phase profiles then yields the results shown in blue in Figure 10c,d. The zonal velocity amplitude on the equator of the Kelvin wave component thus amounts to 3.18 cm s^{-1}, whereas that of the first meridional mode Rossby wave component is 11.22 cm s^{-1}. Polewards of about 2.5°S/N, the influence of higher mode Rossby waves
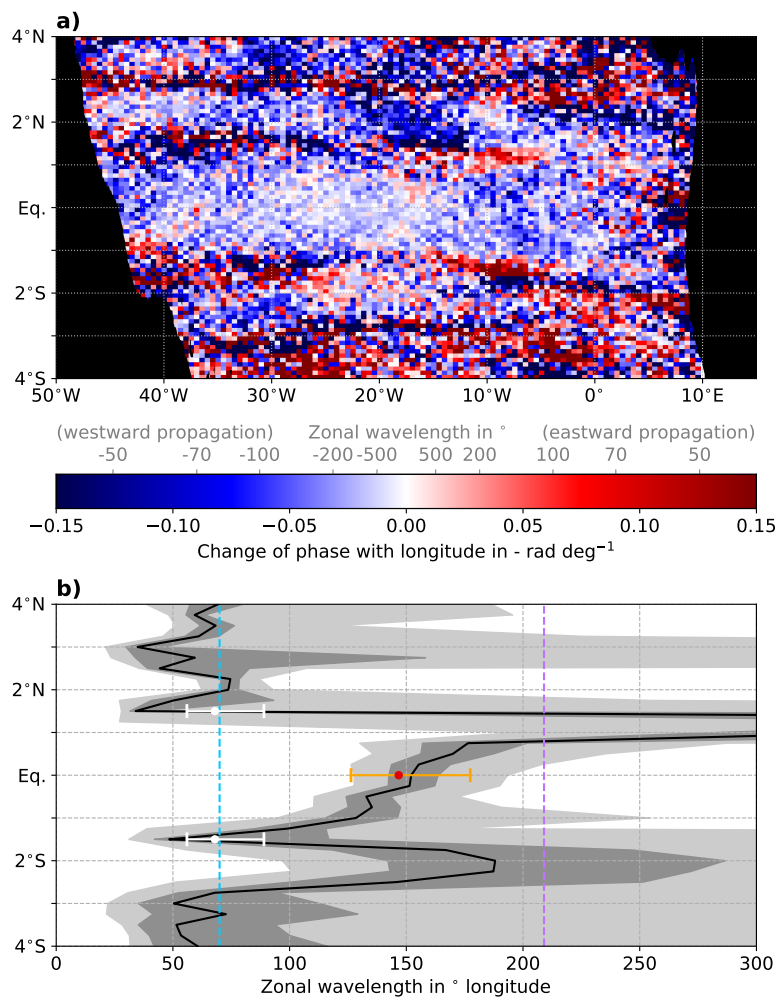
FIG. 9. Zonal wavelength of the Atlantic EDJ at 1000 m depth. Panel a shows the change of EDJ phase (as shown in Figure 8a) with longitude, and the associated zonal wavelength. Blue shading means westward propagation of the EDJ harmonic, red colors indicate eastward propagation. Panel b shows the absolute value of the zonal wavelength estimated by linear regression of the EDJ phase between 40°W and 0°E. Indicated in red is the estimate from the original data between 1°S and 1°N, with the 95% confidence interval in orange. To examine the change with latitude, the zonal EDJ wavelength is shown for different latitudes in black, now with only 1° wide latitude bins to show more detail. The dark grey shading indicates the 50%, the light grey shading the 95% confidence interval. In white, the estimate and 95% confidence interval from Youngs and Johnson (2015) is shown. The theoretical Kelvin wavelength is shown by the dashed purple line, the meridional mode 1 Rossby wavelength by the dashed blue line.

is visible in the repeated amplitude minimum and π phase shift that cannot be accounted for by the fit. Shown in Figure 10 are only results using data from the center of the basin, where the EDJ signal is strongest – repeating the analysis with data further east yielded less significant results because of larger contributions from higher mode Rossby waves (not shown).

e. Vertical structure on the equator

We used the hydrographic data that are measured by the Argo floats during descent/ascent to reconstruct the geostrophic zonal velocity at depth, using the YoMaHa'07 data at 1000 m depth as reference (see methods section).

However, this is possible only directly on the equator, as well as prone to large error propagation (cf. Eq. 4), such that we only use this to estimate the vertical structure of the Atlantic EDJ which cannot be inferred from the YoM-aHa'07 data.

In Figure 11, a comparison of the reconstructed geostrophic velocity from hydrographic Argo data between 20 and 25°W with the velocity measured by moored current meters at 23°W is shown. The reconstructed zonal velocity (Panel b) was originally dominated by strong, but apparently random, linear vertical trends. We suspect that these are spurious and due to the vertical integration of systematic errors in the original Argo float measurements,
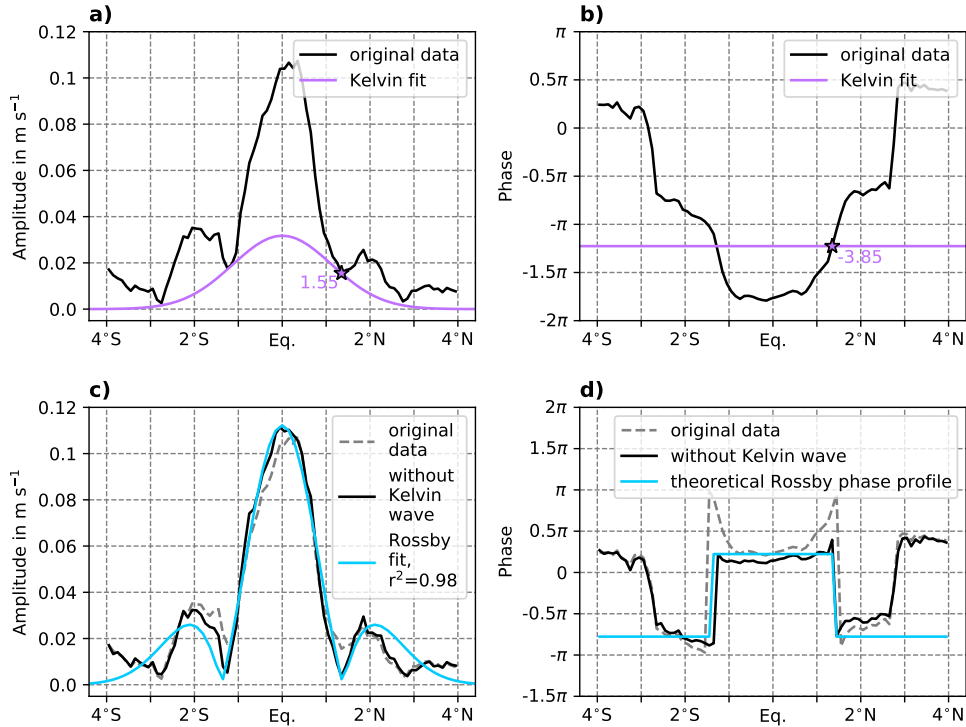
FIG. 10. Amplitude and phase of the Kelvin and first meridional mode Rossby wave components of the Atlantic EDJ at 1000 m depth in the center of the basin. Panels a and b show the meridional profiles of EDJ amplitude and phase averaged between 21°W and 19°W in black. The purple stars and corresponding numbers indicate the values used to reconstruct the Kelvin wave profiles (shown as purple lines). In Panels c and d, the amplitude and phase profiles after removing the Kelvin wave signal are shown in black (for comparison the original data in grey). The fit of a first meridional mode Rossby wave to the remaining data is shown in blue. Note that the theoretical Kelvin and Rossby wave profiles have been stretched meridionally by a factor of 1.5 (details see text).

possibly caused by drift of the salinity sensors. These trends have been removed before further analysis; shown in Figure 11 is the vertically detrended zonal velocity. Although there is some noise visible in the reconstructed geostrophic zonal velocity from Argo data, it generally compares well with the zonal velocity measurements from the 23°W mooring, and seems to capture the EDJ quite well.

To estimate the vertical wavelength of the Atlantic EDJ, we again make use of the Lomb-Scargle periodogram to calculate vertical wavenumber spectra of the zonal velocity. We choose wavenumbers with a resolution of $1 \cdot 10^{-5}$ sdbar^{-1}, which corresponds to a wavelength resolution of approximately 2.5 sdbar around 500 sdbar. In Figure 12, the resulting spectra are shown from the reconstructed zonal velocity from Argo from between 20 and 25°W (Panel a) and, for comparison, from the 23°W moored velocity measurements (Panel b). Note that the data have been stretched and scaled before spectral analysis to remove the influence of variable stratification with depth (for details see the methods section), as well as temporally filtered to get rid of noise on time scales different from that of the EDJ. In Panel c, the peak vertical wave-

length is shown for all longitudes, together with a 95% confidence interval obtained by bootstrapping. The value and confidence interval from the mooring data is drawn in black, and it can be seen that although the difference between the estimated vertical EDJ wavelengths is only about 20 sdbar (with 483 sdbar from the Argo data between 25°W and 20°W, and 465 sdbar from the mooring data at 23°W), the confidence intervals do not overlap. This significant difference indicates deficiencies in our error estimation – it seems that, in this case, there is an additional source of error beside the sampling uncertainty that cannot be quantified by bootstrapping. The basin-wide estimate by Youngs and Johnson (2015) from shipboard CTD measurements, which is shown in grey, compares well with our estimates.

It has been noted before that the EDJ are slightly tilted towards the east, both in observations (Schmid et al. 2005) and model simulations (Claus et al. 2016). We used the phase information obtained through vertical harmonic fitting of the reconstructed geostrophic zonal velocity data averaged over six-month time bins to quantify this eastern deepening. In Figure 13a, the resulting phase is shown as a function of longitude and time. A tilt with longitude is visible. In Figure 13b, all phase anomalies are shown as
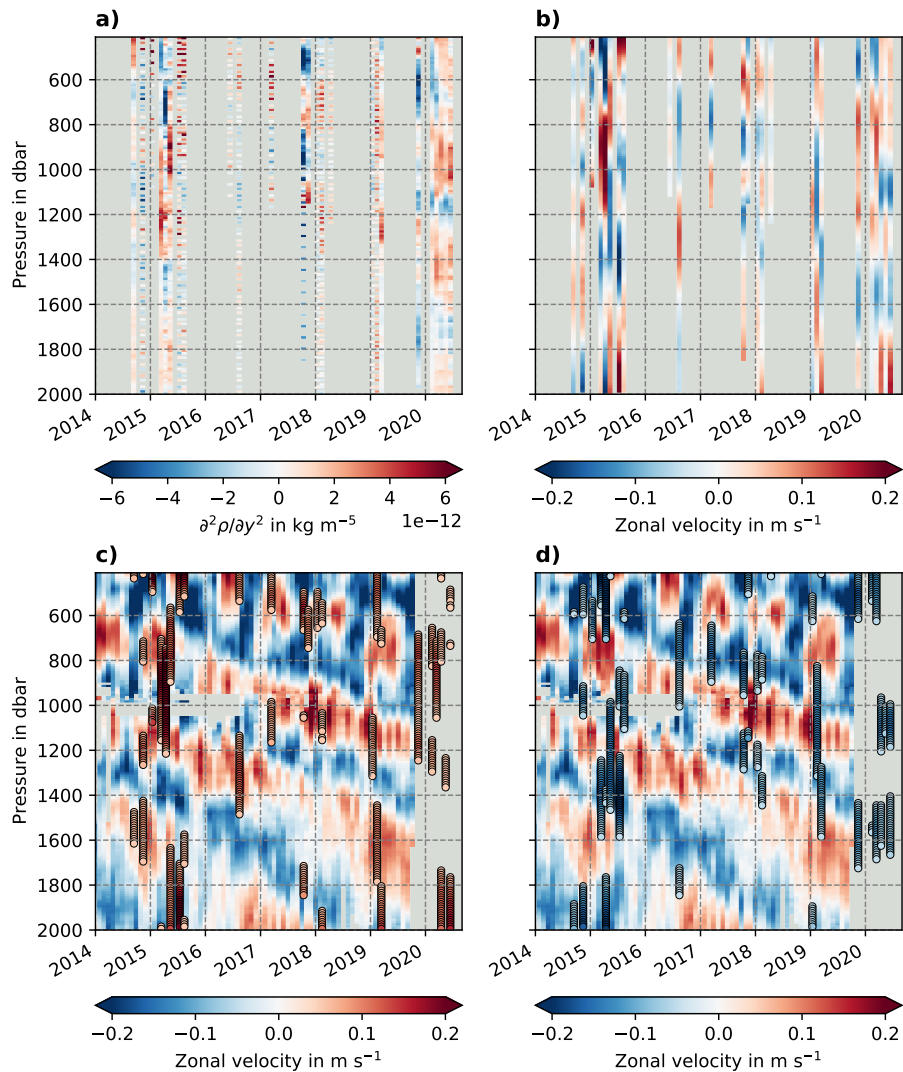
FIG. 11. Reconstructed equatorial geostrophic zonal velocity from hydrographic Argo float data between 25°W and 20°W. Panel a: Second meridional derivative of in-situ density, calculated from Argo float temperature and salinity measurements, averaged monthly and between 25°W and 20°W. Panel b: Geostrophic zonal velocity as calculated from the data shown in Panel a, referenced with Argo float displacement data from YoMaHa'07 at 1000 m depth, and detrended vertically (details see text). Panels c and d: Moored equatorial zonal velocity measurements at 23°W (color shading) for comparison. The reconstructed geostrophic zonal velocity that is also shown in Panel b is drawn here as colored circles, for better visibility separated into positive values (Panel c), and negative values (Panel d).

grey markers (calculated by, for every available six-month average separately, subtracting the mean over all longitudes). The median at every longitude is indicated by an orange asterisk. The deepening of the EDJ towards the east does not seem to be linear: The tilt of the EDJ is strongest in the western part of the basin, and the EDJ flatten out towards the east, consistent with the findings of Schmid et al. (2005) from the comparison of shipboard sections at different longitudes. A least-squares quadratic fit suggests a deepening of the EDJ between 40°W and 0°E of about 0.35 π or a sixth of their vertical wavelength, i.e. about 80 sdbar.

4. Discussion

a. A new characterization of the Atlantic EDJ

In this study, we have compiled a new, independent, more comprehensive and accurate description of the Atlantic equatorial deep jets (EDJ) than available so far. For this, we have analyzed Argo float displacement data at 1000 m depth (Lebedev et al. 2007) and Argo float hydrographic profiles (Argo 2020). At 1000 m depth, we provide estimates of the period, the amplitude, the phase, the zonal wavelength, and the meridional structure of the Atlantic EDJ. Our EDJ period estimate of 4.60 years (95%
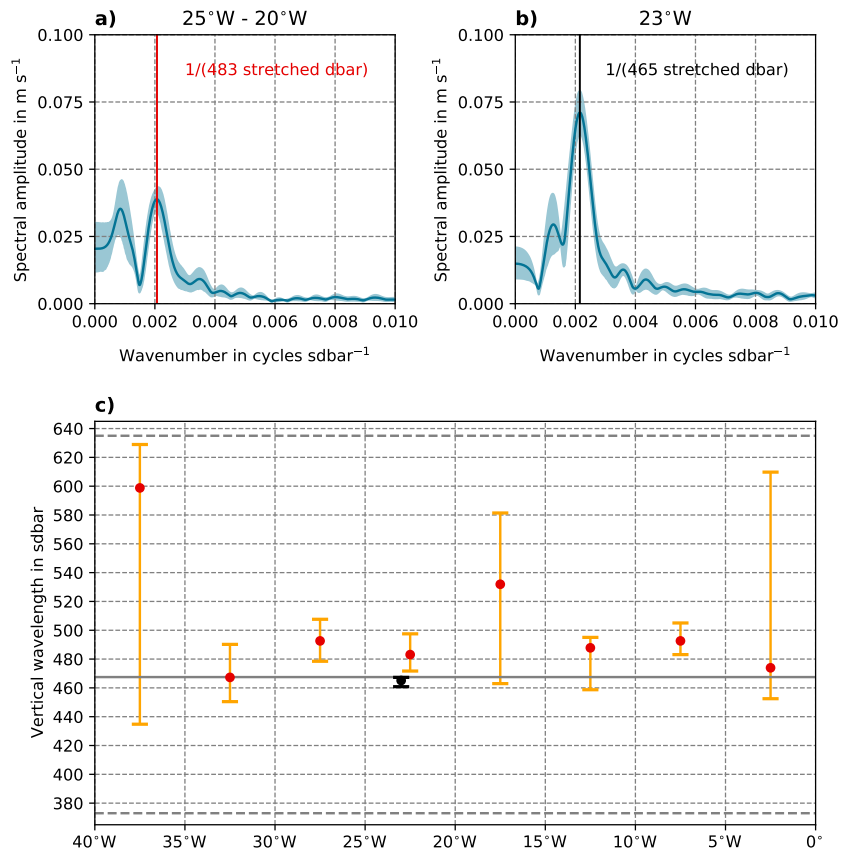
Fig. 12. Vertical wavelength of the Atlantic EDJ on the equator. Panel a: Vertical wavenumber spectrum of (stretched and scaled) equatorial geostrophic zonal velocity between 400 and 2000 m depth and between 20 and 25°W, reconstructed from hydrographic Argo float data. Because the data were otherwise too noisy, they were temporally filtered to contain only variability on the EDJ frequency. The solid blue line indicates the mean of all spectra calculated separately for each monthly profile, the area between the 25% and the 75% quantile of all spectra is shaded. The location of the EDJ peak is indicated in red with corresponding red text. Panel b: As Panel a, but from equatorial zonal velocity at 23°W measured by moored current meters for comparison. Here the EDJ peak is indicated in black. Panel c: Location of EDJ peak for all 5° longitude bins (in red), together with 95% confidence intervals obtained by bootstrapping (in orange). The value and confidence interval from the mooring data are drawn in black. For comparison, the vertical wavelength estimate by Youngs and Johnson (2015) from shipboard CTD measurements is indicated by the solid grey line, their 95% confidence interval by the dashed grey lines.

confidence interval between 4.56 years and 4.64 years) fits well to earlier estimates using the moored velocity measurements from 23°W (e.g. Brandt et al. 2011; Claus et al. 2016; Greatbatch et al. 2018), and also confirms the most recent basin-wide estimate from shipboard CTD measurements by Youngs and Johnson (2015), but with a smaller confidence interval. Our EDJ amplitude and phase estimates from the Argo float displacement data represent the first detailed assessment of the basin-wide horizontal structure of the Atlantic EDJ, albeit only at 1000 m depth: The horizontal shape that the EDJ assume in the basin has so far only been predicted with models (e.g. Greatbatch et al. 2012; Claus et al. 2014, 2016). In our results, it can be seen that the Atlantic EDJ are slightly narrower in the basin center than towards the west and east, which is suggestive of long Rossby wave focussing due to β-dispersion (Schopf et al. 1981). This focussing effect is likely reduced by the

mean flow around the equator, and by enhanced momentum dissipation (Claus et al. 2014; Greatbatch et al. 2012), but evidently not prevented completely. The zonal wavelength of the Atlantic EDJ is highly dependent on latitude, because of the different meridional structures and zonal wavelengths of the constituting Kelvin and Rossby wave components. Our estimate confirms and complements the estimate of Youngs and Johnson (2015) who only calculated the zonal wavelength of the Rossby wave component off the equator, but not the zonal wavelength of the entire EDJ on the equator, which is about twice as large as that of the Rossby wave component alone. Claus et al. (2016) have found similar results with a shallow water model of the Atlantic EDJ.

Since the Argo float displacement data are only abundant at 1000 m depth, it is not possible to estimate the vertical scale of the EDJ. Instead, we estimate it from hy-
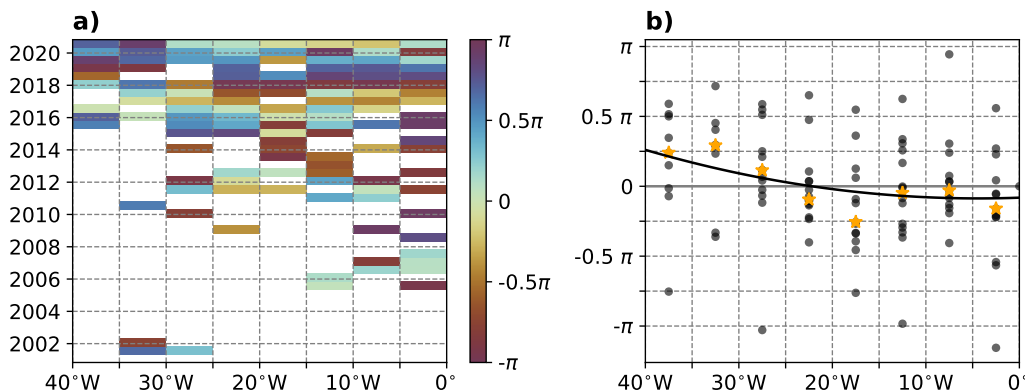
FIG. 13. Eastern deepening of the Atlantic EDJ. Panel a: Phase obtained by vertical harmonic fitting of six-month averages of the (stretched and scaled) reconstructed geostrophic zonal velocity from hydrographic Argo data. Panel b: Phase anomalies as a function of longitude. The anomalies have been calculated by subtracting the mean over all longitudes for every available point in time separately, and are drawn as grey markers. The median at each longitude is indicated by an orange asterisk. A least-squares quadratic fit to the data, given by $8.6 \cdot 10^{-4} \lambda^2 + 7.6 \cdot 10^{-3} \lambda - 0.26$ where λ is the longitude in degrees, is shown in black.

drographic profiles measured by the floats, using the fact that the EDJ are approximately in geostrophic balance. Our results compare well with the estimate from Youngs and Johnson (2015), and even have smaller confidence intervals. However, since the reconstruction of geostrophic velocity from the equatorial density field is somewhat noisy, and there is no systematic change of vertical EDJ scale with longitude visible in our results, we suggest that the moored velocity measurements at 23°W should preferably be used to obtain a good estimate of the Atlantic EDJs' vertical wavelength.

Our results confirm the similarity of the Atlantic EDJ to a resonant equatorial basin mode (Cane and Moore 1981), which has been suggested by several modelling studies (e.g. d'Orgeville et al. 2007; Ascani et al. 2015; Matthießen et al. 2015, 2017) and from analysis of the EDJ period and vertical scale from the moored velocity measurements at 23°W (e.g. Claus et al. 2016; Greatbatch et al. 2018). The theoretical period for the gravest equatorial basin mode is given by

$$T_n = \frac{4L}{c_n} \qquad (11)$$

where L is the width of the basin, and n is the baroclinic mode number. If we take $L = 52°$ as the width of the equatorial Atlantic at 1000 m depth, and $c_n = 0.16\,\mathrm{m\,s^{-1}}$ for the dominant vertical mode of the EDJ $n = 17$, as determined by a vertical mode decomposition of the moored zonal velocity measurements from 23°W as described in detail in Claus et al. (2016), we get a theoretical EDJ period of $T_n = 4.57$ years, which fits well to our estimate of 4.6 ± 0.04 years. We also find that the amplitude of the Atlantic EDJ is largest in the central part of the basin (though not exactly in the basin center, see below), and decreases towards

the western and eastern boundaries. Furthermore, the Atlantic EDJ signal that we find in Argo data is dominantly composed of an equatorial Kelvin wave and a first meridional mode Rossby wave, with some contribution from higher meridional mode Rossby waves close to the eastern boundary. All this corresponds well to the structure of a resonant equatorial basin mode (Cane and Moore 1981).

However, there are also some differences between the EDJ in the real Atlantic ocean and a theoretical (linear) equatorial basin mode as described by Cane and Moore (1981). In the latter, the amplitudes of the equatorial Kelvin wave and the first meridional mode Rossby wave should be similar (Cane and Moore 1981; Cane and Sarachik 1977), but our results confirm the finding of Youngs and Johnson (2015) that the Atlantic EDJ are dominated by a much stronger Rossby wave signal. This seems to be a special feature of the Atlantic EDJ, since Youngs and Johnson (2015) find that in the Indian and Pacific Oceans the equatorial Kelvin and first meridional mode Rossby wave amplitudes are much more similar. A possible explanation could be topographic differences between the oceans, e.g. the distinctive Gulf of Guinea in the Atlantic, that might lead to an asymmetry in the energy of the EDJ wave components. Another difference between the real Atlantic EDJ and a theoretical equatorial basin mode is the location of the zonal velocity amplitude maximum. Theoretical linear basin modes have their zonal velocity maximum in the center of the basin (Cane and Moore 1981), whereas our Argo data analysis shows that the amplitude maximum of the Atlantic EDJ is not located in the basin center but shifted to the west. Additionally, the phase difference between the Kelvin and the first meridional mode Rossby wave in the center of the basin is approximately 1.4π, although it should be 1π for a theoretical basin mode. These differ-
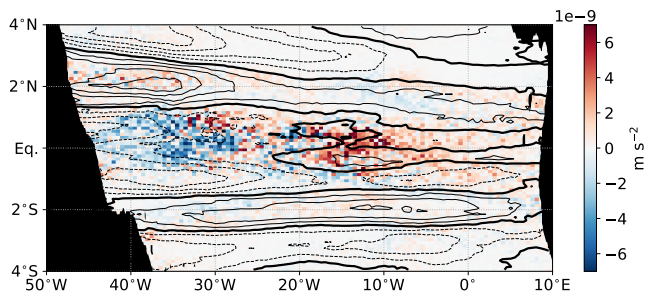
FIG. 14. Acceleration of the mean zonal velocity at 1000 m depth through the zonal self-advection of the Atlantic EDJ. The color shading shows the acceleration of the time mean zonal velocity $\overline{u}$ through the term $-\partial \left(\overline{u'u'} \right) / \partial x$, where the overbar denotes a time average and u' denotes the EDJ, i.e. zonal velocity variability with a time scale of 4.6 years. The time mean zonal velocity field at 1000 m depth is drawn as black contours. The thick solid line indicates the zero contour, the thin contours are spaced 0.01 m s^{-1} apart and solid for positive values, dashed for negative values.

ences could be indications of the effect of nonlinearity on the appearance of equatorial basin modes in the real ocean.

b. Nonlinear acceleration of time mean zonal flow by Atlantic EDJ

It has been suggested by idealized model studies that the EDJ nonlinearly transfer some energy to the time mean zonal currents at depth (Ascani et al. 2015; Bastin et al. 2020). The term that has been found to be largely responsible for this energy transfer in the models is the zonal self-advection of the EDJ, or

$$-\frac{\partial \left(\overline{u'u'} \right)}{\partial x} \qquad (12)$$

where the overbar denotes a time average, and u' is the zonal velocity variability at a time scale of 4.6 years, i.e. the Atlantic EDJ. We calculate this term from the Argo observations of the Atlantic EDJ at 1000 m depth, to see whether this can confirm the model results. The acceleration of the mean zonal flow due to (12) is shown in Figure 14, together with the time mean zonal flow at 1000 m depth. Because the EDJ are so strong compared to the time mean flow, the EDJ variability has been removed from the zonal velocity data before calculating the time average to prevent biases related to uneven sampling of different EDJ phases. Indeed, the acceleration due to the zonal self-advection of the EDJ in the Argo data shows very similar patterns as suggested by the model studies. In the western part of the basin, the EDJ strengthen the equatorial mean westward flow, as well as the flanking mean eastward jets at about 2°S and 2°N (although for the flanking jets, the acceleration is weak compared to the equator). In the center of the basin, however, where the EDJ have their amplitude

maximum, the sign of their zonal self-advection changes, leading to eastward acceleration of the mean zonal flow on the equator in the eastern part of the basin. This change of sign in the center of the basin can also be seen in the mean zonal velocity field.

c. EDJ signals in the Indian and Pacific Oceans

Equatorial deep jets have previously been found in all three ocean basins (e.g. Youngs and Johnson 2015). However, there is agreement that in the Pacific and Indian Oceans, the EDJ signal is considerably weaker than in the Atlantic. This is also visible in the Argo velocity data from 1000 m depth. In Figure 15a, a Hovmöller diagram of zonal velocity at the equator is shown for the Indian

FIG. 15. Panel a: Hovmöller diagram of zonal velocity at 1000 m depth along the equator in the Indian and Pacific Oceans, from the YoMaHa'07 dataset. The shown zonal velocity values are averages between 1°S and 1°N, and over 5° longitude bins. Positive values mean eastward velocity, negative westward velocity. Panels b and c: Lomb-Scargle periodograms of equatorial zonal velocity at 1000 m depth in the b) Indian and c) Pacific Oceans.

and Pacific Oceans (the velocity values shown are averaged between 1°S and 1°N, as well as over 5° longitude bins). In the Atlantic, a clear interannual variation of the equatorial zonal velocity is visible (cf. Figure 1), whereas in the Indian Ocean high-frequency variability (or noise) is prevalent. The most dominant signal in the Pacific is the annual cycle, although some superposition of variability on longer time scales is also perceptible. This is also visible in the spectra shown in Figure 15b (Indian Ocean) and 15c (Pacific Ocean). In the Pacific, no peak stands out at very low frequencies, where the EDJ would appear. In the Indian Ocean, a peak is visible at a frequency of about $0.22\,\text{years}^{-1}$, but only at very few longitudes. These are located in the western part of the basin. A possible reason for the absence of a Pacific EDJ signal in the Argo float displacement data at 1000 m depth is the long periodicity of the Pacific EDJ which is estimated to be between 12 years (Youngs and Johnson 2015) and several decades (Johnson et al. 2002), whereas there is sufficient data coverage in the YoMaHa'07 data only for the last 10 years. In the Indian Ocean, the absence of an EDJ signal could be due to the shallower mid-ocean bathymetry, reaching up to about 1000 m. Measurements of the EDJ in the Indian Ocean have generally been made at shallower depths (e.g. Luyten and Swallow 1976). We thus suggest that more data or maybe data at different depths are needed to pick up the EDJ signals in the Indian and Pacific Oceans.

d. Outlook

An application for which this new estimation of Atlantic EDJ characteristics from Argo data might be highly relevant, is the modelling of the tropical Atlantic Ocean. Despite the EDJs' likely importance for both interannual surface climate variability and deep ocean nutrient and oxygen transport, current ocean models and coupled forecasting systems are generally not able to faithfully simulate them. A possible way to include EDJ in ocean models or forecasting systems would be to add a forcing term to the momentum equation to create and maintain the currents, conceptually based on the real-world mechanism of momentum being fluxed into the EDJ due to the deformation of intraseasonal waves (Greatbatch et al. 2018; Bastin et al. 2020). For this, a forcing dataset is necessary that recreates the EDJs' characteristics as well as possible, and in particular the EDJs' phase needs to be estimated from a continuously running observing system like Argo or long-term current meter moorings.

Data availability statement. The Argo float data are openly available through http://apdrc.soest.hawaii.edu/projects/Argo/data/trjctry/yomaha07.dat.gz (YoMaHa'07 deep velocity dataset, our version downloaded on July 1, 2020) and ftp://ftp.ifremer.fr/ifremer/argo/geo/atlantic_ocean/ (hydrographic Argo float profiles, our version downloaded on July 20, 2020). The mooring data can be accessed through www.pangaea.de or https://zenodo.org/record/4478285#.YNYNxC0es0o. All analysis scripts will be published on Zenodo if the manuscript is accepted.

References

Argo, 2020: Argo float data and metadata from Global Data Assembly Centre (Argo GDAC). doi:10.17882/42182.

Argo Data Management Team, 2019: Argo user's manual V3.3. doi:10.13155/29825.

Ascani, F., E. Firing, P. Dutrieux, J. P. McCreary, and A. Ishida, 2010: Deep Equatorial Ocean Circulation Induced by a Forced-Dissipated Yanai Beam. *Journal of Physical Oceanography*, **40**, 1118–1142, doi:10.1175/2010JPO4356.1.

Ascani, F., E. Firing, J. P. McCreary, P. Brandt, and R. J. Greatbatch, 2015: The Deep Equatorial Ocean Circulation in Wind-Forced Numerical Solutions. *Journal of Physical Oceanography*, **45**, 1709–1734, doi:10.1175/JPO-D-14-0171.1.

Bastin, S., M. Claus, P. Brandt, and R. J. Greatbatch, 2020: Equatorial Deep Jets and Their Influence on the Mean Equatorial Circulation in an Idealized Ocean Model Forced by Intraseasonal Momentum Flux Convergence. *Geophysical Research Letters*, **47**, e2020GL087808, doi:10.1029/2020GL087808.

Brandt, P., M. Claus, R. J. Greatbatch, R. Kopte, J. M. Toole, W. E. Johns, and C. W. Böning, 2016: Annual and Semiannual Cycle of Equatorial Atlantic Circulation Associated with Basin-Mode Resonance. *Journal of Physical Oceanography*, **46**, 3011–3029, doi:10.1175/JPO-D-15-0248.1.

Brandt, P., A. Funk, V. Hormann, M. Dengler, R. J. Greatbatch, and J. M. Toole, 2011: Interannual atmospheric variability forced by the deep equatorial Atlantic Ocean. *Nature*, **473**, 497–500, doi:10.1038/nature10013.

Brandt, P., V. Hormann, B. Bourlès, J. Fischer, F. A. Schott, L. Stramma, and M. Dengler, 2008: Oxygen tongues and zonal currents in the equatorial Atlantic. *Journal of Geophysical Research*, **113**, C04 012, doi:10.1029/2007JC004435.

Brandt, P., and Coauthors, 2012: Ventilation of the equatorial Atlantic by the equatorial deep jets. *Journal of Geophysical Research*, **117**, C12 015, doi:10.1029/2012JC008118.

Brandt, P., and Coauthors, 2015: On the role of circulation and mixing in the ventilation of oxygen minimum zones with a focus on the eastern tropical North Atlantic. *Biogeosciences*, **12**, 489–512, doi:10.5194/bg-12-489-2015.

Bunge, L., C. Provost, B. L. Hua, and A. Kartavtseff, 2008: Variability at Intermediate Depths at the Equator in the Atlantic Ocean in 2000–06: Annual Cycle, Equatorial Deep Jets, and Intraseasonal Meridional Velocity Fluctuations. *Journal of Physical Oceanography*, **38**, 1794–1806, doi:10.1175/2008JPO3781.1.

Bunge, L., C. Provost, J. M. Lilly, M. d'Orgeville, A. Kartavtseff, and J.-L. Melice, 2006: Variability of the Horizontal Velocity Structure in the Upper 1600 m of the Water Column on the Equator at 10°W. *Journal of Physical Oceanography*, **36**, 1287–1304, doi:10.1175/JPO2908.1.

Cane, M. A., and D. W. Moore, 1981: A Note on Low-Frequency Equatorial Basin Modes. *Journal of Physical Oceanography*, **11**, 1578–1584, doi:10.1175/1520-0485(1981)011<1578:ANOLFE>2.0.CO;2.

Cane, M. A., and E. S. Sarachik, 1977: Forced baroclinic ocean motions: II. The linear equatorial bounded case. *Journal of Marine Research*, **35**, 395–432.

Claus, M., R. J. Greatbatch, and P. Brandt, 2014: Influence of the Barotropic Mean Flow on the Width and the Structure of the Atlantic Equatorial Deep Jets. *Journal of Physical Oceanography*, **44**, 2485–2497, doi:10.1175/JPO-D-14-0056.1.

Claus, M., R. J. Greatbatch, P. Brandt, and J. M. Toole, 2016: Forcing of the Atlantic Equatorial Deep Jets Derived from Observations. *Journal of Physical Oceanography*, **46**, 3549–3562, doi:10.1175/JPO-D-16-0140.1.

Crameri, F., 2018: Scientific colour maps. *Zenodo*, doi:10.5281/zenodo.1243862.

Cravatte, S., W. S. Kessler, and F. Marin, 2012: Intermediate Zonal Jets in the Tropical Pacific Ocean Observed by Argo Floats. *Journal of Physical Oceanography*, **42**, 1475–1485, doi:10.1175/JPO-D-11-0206.1.

Cravatte, S., E. Kestenare, F. Marin, P. Dutrieux, and E. Firing, 2017: Subthermocline and Intermediate Zonal Currents in the Tropical Pacific Ocean: Paths and Vertical Structure. *Journal of Physical Oceanography*, **47**, 2305–2324, doi:10.1175/JPO-D-17-0043.1.

Delpech, A., S. Cravatte, F. Marin, Y. Morel, E. Gronchi, and E. Kestenare, 2020: Observed Tracer Fields Structuration by Mid-depth Zonal Jets in the Tropical Pacific. *Journal of Physical Oceanography*, **50**, 281–304, doi:10.1175/JPO-D-19-0132.1.

Delpech, A., C. Ménesguen, Y. Morel, L. N. Thomas, F. Marin, S. Cravatte, and S. Le Gentil, 2021: Intra-Annual Rossby Waves Destabilization as a Potential Driver of Low-Latitude Zonal Jets: Barotropic Dynamics. *Journal of Physical Oceanography*, **51**, 365–384, doi:10.1175/JPO-D-20-0180.1.

d'Orgeville, M., B. L. Hua, and H. Sasaki, 2007: Equatorial deep jets triggered by a large vertical scale variability within the western boundary layer. *Journal of Marine Research*, **65**, 1–25, doi:10.1357/002224007780388720.

Efron, B., 1979: The 1977 Rietz Lecture. Bootstrap Methods: Another Look at the Jackknife. *The Annals of Statistics*, **7**, 1–26, doi:10.1214/aos/1176344552.

Eriksen, C. C., 1982: Geostrophic equatorial deep jets. *Journal of Marine Research*, **40**, 143–157.

Gill, A. E., 1982: *Atmosphere-Ocean Dynamics*, International Geophysics Series, Vol. 30. Academic Press.

Gouriou, Y., B. Bourlès, H. Mercier, and R. Chuchla, 1999: Deep jets in the equatorial Atlantic Ocean. *Journal of Geophysical Research*, **104**, 21,217–21,226, doi:10.1029/1999JC900057.

Gouriou, Y., and Coauthors, 2001: Deep Circulation in the Equatorial Atlantic Ocean. *Geophysical Research Letters*, **28**, 819–822, doi:10.1029/2000GL012326.

Greatbatch, R. J., P. Brandt, M. Claus, S.-H. Didwischus, and Y. Fu, 2012: On the Width of the Equatorial Deep Jets. *Journal of Physical Oceanography*, **42**, 1729–1740, doi:10.1175/JPO-D-11-0238.1.

Greatbatch, R. J., and Coauthors, 2018: Evidence for the Maintenance of Slowly Varying Equatorial Currents by Intraseasonal Variability. *Geophysical Research Letters*, **45**, 1923–1929, doi:10.1002/2017GL076662.

Hayes, S. P., and H. B. Milburn, 1980: On the Vertical Structure of Velocity in the Eastern Equatorial Pacific. *Journal of Physical Oceanography*, **10**, 633–635, doi:10.1175/1520-0485(1980)010<0633:OTVSOV>2.0.CO;2.

Hua, B. L., M. d'Orgeville, M. D. Fruman, C. Ménesguen, R. Schopp, P. Klein, and H. Sasaki, 2008: Destabilization of mixed Rossby gravity waves and the formation of equatorial zonal jets. *Journal of Fluid Mechanics*, **610**, 311–341, doi:10.1017/S0022112008002656.

Hunter, J. D., 2007: Matplotlib: A 2D graphics environment. *Computing in Science & Engineering*, **9 (3)**, 90–95, doi:10.1109/MCSE.2007.55.

Jayne, S. R., D. Roemmich, N. Zilberman, S. C. Riser, K. S. Johnson, G. C. Johnson, and S. R. Piotrowicz, 2017: The Argo Program: Present and Future. *Oceanography*, **30**, 18–28, doi:10.5670/oceanog.2017.213.

Johnson, G. C., E. Kunze, K. E. McTaggart, and D. W. Moore, 2002: Temporal and Spatial Structure of the Equatorial Deep Jets in the Pacific Ocean. *Journal of Physical Oceanography*, **32**, 3396–3407, doi:10.1175/1520-0485(2002)032<3396:TASSOT>2.0.CO;2.

Johnson, G. C., and D. Zhang, 2003: Structure of the Atlantic Ocean Equatorial Deep Jets. *Journal of Physical Oceanography*, **33**, 600–609, doi:10.1175/1520-0485(2003)033<0600:SOTAOE>2.0.CO;2.

Leaman, K. D., and T. B. Sanford, 1975: Vertical Energy Propagation of Inertial Waves: A Vector Spectral Analysis of Velocity Profiles. *Journal of Geophysical Research*, **80**, 1975–1978, doi:10.1029/JC080i015p01975.

Lebedev, K. V., H. Yoshinari, N. A. Maximenko, and P. W. Hacker, 2007: YoMaHa'07: Velocity data assessed from trajectories of Argo floats at parking level and at the sea surface. *IPRC Technical Note No. 4(2)*, 16 p, updated as of July 1, 2020.

Leetmaa, A., and P. F. Spain, 1981: Results from a Velocity Transect Along the Equator from 125 to 159°W. *Journal of Physical Oceanography*, **11**, 1030–1033, doi:10.1175/1520-0485(1981) 011<1030:RFAVTA>2.0.CO;2.

Lomb, N. R., 1976: Least-squares frequency analysis of unequally spaced data. *Astrophysics and Space Science*, **39**, 447–462, doi: 10.1007/BF00648343.

Luyten, J. R., and J. C. Swallow, 1976: Equatorial undercurrents. *Deep-Sea Research*, **23**, 999–1001, doi:10.1016/0011-7471(76)90830-5.

Matthießen, J.-D., R. J. Greatbatch, P. Brandt, M. Claus, and S.-H. Didwischus, 2015: Influence of the equatorial deep jets on the north equatorial countercurrent. *Ocean Dynamics*, **65**, 1095–1102, doi: 10.1007/s10236-015-0855-5.

Matthießen, J.-D., R. J. Greatbatch, M. Claus, F. Ascani, and P. Brandt, 2017: The emergence of equatorial deep jets in an idealised primitive equation model: an interpretation in terms of basin modes. *Ocean Dynamics*, **67**, 1511–1522, doi:10.1007/s10236-017-1111-y.

Ménesguen, C., A. Delpech, F. Marin, S. Cravatte, F. Schopp, and Y. Morel, 2019: Observations and Mechanisms for the Formation of Deep Equatorial and Tropical Circulation. *Earth and Space Science*, **6**, 370–386, doi:10.1029/2018EA000438.

Ponte, R. M., J. Luyten, and P. L. Richardson, 1990: Equatorial deep jets in the Atlantic Ocean. *Deep-Sea Research*, **37**, 711–713, doi: 10.1016/0198-0149(90)90100-A.

Scargle, J. D., 1982: Studies in astronomical time series analysis. II. Statistical aspects of spectral analysis of unevenly spaced data. *The Astrophysical Journal*, **263**, 835–853, doi:10.1086/160554.

Schmid, C., B. Bourlès, and Y. Gouriou, 2005: Impact of the equatorial deep jets on estimates of zonal transports in the Atlantic. *Deep-Sea Research II*, **52**, 409–428, doi:10.1016/j.dsr2.2004.12.008.

Schopf, P. S., D. L. T. Anderson, and R. Smith, 1981: Beta-dispersion of low-frequency Rossby waves. *Dynamics of Atmospheres and Oceans*, **5**, 187–214, doi:10.1016/0377-0265(81)90011-7.

Tuchen, F. P., P. Brandt, M. Claus, and R. Hummels, 2018: Deep Intraseasonal Variability in the Central Equatorial Atlantic. *Journal of Physical Oceanography*, **48**, 2851–2865, doi:10.1175/ JPO-D-18-0059.1.

Youngs, M. K., and G. C. Johnson, 2015: Basin-Wavelength Equatorial Deep Jet Signals across Three Oceans. *Journal of Physical Oceanography*, **45**, 2134–2148, doi:10.1175/JPO-D-14-0181.1.

4 Factors influencing the meridional width of the equatorial deep jets in different idealised model setups

4.1 Introduction

The structure of the Equatorial Deep Jets (EDJ) shows some peculiarities that deviate from the theoretical appearance of an inviscid linear equatorial basin mode with the corresponding vertical scale. One of them is the jets' cross-equatorial width which has been observed to be larger by a factor of 1.5 than theoretically expected. Muench et al. (1994) found this enhanced meridional width for the EDJ in the Pacific Ocean from looking at a zonal velocity section between 3°S and 3°N and at 159°W, averaged over 16 months. For the Atlantic EDJ, a widening by the same factor of 1.5 has been shown by Johnson and Zhang (2003) from an analysis of shipboard CTD profiles, and has later been confirmed by other studies, e.g. Youngs and Johnson (2015), as well as in Chapter 3 of this thesis. Muench et al. (1994) suggested that the widening was an artefact caused by time averaging over EDJ that meander due to meridional advection by intraseasonal waves.

An alternative theory was put forward by Greatbatch et al. (2012) who suggested that the strong intraseasonal velocity variability found at the equator leads to lateral mixing of momentum. They argue that, because the EDJ are close to geostrophic balance, a strong lateral mixing of momentum weakening the zonal flow on the equator requires a reduction of the meridional density gradient north and south of the equator. This can be achieved either by enhanced diapycnal mixing, or by a meridional widening of the equatorial geostrophic flow, i.e. the EDJ. Since the diapycnal mixing around the equator is weak (Dengler and Quadfasel, 2002; Gregg et al., 2003), the lateral mixing of momentum thus has to be balanced by a larger cross-equatorial width of the EDJ (Greatbatch et al., 2012). Indeed, Greatbatch et al. (2012) could show with a shallow water model that the cross-equatorial width of the simulated EDJ gets larger when the value of the lateral eddy viscosity in the model is increased. They note that the meandering suggested by Muench et al. (1994) is reversible, whereas the EDJ widening through lateral mixing of momentum is an irreversible process.

Both Muench et al. (1994) and Greatbatch et al. (2012) suggest that the widening of the EDJ about the equator is connected to the intraseasonal variability in the deep equatorial ocean, although in the theory of Greatbatch et al. (2012) other processes which lead to enhanced lateral mixing of momentum could also play a role. In this chapter, the relation between the strength of intraseasonal variability and the cross-equatorial width of the EDJ is therefore investigated with the help of different idealised model configurations of the tropical Atlantic Ocean. Additionally, the relative importance of the two suggested mechanisms, i.e. the reversible meandering through intraseasonal

meridional advection versus the irreversible enhanced lateral mixing of momentum associated with the intraseasonal variability, for the enhanced mean EDJ width is assessed in these models.

As described in Chapter 1, the EDJ are very similar to the gravest resonant equatorial basin mode (Cane and Moore, 1981) of the corresponding dominant baroclinic mode, and thus consist of the sum of an eastward propagating equatorial Kelvin wave and its reflection as westward propagating long Rossby waves. Because the zonal velocity signature of an equatorial Kelvin wave has a larger cross-equatorial width than that of a first meridional mode long Rossby wave of the corresponding vertical mode, the ratio between the Kelvin and first meridional mode Rossby wave amplitudes in the EDJ basin mode has an influence on the meridional width of the EDJ. The importance of this for the meridional EDJ width is also investigated in this chapter.

The chapter is structured as follows: In Section 4.2, a description of the model configurations as well as analysis methods is provided. In Section 4.3, the results are presented, starting with an overview of the model configurations' ability to simulate EDJ and a description of the differences in the cross-equatorial width of the EDJ in Section 4.3.1. This is followed by Section 4.3.2 where the amplitude contributions of the equatorial Kelvin and first meridional mode Rossby wave to the EDJ are discussed. The importance of meandering versus instantaneous widening of the EDJ in setting their time mean cross-equatorial width is investigated in Section 4.3.3, as well as the relationship between the meridional EDJ width and the intraseasonal variability in the models. Finally, a discussion of the results is provided in Section 4.4.

4.2 Model and methods

4.2.1 Model configurations

The ocean model that has been used for all simulations in this thesis is the Nucleus for European Modelling of the Ocean (NEMO, Madec et al., 2017), Version 3.6.

The basic model setup is based on the studies by Ascani et al. (2015) and Matthießen et al. (2015, 2017), who succeeded in simulating EDJ with an idealised model of the tropical Atlantic, although they used the Parallel Ocean Program (POP), respectively MITgcm ocean models instead of NEMO. All models are ocean-only simulations for a basin analogous to the tropical Atlantic, but with closed boundaries at 20°S and 20°N. The horizontal resolution is set to $0.25° \times 0.25°$. Following Ascani et al. (2015), the horizontal mixing of tracer and momentum is parameterised using biharmonic diffusion/viscosity with a coefficient of $-2 \cdot 10^{10}\,\mathrm{m^4\,s^{-1}}$, and the vertical mixing scheme is Richardson number dependent (Pacanowski and Philander, 1981) with a background diffusivity of $10^{-5}\,\mathrm{m^2\,s^{-1}}$. The TEOS-10 equation of state is used for all simulations. All model runs are initialised with horizontally and temporally averaged vertical profiles of tropical Atlantic (between 20°S and 20°N) salinity and temperature from the World Ocean Atlas 2018 (WOA18, Locarnini et al., 2019; Zweng et al., 2019). The in-situ temperature and practical salinity from WOA18 have been converted to conservative temperature and absolute salinity with a Python implementation of the Gibbs Sea Water Library (*gsw 3.3.1*). At the surface, the temperature and salinity are restored to their initialisation value with a damping time scale of 30 days, to maintain a reasonable stratification of the water column over time.

The model setup from which all the others are derived is called L200-WIND (same as Sim-WIND in Chapter 2). The domain is rectangular with a width of 55° to mimic the Atlantic Ocean at the equator, and has a flat bottom at 5000 m depth. There are 200 model levels, with a vertical resolution of 5 m close to the surface, approximately 20 m in the depth range of the EDJ, and increasing to 50 m close to the bottom (the thickness of all vertical levels is shown in Figure S1 in Chapter 2.A). L200-WIND is forced with zonally and temporally averaged wind stress from the NCEP/NCAR reanalysis (Kalnay et al., 1996; Kistler et al., 2001). It has a free slip boundary condition at the bottom, because Ascani et al. (2015) and Matthießen (2017) found that bottom friction reduces the ability of the model to simulate EDJ. In L200-WIND, reasonably realistic EDJ develop in the model, as shown in Chapter 2 and also visible in Figure 4.1 where Hovmöller diagrams of the zonal velocity in the centre of the model basin are shown for all model runs used in this thesis (continued in Figures 4.2 and 4.3).

From L200-WIND, a number of other model setups are derived, all of which are listed with their distinguishing features in Table 4.1. There are two different vertical resolutions, marked by the number after the L in the configuration name. L200 is the fine vertical resolution, and L75 is a coarser one that is one of the commonly used vertical axes by NEMO ocean models, e.g. by the Global Seasonal forecast system of the MetOffice (MacLachlan et al., 2015). Note that there are some configurations that are named L220; these have the same vertical resolution as the L200 configurations but extend to depths greater than 5000 m and thus have additional layers at these depths because they include realistic bathymetry. Another thing that the configurations differ in is the forcing. There are two types of forcing applied. First, the wind forcing, i.e. zonally and temporally averaged NCEP/NCAR wind stress, is either switched on or off. Second, there is the IMFC (Intraseasonal Momentum Flux Convergence) forcing, which is a tendency added to the zonal momentum equation in the model at every grid point and time step, as already described in Chapters 2 and 2.A. It is the intraseasonal eddy flux from the meridional advection term in the zonal momentum equation, i.e.

$$-\frac{\partial(\overline{u'v'})}{\partial y} \tag{4.1}$$

where the prime denotes variability on time scales smaller than 70 days (or intraseasonal) and the overbar means variability on time scales larger than 70 days. This term is thought to be responsible for energy transfer from intraseasonal waves to the EDJ and other slowly varying currents (for details see Greatbatch et al., 2018). For the IMFC model forcing, the term (4.1) is diagnosed from the base model configuration L200-WIND, to be applied to other model configurations. There are three different flavours of IMFC forcing in the different model experiments: "edj" includes only one Fourier component of the IMFC, namely that with the frequency of the EDJ; "full" includes the entire IMFC diagnosed from L200-WIND varying on all time scales; and "mean" includes only the time mean of the IMFC. The last differences between the model setups concern the use of realistic coastlines and bathymetry, and the bottom boundary condition which is either free slip like in L200-WIND or a linear bottom friction. All model configurations that do not have realistic coastlines and bathymetry are rectangular and have a flat bottom like L200-WIND. The model setups that do have realistic coastlines and bathymetry still have closed boundaries at 20°S and 20°N.

Table 4.1: Overview of model runs used in this thesis. Italic names are the alternative names used in Chapter 2.

Name	Wind forcing	IMFC forcing	Bathymetry and coastlines	Bottom friction	EDJ	Chapters
L200-WIND *Sim-WIND*	yes	no	no	no	yes	*2*, 4, 5
L200-edjIMFC *Sim-IMFC*	no	edj	no	no	yes	*2*, 4
L200-2edjIMFC *Sim-doubledIMFC*	no	$2 \times$ edj	no	no	yes	*2*, 4
L200-fullIMFC	no	full	no	no	yes	4, 5
L200-meanIMFC	no	mean	no	no	no	4, 5
L200-WIND-bfric	yes	no	no	yes	no	4
L220-bathy-WIND	yes	no	yes	yes	no	4
L220-bathy-edjIMFC	no	edj	yes	yes	yes	4
L220-bathy-WIND-edjIMFC	yes	edj	yes	yes	yes	4
L220-bathy-fullIMFC	no	full	yes	yes	yes	4
L75-WIND	yes	no	no	no	(no)	4
L75-edjIMFC	no	edj	no	no	yes	4
L75-fullIMFC	no	full	no	no	yes	4

4.2.2 Analysis methods

Vertical normal mode decomposition

Because the EDJ, unlike most other large-scale flow patterns in the ocean, are characterized by relatively small vertical wavelengths, it is instructive to separate the velocity field into its different vertical scales. This can be done by expressing the flow field's variation in the vertical as a sum of vertical normal modes, to get a sum of linearly independent components of the velocity field, each of which has its unique vertical structure and varies only in the horizontal and time. The first (or rather, order zero, since its structure function has no zero crossings) vertical mode is usually called the barotropic mode and comprises all motions with uniform vertical structure. The other modes, from mode one upwards, are called baroclinic modes and are characterized by decreasing vertical scales with increasing mode number.

The following explanation of the separation into vertical normal modes follows Kundu et al. (2012, Chapter 13.9.):

For an ocean with uniform stratification, in which the horizontal scales of motion are much larger than the vertical scale of motion, the linearised equations of motion can be written as

$$\frac{\partial u}{\partial x} + \frac{\partial v}{\partial y} + \frac{\partial w}{\partial z} = 0 \tag{4.2}$$

$$\frac{\partial u}{\partial t} - fv = -\frac{1}{\rho_0}\frac{\partial p}{\partial x} \tag{4.3}$$

$$\frac{\partial v}{\partial t} + fu = -\frac{1}{\rho_0}\frac{\partial p}{\partial y} \tag{4.4}$$

$$0 = -\frac{\partial p}{\partial z} - g\rho \tag{4.5}$$

$$\frac{\partial \rho}{\partial t} - \frac{\rho_0 N^2}{g}w = 0 \tag{4.6}$$

where x, y and z are the Cartesian coordinates towards the east, the north, and upward, t is the time, u, v and w are the zonal, meridional and vertical components of velocity, f is the Coriolis parameter, p and ρ are the perturbation pressure and density relative to a state of rest, ρ_0 is a constant average density, g is the acceleration due to gravity, and N is the buoyancy frequency with

$$N^2 = -\frac{g}{\rho_0}\frac{\partial \rho}{\partial z} \tag{4.7}$$

Solutions to this set of equations plus appropriate boundary conditions can be found with a separation of variables technique. The solutions then have the form

$$q = \sum_{n=0}^{\infty} q_n(x,y,t)\psi_n(z) \tag{4.8}$$

for a field variable q that depends on x, y, z and t. ψ_n now describes a fixed vertical structure for a certain n, and q_n is q projected onto the vertical structure in question. To write all variables in Eqs. (4.2) to (4.6) in terms of the same set of vertical structure functions ψ_n, one has to assume solutions of the form

$$[u,v,p/\rho_0] = \sum_{n=0}^{\infty}[u_n,v_n,p_n]\psi_n(z) \tag{4.9}$$

$$w = \sum_{n=0}^{\infty} w_n \int_{-H}^{z} \psi_n(z)dz \tag{4.10}$$

$$\rho = \sum_{n=0}^{\infty} \rho_n \frac{d\psi_n}{dz} \tag{4.11}$$

with the amplitudes u_n, v_n, p_n, w_n and ρ_n depending on x, y and t. z is the depth measured positive upward, and H is the water depth.

Inserting Eqs. (4.9) to (4.11) into the set of governing equations gives the following differential equation describing the vertical structure functions ψ_n:

$$\frac{d}{dz}\left(\frac{1}{N^2}\frac{d\psi_n}{dz}\right) + \frac{1}{c_n^2}\psi_n = 0 \tag{4.12}$$

where c_n is a constant that has the unit of velocity. Eq. (4.12), together with appropriate boundary conditions, is a Sturm-Liouville problem and thus has solutions that are orthogonal to each other, i.e. the resulting vertical normal modes will indeed form a basis of linearly independent vertical structures. The eigenvalues $\frac{1}{c_n^2}$ have physical significance, as it can be shown that each normal mode behaves as a homogeneous layer with an equivalent depth H_e defined by $c_n^2 = gH_e$. Hence, the c_n represent the gravity wave speed for the respective vertical normal mode.

Because all the ψ_n are orthogonal to each other, the amplitude $u_n(x,y,t)$ of the n-th mode is given

by

$$u_n = \frac{\int_{-H}^{0} u(x,y,z,t)\psi_n(z)dz}{\int_{-H}^{0} \psi_n^2(z)dz} \tag{4.13}$$

This works analoguously for the other variables, but is only done for the zonal velocity in this thesis because the focus is on the zonal EDJ.

To obtain the vertical structure functions ψ_n, a mean buoyancy frequency profile from the model, averaged along the equator, is used, and the eigenvalue problem given by Eq. (4.12) is solved with the following boundary conditions:

$$\frac{d\psi_n}{dz} = 0 \ \text{ at } z = -H \quad \text{(following from } w = 0) \tag{4.14}$$

$$\frac{d\psi_n}{dz} + \frac{N^2}{g}\psi_n = 0 \ \text{ at } z = 0 \quad \text{(following from } \frac{\partial p}{\partial t} = \rho_0 gw) \tag{4.15}$$

The zonal velocity field from the model is projected onto the vertical structure functions using Eq. (4.13). The resulting u_n can then be analyzed separately, e.g. by calculating vertical mode spectra as shown in Figure 4.1. The separation into vertical normal modes is also used here to vertically filter the zonal velocity by summing only the u_n of modes 15 to 22, to get rid of variability different from the EDJ.

Quantification of meridional EDJ width

The cross-equatorial width of the EDJ has usually been given as the e-folding scale of the meridional profile of zonal velocity amplitude (e.g. Greatbatch et al., 2012). This is continued here. To ensure comparability across all the meridional width estimates given in this chapter (e.g. also those of a theoretical inviscid Kelvin or Rossby wave), they are all determined by a fit of a Gaussian of the form

$$g(\theta) = a \cdot \exp\left(-\frac{1}{2}\frac{(\theta - \theta_c)^2}{\sigma^2}\right) \tag{4.16}$$

to the zonal velocity between 1.5°S and 1.5°N. Here, a is the amplitude, θ denotes latitude, θ_c is the position of the EDJ core (or maximum), and the meridional width of the EDJ is given by $W = \sqrt{2} \cdot \sigma$. The relatively narrow equatorial corridor between 1.5°S and 1.5°N is taken to reduce the influence of off-equatorial maxima in the zonal velocity field, such as associated with Rossby waves. The equatorial radius of deformation for a gravity wave speed of $16.2\,\text{cm}\,\text{s}^{-1}$ (corresponding to the EDJ peak baroclinic mode 19 from L200-WIND) is approximately 0.76°, well covered by the latitude range used for the fit.

The zonal velocity fields from the model configurations are filtered vertically before analysing the cross-equatorial EDJ width, such that only the EDJ variability is included in the analysis. This is done by decomposing the zonal velocity into vertical normal modes (see previous section) and retaining only the contributions of the vertical modes 15 to 22, which cover the EDJ peak (shown in Figures 4.1, 4.2 and 4.3).

A distinction is made between the quantification of the mean EDJ width and the instantaneous EDJ width. The mean EDJ width is determined by fitting Eq. (4.16) to the harmonic amplitude field of the vertically filtered zonal velocity varying at the EDJ period which is approximately 4.4 years in the models, whereas the instantaneous EDJ width as well as the EDJ widening due to meandering are determined by fitting Eq. (4.16) to temporal snapshots of the vertically filtered

74

zonal velocity field. The instantaneous EDJ width is then given as the average of $W = \sqrt{2} \cdot \sigma$. For the EDJ width due to meandering, the resulting distribution of the parameter θ_c, i.e. the shift of the EDJ core away from the equator, is used to produce a distribution of theoretical first meridional mode Rossby wave zonal velocity amplitude profiles with corresponding meridional shifts. From these, an average profile is calculated and the e-folding scale of this is determined as described above. Because the studies that reported the increased meridional width of the EDJ generally used an inviscid first meridional mode Rossby wave of corresponding vertical scale and frequency as the theoretical comparison, and on this basis calculated a widening of the EDJ by a factor of 1.5 (Johnson and Zhang, 2003; Youngs and Johnson, 2015), the width of an analytic inviscid first meridional mode Rossby wave is also used as a basis for comparison throughout this chapter.

Separation of Kelvin and first meridional mode Rossby wave

The contributions of the equatorial Kelvin wave and the first meridional mode Rossby wave to the EDJ are separated by a regression of the models' zonal velocity field onto the theoretical structures of the two waves, where the meridional velocity profile of the respective wave is specified and the waves' frequency is fixed to the dominant EDJ frequency, which in the models is approximately $f_{EDJ} = (4.4 \text{ years})^{-1}$. For both waves, a linear combination of a sine and a cosine with the respective frequency and meridional structure is fitted, such that the problem takes the form of a linear regression with four degrees of freedom. The optimisation problem is given by the following term that is minimised using a Python implementation of a least squares linear regression (*scipy.optimize.lsq_linear*, Version 1.6.2):

$$0.5 \cdot ||D(i,j) \cdot c(j) - u(i)||^2 \tag{4.17}$$

Here, u is the zonal velocity, i a combined multi-index for time and latitude, c is the coefficient vector to be determined with index $j = (1, 2, 3, 4)$, and the design matrix D is given by:

$$D = \begin{pmatrix} \cos(\omega \cdot t(i)) \cdot u_K(y(i)) \\ \sin(\omega \cdot t(i)) \cdot u_K(y(i)) \\ \cos(\omega \cdot t(i)) \cdot u_{R1}(y(i)) \\ \sin(\omega \cdot t(i)) \cdot u_{R1}(y(i)) \end{pmatrix}^T \tag{4.18}$$

The angular frequency $\omega = 2\pi f_{EDJ}$ is set to that of the EDJ, t is the time and y the northward distance from the equator in m. The meridional profiles of the zonal velocity signatures of the Kelvin (u_K) and first meridional mode Rossby (u_{R1}) waves are given by Eqs. (9) and (10) in Chapter 3. In this chapter, the EDJ peak baroclinic mode 19 from L200-WIND with a corresponding gravity wave speed of $16.2 \, \text{cm} \, \text{s}^{-1}$ is used for the theoretical wave profiles. u_K and u_{R1} are stretched meridionally before the regression, to account for the different meridional widths of the EDJ in the model configurations. The stretching factor is determined by detecting the mean latitude of the off-equatorial minima in the EDJ amplitude field, and dividing this latitude by the latitude of the theoretical Rossby wave zonal velocity profile zero crossing.

From the resulting coefficients c, the amplitude A and phase p of the Kelvin and Rossby wave can

then be computed as:

$$A_K = \sqrt{c(1)^2 + c(2)^2} \tag{4.19}$$

$$p_K = \arctan\left(-\frac{c(2)}{c(1)}\right) \tag{4.20}$$

$$A_{R1} = \sqrt{c(3)^2 + c(4)^2} \tag{4.21}$$

$$p_{R1} = \arctan\left(-\frac{c(4)}{c(3)}\right) \tag{4.22}$$

4.3 Results

4.3.1 EDJ in the different model experiments

In Figures 4.1, 4.2 and 4.3, Hovmöller diagrams of the zonal velocity from the centre of the model basin are shown for all model configurations listed in Table 4.1. Spectra of the zonal velocity from the model basin centre are shown as well, calculated after the zonal velocity has been decomposed into vertical normal modes.

When they are present, the EDJ are visible in the Hovmöller diagrams of equatorial zonal velocity as vertically alternating, downward propagating bands of currents. In the normal mode spectra, they appear as a peak close to the basin mode resonance curve, at a period of about 4.4 years. The observed period of the real Atlantic EDJ is with 4.6 years a bit larger (see Chapter 3). This difference might be due to the high degree of idealization of the model.

There are nine model configurations in which EDJ develop, which include apart from the basic L200-WIND only the model configurations forced with the "edj" or "full" flavour of the IMFC forcing:

- L200-WIND

- L200-edjIMFC

- L200-2edjIMFC

- L200-fullIMFC

- L220-bathy-edjIMFC

- L220-bathy-WIND-edjIMFC

- L220-bathy-fullIMFC

- L75-edjIMFC

- L75-fullIMFC

Results from these nine model configurations will therefore be used for the analysis of the meridional EDJ width in the rest of this chapter. Wind forcing without IMFC forcing is only enough to generate EDJ in the vertically finely resolved L200-WIND without bottom friction. When there is bottom friction included, no stable EDJ with downward phase propagation develop. Instead, as already noticed by Matthießen (2017) who did sensitivity experiments for simulating EDJ with the MITgcm ocean model, EDJ with upward phase propagation appear but they are not maintained
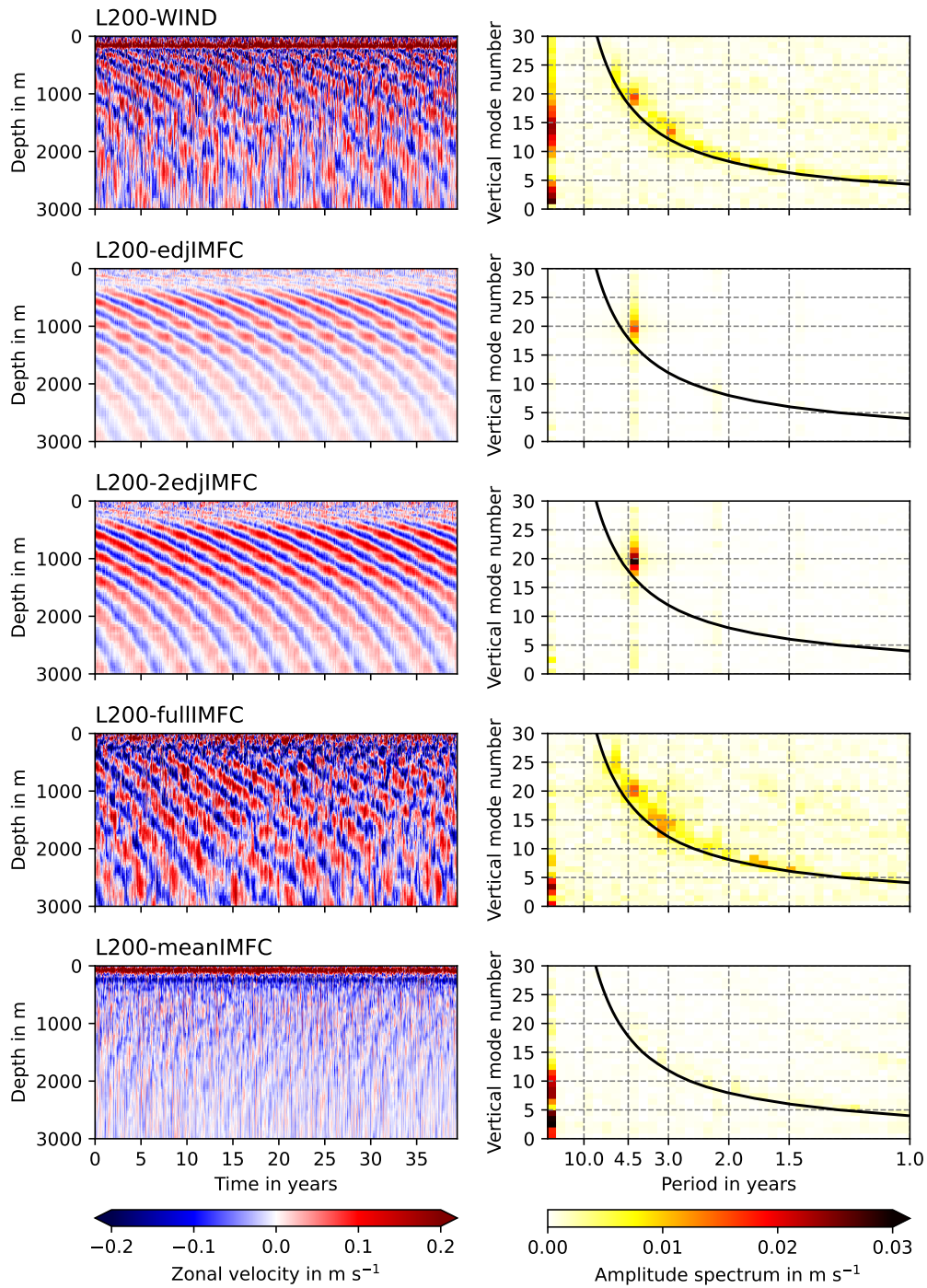
Figure 4.1: Hovmöller diagrams (left panels) and normal mode spectra (right panels) of the zonal velocity in the centre of the model basin, for the model configurations L200-WIND, L200-edjIMFC, L200-2edjIMFC, L200-fullIMFC, and L200-meanIMFC. Positive zonal velocity values indicate eastward velocity, negative values mean westward velocity. The solid black line in the right panels shows the resonance frequency for the gravest equatorial basin mode for each vertical normal mode. The spinup is excluded from all model runs except L200-WIND-bfric (Figure 4.2) where no EDJ develop and the model was therefore not run beyond 50 years, but from which the last 40 years are shown here anyway for better comparability to the rest of the model configurations. (Continued for other model runs in Figures 4.2 and 4.3.)
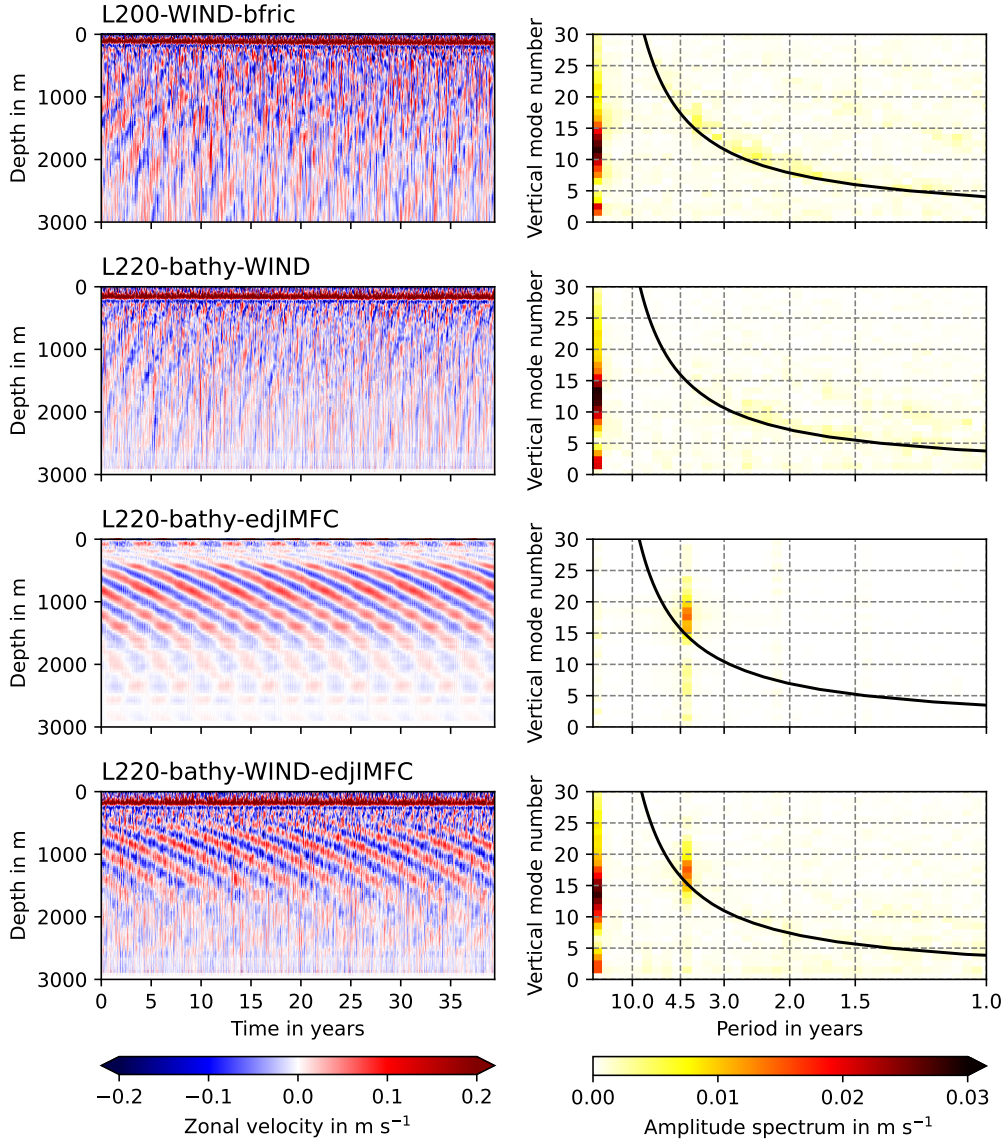
Figure 4.2: As Figure 4.1, but for the model configurations L200-WIND-bfric, L220-bathy-WIND, L220-bathy-edjIMFC, and L220-bathy-WIND-edjIMFC.

and become weaker over time. When there is no bottom friction but the vertical resolution is coarser (L75-WIND), downward propagating EDJ-like structures do develop (also already described for a similar configuration by Matthießen, 2017), but they are weaker, do not reach depths as large as in the finely resolved configuration, and also appear at other frequencies and normal modes in the spectrum. Therefore, also L75-WIND is not included in the further analyses of the meridional width of the EDJ in this chapter.

Across the nine model runs with EDJ, the cross-equatorial width of the deep jets varies quite a bit. Shown in Figure 4.4 are snapshots of the vertically filtered (modes 15 to 22 to show only the EDJ variability) zonal velocity at 1000 m depth, spaced one year apart, for L200-WIND and L200-edjIMFC. The EDJ are visible as strong zonal current bands on the equator, changing direction every few years and propagating from the east towards the west. It is visible that the EDJ in L200-WIND have a larger meridional scale than those in L200-edjIMFC. What can also be seen already by eye is that different mechanisms seem to contribute to the enhanced meridional EDJ
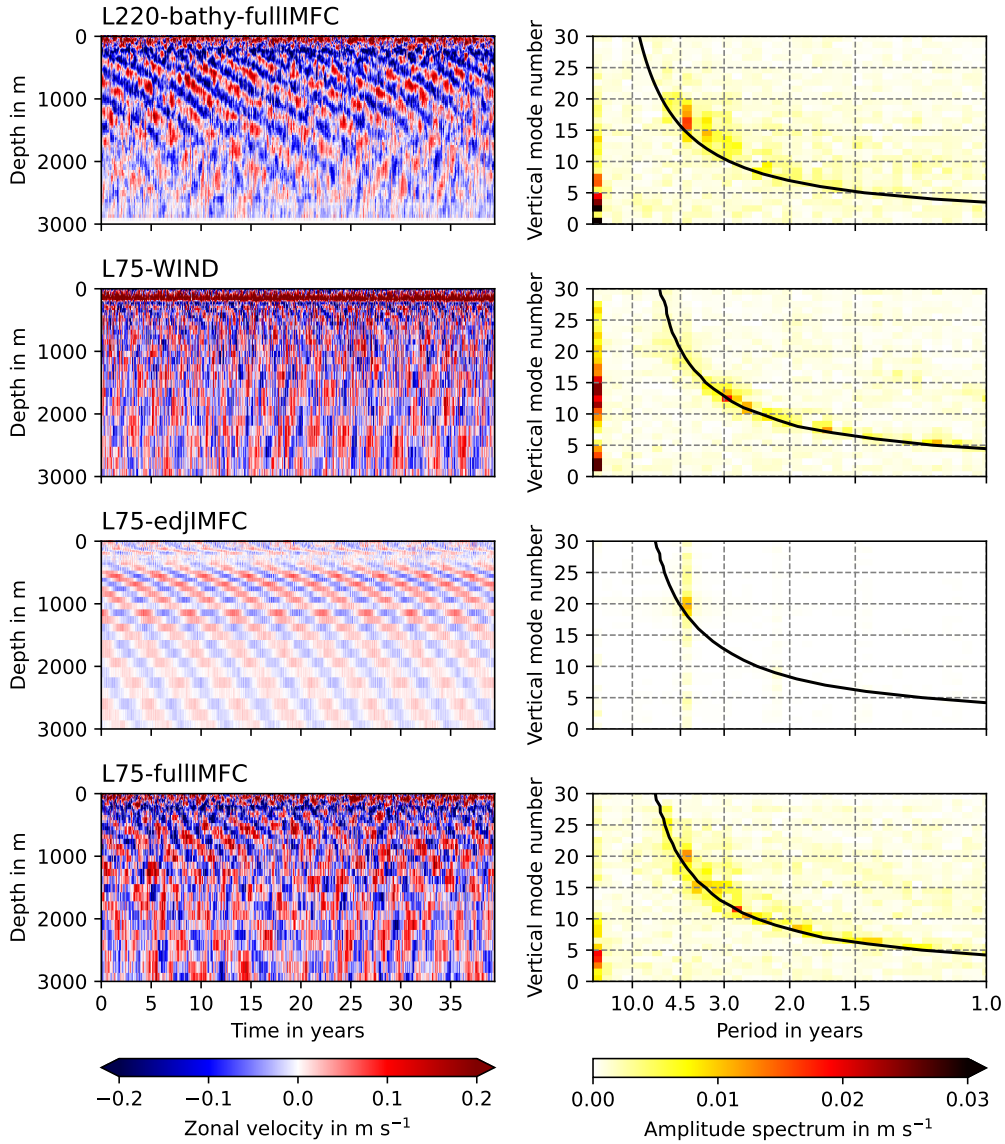
Figure 4.3: As Figure 4.1, but for the model configurations L220-bathy-fullIMFC, L75-WIND, L75-edjIMFC, and L75-fullIMFC.

width in L200-WIND: there is more meandering around the equator of the EDJ that would lead to a larger meridional scale in the time mean EDJ signature compared to L200-edjIMFC as suggested by Muench et al. (1994), but the EDJ also seem to have a larger instantaneous meridional width in L200-WIND than in L200-edjIMFC which could indicate an irreversible widening through enhanced lateral mixing of momentum as suggested by Greatbatch et al. (2012). The influence of these two different factors on the time mean meridional width is investigated for all nine model configurations with EDJ in Section 4.3.3.

The mean meridional EDJ width for all of the nine model runs is shown in Figure 4.5, together with the meridional width of an inviscid first meridional mode Rossby wave and an inviscid equatorial Kelvin wave with a corresponding vertical structure. The model runs are sorted by the mean meridional width of the EDJ, from small to large; this order will be kept for the following similar figures throughout the chapter. Also marked in Figure 4.5 is the value of the Rossby wave width enhanced by a factor of 1.5. The exact value of the meridional Rossby wave scale is a bit arbitrary,
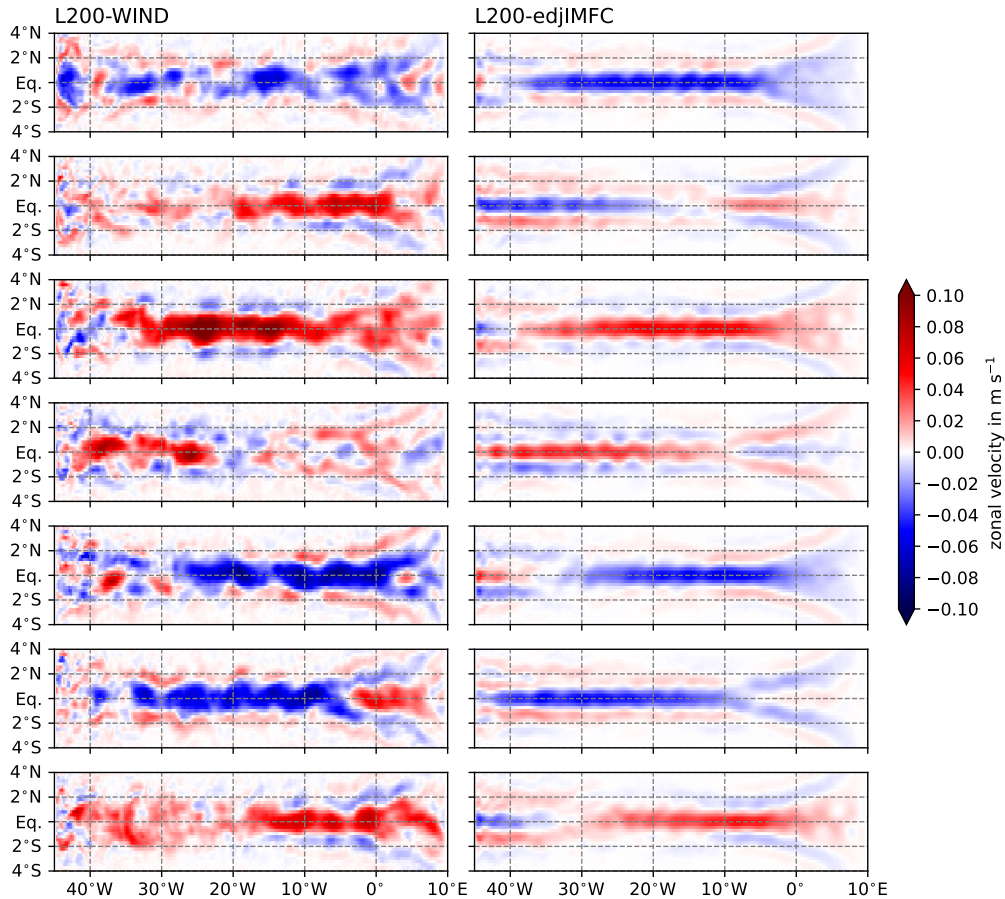
Figure 4.4: Yearly snapshots of zonal velocity at 1000 m depth in the L200-WIND and L200-edjIMFC model runs. The zonal velocity has been vertically filtered to contain only the baroclinic modes 15 to 22. Positive zonal velocity values indicate eastward velocity, negative values mean westward velocity.

since it depends on the choice of the vertical normal mode of the wave. However, the EDJ are composed of multiple normal modes rather than one distinct mode. Here one of the EDJ peak modes from L200-WIND is chosen (mode 19) just to give a visual impression of how much wider the observed EDJ are than the expected inviscid Rossby wave width (the grey dashed line compared to the black dashed line). The values for the Rossby wave width are a bit smaller here than usually obtained from observations of the Atlantic EDJ: Youngs and Johnson (2015), for example, estimated the Rossby wave width to be 0.73°, consistent with the lower vertical mode number 17 that they found for the Atlantic EDJ peak from observations.

As mentioned in Section 4.1 and visible in Figure 4.5, the Kelvin wave has a larger meridional scale than the first meridional mode Rossby wave. Since the EDJ are composed of the sum of both waves, the amplitude ratio might affect their meridional scale. The contribution of the Kelvin wave could also explain why the range of the mean EDJ widths is a bit shifted to larger values compared to the Rossby wave (1.5 times the Rossby wave) width. The widening of the real EDJ by a factor of 1.5 seems to happen independent of the amplitude ratio of Kelvin and Rossby wave, because Johnson and Zhang (2003) and Youngs and Johnson (2015) observed the widening by a factor of 1.5 when analysing only the first meridional mode Rossby wave part of the EDJ for all ocean basins. However, the influence of the two waves' amplitude ratio on the modelled meridional EDJ
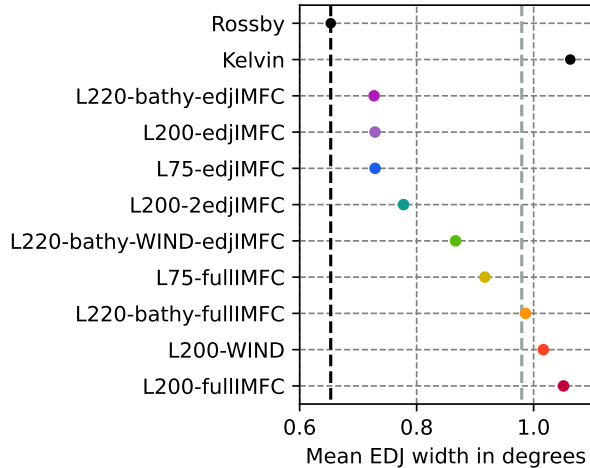
Figure 4.5: Mean cross-equatorial EDJ width in the different model experiments. For the nine model configurations that can simulate EDJ, the e-folding scale of a Gaussian fit to the time mean EDJ amplitude field is shown. The time mean EDJ amplitude field has been determined as the harmonic amplitude at the EDJ period (4.4 years) of the vertically filtered (modes 15 to 22) zonal velocity field from the models. Also shown are the corresponding meridional widths, also determined as the e-folding scale, of a Gaussian fit to the zonal velocity amplitude profile of an inviscid first meridional mode Rossby wave and an inviscid Kelvin wave for the EDJ peak baroclinic mode 19 from L200-WIND. The black dashed line marks the width of the Rossby wave, the grey dashed line is drawn at 1.5 times the width of the Rossby wave.

widths is investigated in Section 4.3.2, because it might explain part of the differences between the models.

In general, the mean meridional width of the EDJ is larger in those model configurations with wind forcing or fullIMFC forcing. In contrast to that, models with only edjIMFC forcing, i.e. IMFC forcing varying only at the interannual EDJ frequency, have the narrowest EDJ, although the doubling of the edjIMFC forcing in L200-2edjIMFC leads to a slight EDJ widening compared to L200-edjIMFC. Since variability on all other time scales is much reduced in the model runs forced only at the interannual EDJ frequency, the narrow EDJ in those models could be connected to a lack of variability, e.g. intraseasonal waves. This is investigated in Section 4.3.3, where also the contributions of meandering, and instantaneous widening, to the time mean widening of the EDJ are separated.

4.3.2 Contributions of Kelvin and first meridional mode Rossby wave to the EDJ basin mode

In Figure 4.6, a regression of the vertically filtered (containing only vertical modes 15 to 22) zonal velocity from L200-WIND on the zonal velocity signature of an analytic equatorial Kelvin and an analytic first meridional mode Rossby wave of vertical mode 19 at the EDJ frequency is shown. The meridional profiles of the two waves have been stretched meridionally before the regression for every model separately, to account for the different meridional widths of the EDJ. For more details see the methods section. It can be seen in Figure 4.6 that the Rossby wave has a much larger equatorial amplitude than the Kelvin wave in L200-WIND. This is consistent with observations of the Atlantic EDJ (Youngs and Johnson, 2015, Chapter 3). The phase fields of the waves are smooth

and correctly show westward propagation for the Rossby wave and eastward propagation for the Kelvin wave, which indicates that the separation of the two wave components by the regression seems to work well. Additionally, the phase difference between the two waves varies approximately linearly with longitude between $-\pi$ at one boundary and π at the other boundary for all models (not shown), consistent with the theoretical phase difference of the Kelvin and the first meridional mode Rossby wave in a resonant equatorial basin mode (Cane and Moore, 1981).
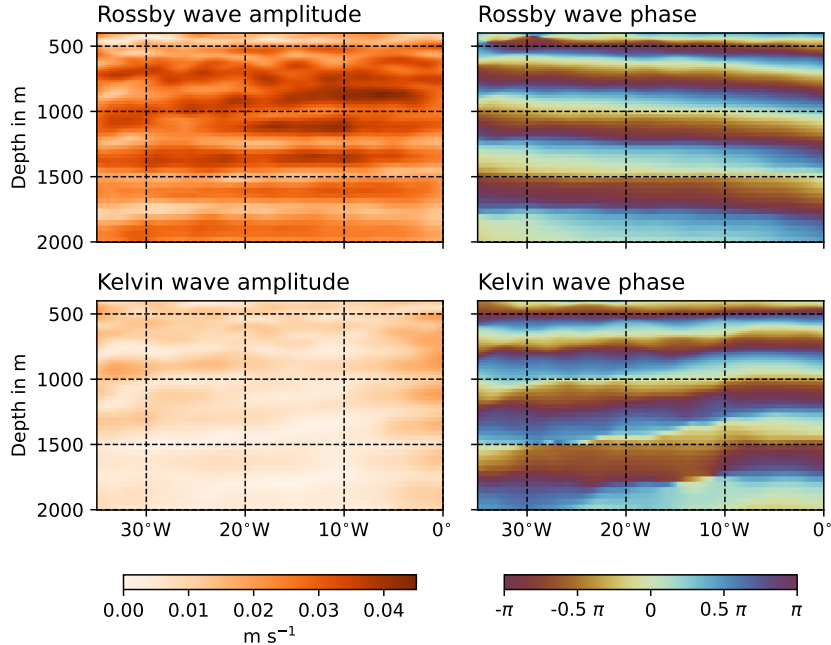

Figure 4.6: Regression of the vertically filtered (modes 15 to 22) zonal velocity from L200-WIND on the zonal velocity signature of an equatorial Kelvin and a first meridional mode Rossby wave of vertical mode 19 and the EDJ frequency. The amplitude shown on the left is the amplitude on the equator.

To quantify the ratio between the Kelvin and the first meridional mode Rossby wave amplitudes, the amplitude fields from the regression are averaged between 500 and 2000 m depth, and between 25°W and 15°W. The resulting equatorial amplitude values of the two waves are shown for each model in the left panel of Figure 4.7, together with the amplitude contributions of the Kelvin and first meridional mode Rossby wave to the real Atlantic EDJ basin mode at 1000 m depth as estimated from Argo float data in Chapter 3. In the centre panel, the amplitude ratio is shown. Again, the model configurations are sorted by the mean meridional width of their EDJ; no systematic relationship between the amplitude ratio and mean EDJ width is visible. In the right panel, the cross-equatorial width of a theoretical basin mode is shown, consisting of an equatorial Kelvin and a first meridional mode Rossby wave with the amplitude ratio shown in the centre panel and the phase difference derived by Cane and Moore (1981) but without any higher meridional mode Rossby waves. As expected, a larger relative contribution of the Kelvin wave (smaller ratio in the centre panel) leads to a wider EDJ basin mode, but the effect is very small for the ratios in the models and also the Atlantic EDJ Argo data. The differences in the Kelvin wave amplitude compared to the Rossby wave amplitude can thus be rejected as a possible explanation for the differences in the mean meridional EDJ width in the models.

There are a few interesting points to note here that are not related to the cross-equatorial width of
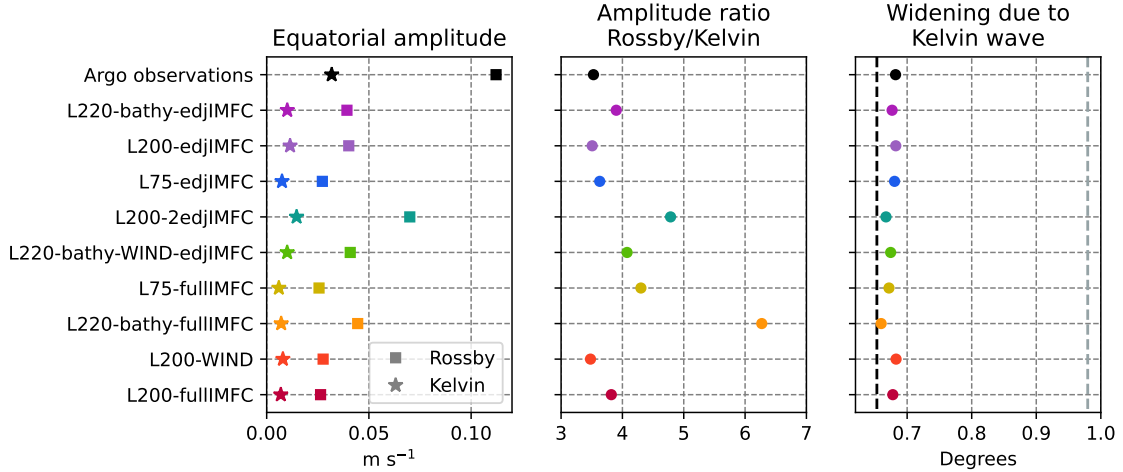
Figure 4.7: Amplitudes of equatorial Kelvin wave and first meridional Rossby wave contributions to the EDJ for each of the nine models with EDJ, as determined by a regression of the waves' zonal velocity signatures on the vertically filtered (modes 15 to 22) zonal velocity field from the models. The models are sorted by their mean EDJ width, from smallest to largest as in Figure 4.5. Also shown in black are the amplitudes of the waves in the real EDJ, as determined from Argo float data in Chapter 3. Shown in the right panel by the coloured markers is the cross-equatorial width of a theoretical basin mode with the amplitude ratio from the central panel, and with higher meridional mode Rossby waves neglected. Again, the width (width enhanced by 1.5) of the Rossby wave is marked by the dashed black line (dashed grey line).

the EDJ. In general, the EDJ in the models are much weaker than in the real Atlantic Ocean, as visible in the left panel of Figure 4.7. This has already been shown in Chapter 2 for L200-WIND and L200-edjIMFC, and one reason for this could be that the intraseasonal variability exciting and maintaining the EDJ (Chapter 2) is too weak in the model because of the steady or missing wind forcing and thus less instability in the upper ocean currents. This is shown in more detail in Section 4.3.3. However, the amplitude ratio of the Rossby and Kelvin wave is quite realistic in many of the models, although in a few the Rossby wave is even more dominant than in reality. It is intriguing that the models despite their high degree of idealisation correctly simulate the larger Rossby wave amplitude compared to the Kelvin wave amplitude, because this large ratio seems to be a peculiarity of the EDJ in the Atlantic Ocean: Youngs and Johnson (2015) report that in the Indian and Pacific Oceans the Kelvin and first meridional Rossby waves have similar amplitudes. Why the Rossby wave is favoured so much in the Atlantic ocean, is not clear. A possible reason would be differences in bathymetry between the oceans. Because the EDJ do not consist of one single vertical mode but several neighbouring vertical modes, they can propagate vertically. The energy propagates upward because the phase propagation is directed downward, and the upward energy beam of the first meridional Rossby wave component of the EDJ is steeper by a factor 3 than that of the Kelvin wave component (McCreary, 1984). Although the slopes are both small, this might lead to different interaction of the Kelvin wave with the bathymetry compared to the Rossby wave. In the models, the addition of realistic Atlantic bathymetry does indeed make the ratio of Rossby to Kelvin wave amplitude a little larger (see centre panel of Figure 4.7). However, this effect is small, and since also the flat-bottomed configurations simulate a much larger Rossby than Kelvin wave amplitude, the interaction with bathymetry cannot be the only reason for the dominance of the Rossby wave in the Atlantic.

4.3.3 Contributions of EDJ meandering and EDJ instantaneous width, connection to intraseasonal meridional velocity variability

According to the theory of Muench et al. (1994), the EDJ widening could be attributed to time averaging over meandering EDJ, where the meandering is caused by meridional advection by intraseasonal waves. Greatbatch et al. (2012), on the other hand, proposed that the EDJ are wider than an inviscid basin mode of corresponding vertical scale because of strong lateral mixing of momentum due to small scale velocity fluctuations associated with intraseasonal waves, compared to weak diapycnal mixing of density around the equator. In both cases, the meridional width of the EDJ should thus depend on the spectral power of the intraseasonal meridional velocity variability, although for the theory of Greatbatch et al. (2012) also other processes could play a role that contribute to enhanced lateral mixing of momentum. The strength of the intraseasonal variability at depth shows large differences across the nine model configurations that can simulate EDJ. In Figure 4.8, spectra of the meridional velocity at the equator and 23°W are shown for moored observations and two example model configurations, L200-WIND and L200-edjIMFC, which have relatively wide and narrow EDJ, respectively. It can be seen that the intraseasonal variability at depth is a bit too weak in L200-WIND compared to observations. One reason for this is probably the missing seasonal cycle in the model's wind forcing, because in reality the generation of intraseasonal waves in the tropical Atlantic Ocean is strongest in boreal summer when the shear instabilities between the surface currents intensify (e.g. von Schuckmann et al., 2008). In L200-WIND, this peak generation of intraseasonal variability is missing because of the steady forcing. Another difference is a shift of the maximum spectral power between 1000 and 2000 m depth towards longer periods of about 50 days in L200-WIND compared to 30-40 days in the moored observations. Nevertheless, L200-WIND shows, as the moored observations, significant spectral power of the intraseasonal meridional velocity variability on the equator, down to depths of at least 3000 m. In contrast to that, L200-edjIMFC shows very much reduced equatorial meridional velocity variability on all time scales, also in the intraseasonal period range between 30 and 90 days. This is due to the missing wind forcing in this model configuration. Still, there is an intraseasonal peak in the spectrum at a period of about 70 days.

The averaged spectral power of the equatorial intraseasonal meridional velocity variability is shown for each of the nine model configurations in Figure 4.9 (centre left panel). Again, the models are sorted by their mean meridional EDJ width, which is also shown in the left panel of the figure for comparison. The relationship between the mean EDJ width and the strength of the intraseasonal variability in the models is not obvious. Therefore, the contributions of meandering and instantaneous widening to the time mean EDJ width are calculated first, to then analyse their relationship with the strength of the intraseasonal variability separately.

To separate the reversible (meandering) and the irreversible (instantaneous widening) part of the EDJ widening in the model, a Gaussian bell curve is fitted to the vertically filtered (modes 15 to 22) zonal velocity at 1000 m depth, at every longitude between 25°W and 15°W and every point in time separately. The mean width due to meandering, as well as the instantaneous width are then estimated from the fit parameters as described in Section 4.2.2. In Figure 4.9, the resulting meridional widths for each of the nine model configurations are shown, in the centre right panel for meandering, and in the right panel for instantaneous widening. Again, the width (width enhanced by 1.5) of the Rossby wave is marked by the dashed black line (dashed grey line), to give an impression of what fraction of the observed mean EDJ widening can be achieved by the process in question. It can be seen that there are differences between the model configurations in how
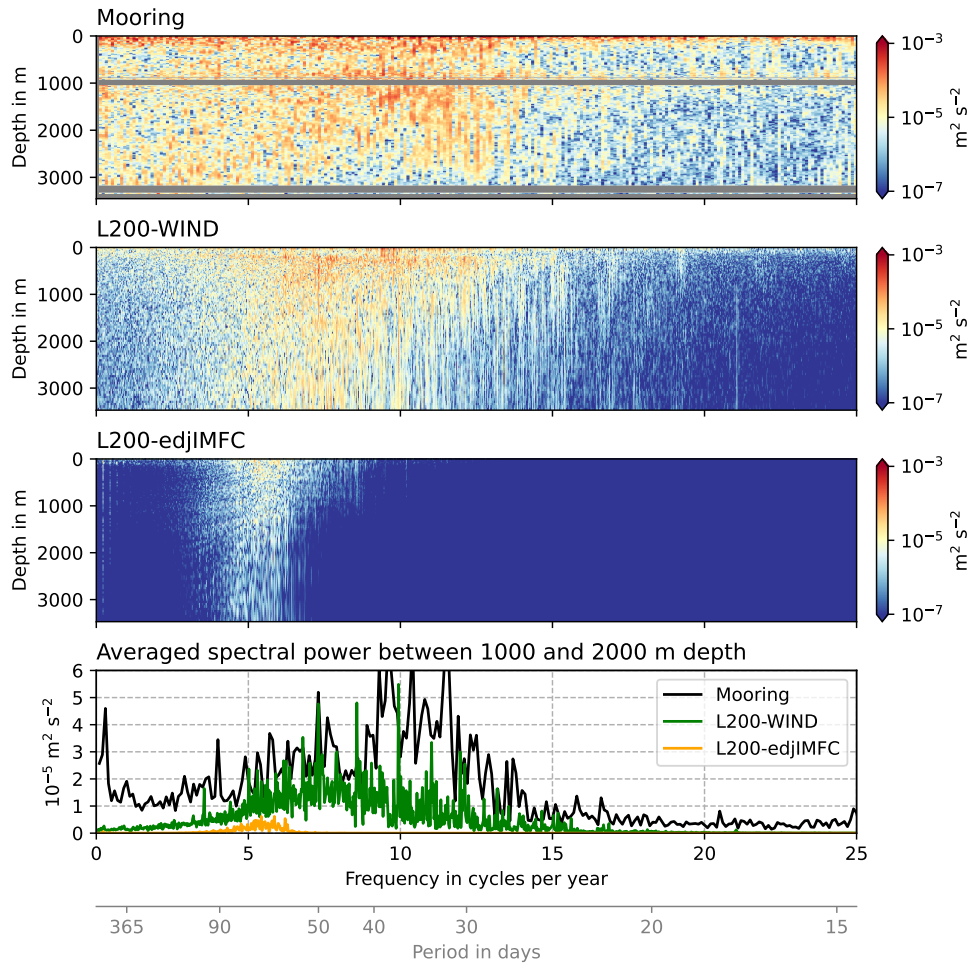
Figure 4.8: Comparison of power spectra of the meridional velocity in moored observations and two model runs, at 0°N, 23°W. The top panel has been updated and modified from Tuchen et al. (2018).

much the EDJ meander. Not surprisingly, the model runs with wind forcing or full IMFC forcing, which also have more intraseasonal variability, show more meandering of the EDJ. In the four model configurations with the largest mean EDJ widths, the meandering widens the EDJ in the time mean by about half the observed widening of factor 1.5, in L75-fullIMFC even more (this model stands out in that respect, as it is the only model in which the meandering contributes more to the time mean widening of the EDJ than the instantaneous width). Our model results thus suggest that meandering of the EDJ does play a role in widening the EDJ meridionally in the time mean. Also the instantaneous width of the EDJ is much larger in the model runs with wind forcing or full IMFC forcing, again consistent with the enhanced intraseasonal variability in those models (although here the relationship is not that clear, more details follow in the next paragraph). Except for L75-fullIMFC, the instantaneous widening explains a larger part of the observed EDJ widening than the meandering, with the instantaneous width of the EDJ in L200-WIND and L200-edjIMFC even reaching factor 1.5 compared to the theoretical Rossby wave scale.

As already mentioned, a clear relationship between the strength of the intraseasonal variability and the EDJ meandering can be seen in Figure 4.9, whereas for the instantaneous widening of the EDJ, the relationship to the strength of the intraseasonal variability in the model is less clear.
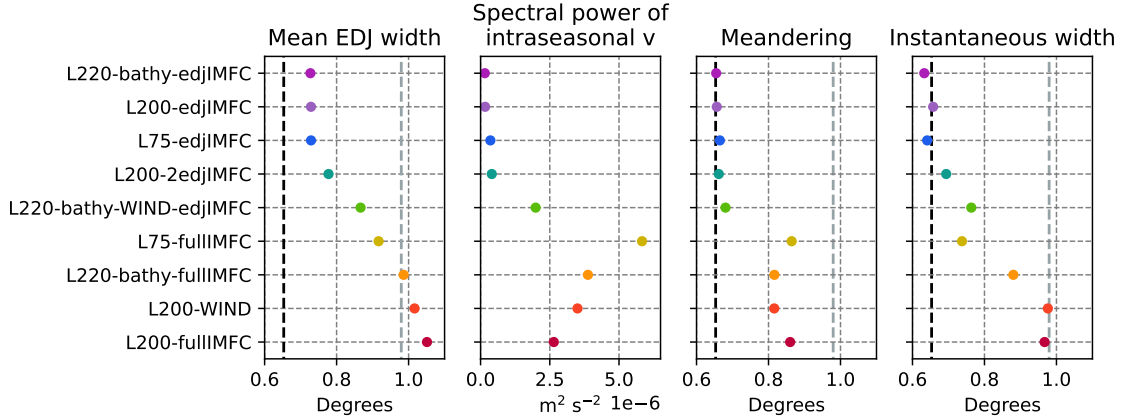
Figure 4.9: Contributions to mean meridional EDJ width by meandering and by instantaneous widening. Left panel: Mean meridional EDJ width, as shown in Figure 4.5. Centre left panel: Spectral power of the equatorial intraseasonal meridional velocity, averaged over periods of 30 to 90 days, between 400 and 2000 m depth and over all longitudes excluding 7.5° at the western and eastern boundary. Centre right panel: Time mean width of a theoretical Rossby wave meandering with the same distribution of velocity core shifts away from the equator as determined for the model in question. Right panel: Instantaneous meridional width of the EDJ. Again, the width (width enhanced by 1.5) of the Rossby wave is marked by the dashed black line (dashed grey line).

To investigate and quantify this, linear regressions of the mean width of the EDJ due to the two processes onto the averaged spectral power of the equatorial meridional velocity variability are shown in Figure 4.10. For both processes, there is a positive correlation between the meridional EDJ width and the strength of the intraseasonal variability. In the case of the EDJ meandering, the correlation is quite large, and the regression can explain 80% of the variance in mean EDJ width due to meandering. In contrast to that, only 35% of the variance in instantaneous EDJ width can be explained by the regression on the strength of the intraseasonal variability, which suggests that although there is a contribution by intraseasonal waves, also other processes must play a role in setting the enhanced cross-equatorial instantaneous EDJ width. According to the theory by Greatbatch et al. (2012), these could be all processes that lead to lateral mixing of momentum, i.e. cause a negative power input into the EDJ, which likely happens also on other scales than the intraseasonal time scale. As visible in the right panel of Figure 4.10, these processes also depend on the model configuration, e.g. the vertical resolution, which is not the case for the meandering. For the instantaneous width, it can be clearly seen that if the models are grouped into three groups; those that have a flat bottom and 200 levels, those that have bathymetry and 220 levels, and those that have a flat bottom and 75 levels (indicated by the three different colours); the resulting regression slope will be a different one and the explained variance will be much higher for each of the groups. Separate regressions are not computed here, however, because the number of data points in each group is too small to obtain a meaningful result.

4.4 Discussion

In this chapter, it could be shown that instantaneous widening of the cross-equatorial zonal velocity profile associated with the EDJ plays a larger role in setting the enhanced time mean meridional width of the EDJ than time averaging over meandering of the jets. It thus seems that the theory
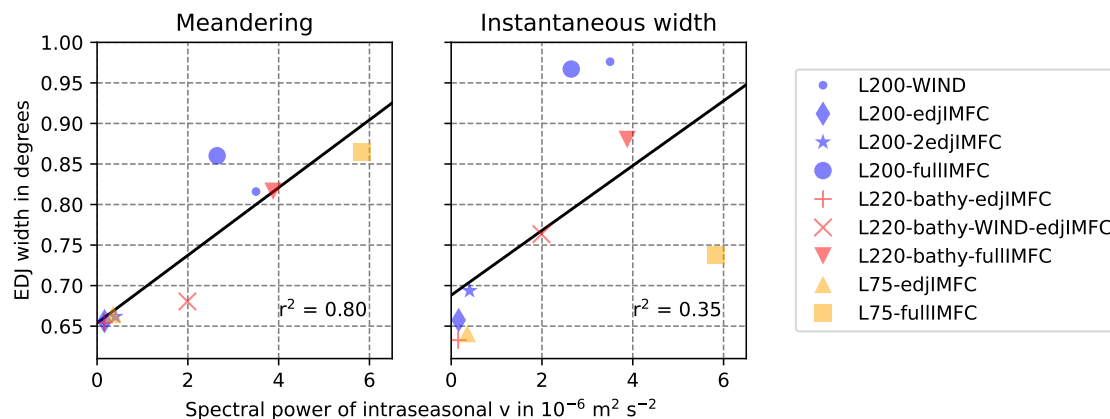
Figure 4.10: Relation between the strength of intraseasonal meridional velocity variability and the enhanced mean meridional width through meandering (left) or instantaneous widening (right) of the EDJ in the models. The spectral power of the equatorial meridional velocity has been averaged over all longitudes excluding 7.5° at the western and eastern boundary, between 400 and 2000 m depth and between periods of 30 and 90 days. Shown in black is a linear regression, with the squared correlation coefficient r^2 indicated in the lower right corner.

suggested by Greatbatch et al. (2012) which attributes the enhanced meridional EDJ width to large lateral mixing of momentum compared to small diapycnal mixing of density is quite important for the observed widening of the EDJ. Nevertheless, also meandering of the EDJ around the equator contributes a non-negligible part to the meridional widening of the EDJ time mean amplitude field, as suggested by Muench et al. (1994).

However, the results shown here are based only on idealised model simulations of the EDJ. The exact magnitude of the contributions of both suggested processes in the real ocean cannot be inferred from these model experiments, but it is possible to gain some insight by looking at instantaneous ship sections of the EDJ. In general, the width of the EDJ has been determined from observations by looking at time mean sections (e.g. Muench et al., 1994) or by spectral analysis which also gives a time mean width (e.g. Johnson and Zhang, 2003; Youngs and Johnson, 2015), such that it is not possible to distinguish between the reversible widening by meandering and irreversible instantaneous widening. By looking at instantaneous (i.e. measured in the course of a few days) zonal velocity sections, it should be possible to assess whether the real EDJ show both an enhanced instantaneous width and meandering as in the model results presented in this chapter.

In Figure 4.11, such an instantaneous zonal velocity section of the Atlantic EDJ is shown, measured in May 2003 as part of a cruise (171) with RV Sonne. Note that the first nine vertical modes have been removed, such that the EDJ are nicely visible. Looking at the five jets where it is possible to clearly see a core and a meridional extent (located at approximately 400 m, 600 m, 800 m, 1100 m and 1300 m depth), one can visually extract values for the maximum velocity and for a corresponding meridional e-folding scale of the jets. The instantaneous e-folding scale exceeds 1° for all of the five jets, which is much larger than the theoretically expected meridional scale of 0.65° to 0.85° for the Atlantic (Youngs and Johnson, 2015), and is close to the observed mean cross-equatorial width of the Atlantic EDJ of 1.08° (Youngs and Johnson, 2015). Also in observations, the instantaneous widening of the EDJ can thus explain a large part of the EDJ widening in the time mean, corroborating the theory by Greatbatch et al. (2012). The EDJ meandering is hard

to quantify from Figure 4.11, but some shifts of EDJ cores away from the equator can be seen. Most jets are centred on the equator, however. Similar instantaneous zonal velocity profiles of the Atlantic EDJ from different longitudes and times, measured during EQUALANT cruises in 1999 and 2000, are shown e.g. by Gouriou et al. (2001), Bourlès et al. (2003), and Bunge et al. (2006). They also show wider instantaneous EDJ, and only small shifts of the jet cores away from the equator. These observations support the conclusion that instantaneous widening, which can be explained by enhanced lateral or isopycnal mixing of momentum together with small diapycnal mixing of density (Greatbatch et al., 2012), plays the most important role in setting the enhanced mean cross-equatorial width of the Atlantic EDJ, whereas averaging over meandering of the jets as suggested by Muench et al. (1994) provides a smaller contribution to the enhanced mean EDJ width.
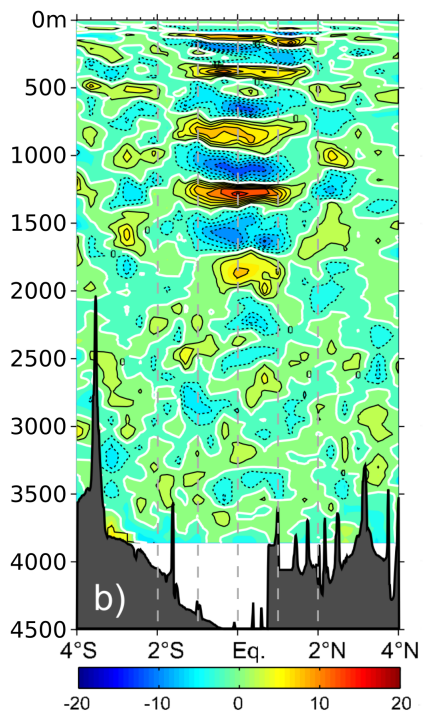

Figure 4.11: Instantaneous zonal velocity section at 35°W as observed in May 2003 during cruise 171 of the research vessel Sonne. The first nine vertical normal modes have been removed. The colour shading shows zonal velocity in $\mathrm{cm\,s^{-1}}$, the contour interval is $2\,\mathrm{cm\,s^{-1}}$. Positive values indicate eastward velocity, negative values westward velocity. Latitude grid lines have been added here for better visibility. *From Eden and Dengler (2008).*

Another interesting result from the model experiments shown here is the connection of the meridional EDJ widening to the strength of intraseasonal variability in the depth range of the EDJ. From the models, it can be concluded that the meandering of the EDJ is very likely largely due to meridional advection of the EDJ by intraseasonal waves, as suggested by Muench et al. (1994). A linear regression of the mean EDJ width due to meandering on the spectral power of the intraseasonal meridional velocity variability in the depth range of the EDJ yields an explained variance of 80%. This is different for the part of the mean EDJ widening that is due to instantaneous widening of the EDJ basin mode. Here, a regression on the spectral power of the intraseasonal variability also yields a positive correlation, but can explain only 35% of the variance. Although Greatbatch

et al. (2012) mention in particular intraseasonal meridional velocity fluctuations as a source for the enhanced lateral mixing of momentum away from the EDJ maximum, there are of course also other processes and variability on other time scales that cause lateral mixing of momentum. For example, the interaction of the EDJ with the Equatorial Undercurrent (EUC) is a source of momentum dissipation for the jets. Further research is necessary to identify and quantify the impact of this and other possible sources of momentum dissipation, for example by doing a kinetic energy budget analysis of all terms in the governing equations that cause negative power input into the EDJ from variability on any other temporal and spatial scales, similar e.g. to what Ascani et al. (2015) have done.

5 Maintenance of the central equatorial intermediate current system by intraseasonal momentum flux convergence

5.1 Introduction

As described in Chapter 1, the Equatorial Intermediate Current System (EICS) is located in the tropical Atlantic Ocean between approximately 500 and 2000 m depth. It consists of strong zonal currents that have a large vertical scale and are quasi-steady in time, in contrast to the EDJ. They alternate in direction with latitude and extend to more than 15°S/N. The central part of the EICS is composed of a mean westward flow on the equator (although in the eastern part of the basin this is reversed by the eastward mean flow that is generated nonlinearly by the EDJ as shown in Chapters 2 and 3), and flanking mean eastward currents at 2°S (South Intermediate Countercurrent, SICC) and 2°N (North Intermediate Countercurrent, NICC). It has been suggested by Hua et al. (2008) and Ascani et al. (2010) that this central part of the EICS is generated by the breaking and dissipation of intraseasonal Yanai waves.

In Chapter 2, it was shown that the intraseasonal momentum flux convergence (IMFC) that is associated with the deformation of intraseasonal waves by the slowly varying EDJ is enough to maintain EDJ with a reasonable amplitude in an idealised ocean model of the tropical Atlantic. This corroborates the theory by Greatbatch et al. (2018) that the EDJ can distort the intraseasonal waves, which are abundant in the equatorial Atlantic Ocean, in such a way that the resulting momentum flux convergence reinforces the jets. Greatbatch et al. (2018) compare this mechanism to the momentum flux into the atmospheric jet stream by distorted, so-called banana-shaped eddies. The theory by Greatbatch et al. (2018) does not only apply to the EDJ, though, but to all equatorial currents that have a smaller meridional scale and larger time scale than the intraseasonal waves. It could thus also be important for the maintenance of the central part of the EICS, a possibility which will be explored in this chapter with a similar experimental setup as that described in Chapter 2 for the EDJ.

In the following, the model setups used in this chapter will be described (Section 5.2), followed by the results in Section 5.3 and a short discussion in Section 5.4.

5.2 Model configurations

To investigate the importance of the IMFC for the time mean zonal flow in the deep equatorial Atlantic Ocean, a combination of idealised model configurations is used that have already been described in detail in Section 4.2. The configuration L200-WIND is again used as the basic model. Two additional model configurations, both with a flat bottom and with 200 vertical levels, are used in this chapter. One is forced only with the time mean component of the IMFC diagnosed from L200-WIND to determine the magnitude and effect of the momentum flux convergence associated with the interaction of the time mean zonal flow, i.e. the central EICS, with the intraseasonal waves; this configuration is called L200-meanIMFC. The other configuration used is L200-fullIMFC, which is forced by the full IMFC field varying on all time scales which of course also includes the time mean component of the IMFC. For more details, please see Section 4.2 and Table 4.1.

5.3 Results

To show which currents can be reproduced in the different model configurations, mean zonal velocity sections are shown from observations and from the three model runs at two different longitudes where sufficiently many ship sections are available. These are the regularly probed cross-equatorial sections at 23°W, shown in Figure 5.1, and closer to the western boundary at 35°W, shown in Figure 5.2. In L200-WIND, the surface and thermocline circulation up to 7°N includes the main features of the observed circulation, but the currents are too strong, especially the North Equatorial Countercurrent (NECC). The Equatorial Undercurrent (EUC) is additionally shifted to the south compared to observations. These differences in the near-surface circulation can likely be attributed to the many deficiencies of the idealised model simulation, including the missing variability in the wind forcing, the lack of bathymetry and coastlines, and the missing exchange of water masses through the northern and southern boundaries. However, as this thesis is concerned with the deeper zonal current systems of the tropical Atlantic, this is not of large importance here. Below 300 m, L200-WIND reproduces the central part of the Equatorial Intermediate Current System (EICS) which is the focus of this chapter. The currents that are simulated at realistic locations are the westward flow located on the equator (Equatorial Intermediate Current, EIC), the flanking eastward currents at approximately 2°S (South Intermediate Countercurrent, SICC) and 2°N (North Intermediate Countercurrent, NICC), and possibly also the westward currents between 3°S/N and 4°S/N. Further north, the currents simulated by L200-WIND are different from the observed currents (visible in Figure 5.1). The inability of the model to simulate the parts of the EICS that are further away from the equator is consistent with the theory that these currents are dynamically different from the central EICS and are generated by nonlinear triad interaction of annual Rossby waves (Qiu et al., 2013; Ménesguen et al., 2019), because there is no annual cycle in L200-WIND due to the steady wind forcing. The central part of the EICS that the model can simulate is too weak compared to observations in L200-WIND. One reason for this is probably that the intraseasonal variability is too weak in the model (see Section 4.3.3).

Interestingly, the subthermocline westward mean flow on the equator and the flanking eastward SICC and NICC are also reproduced in the other two model runs, which have no wind forcing but mean or full IMFC forcing. The amplitude of the westward flow on the equator and the SICC and NICC is larger in L200-meanIMFC than in L200-WIND, and even more so in L200-fullIMFC where the currents reach amplitudes that are very close to those from observations. This indicates that
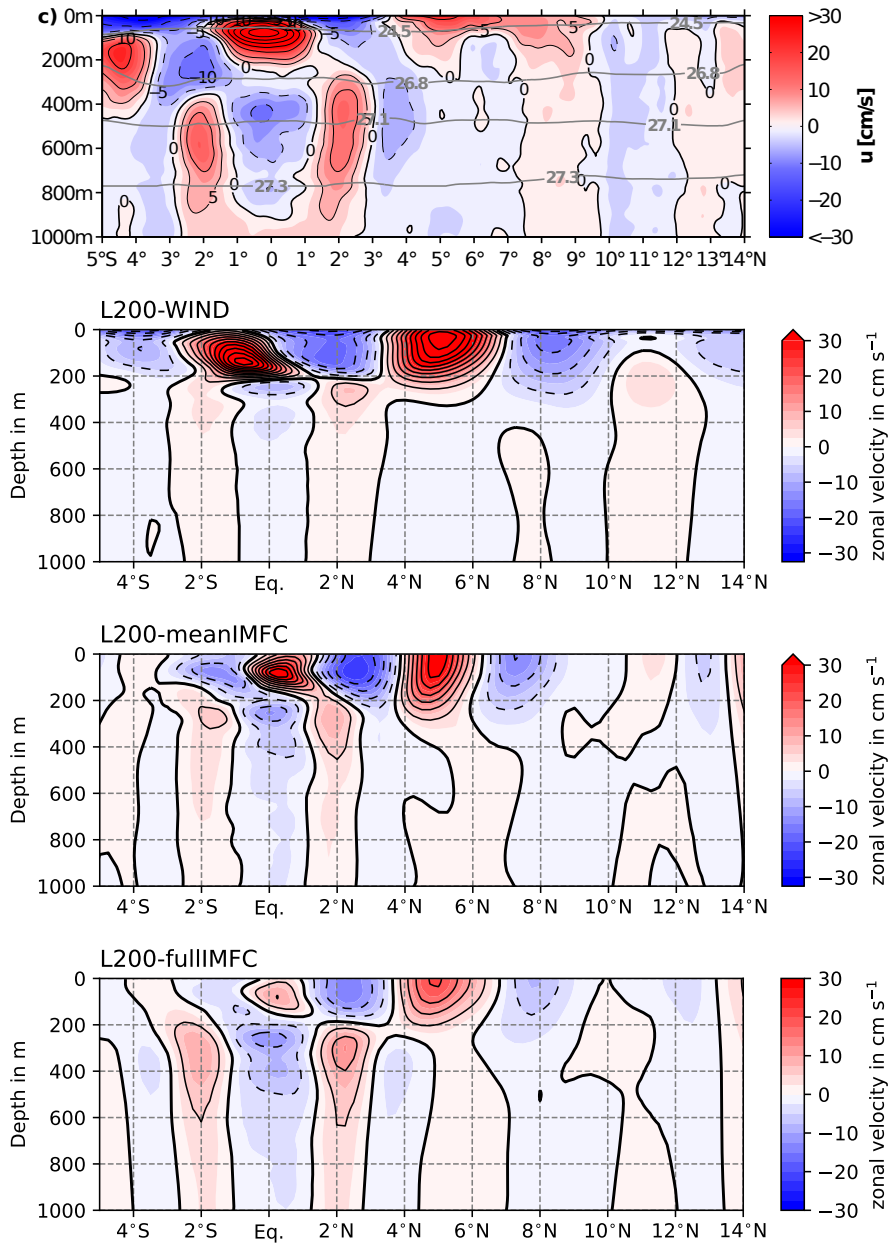
Figure 5.1: Top panel: observed mean zonal velocity section at 23°W *(from Brandt et al., 2015)*. Lower three panels: mean zonal velocity sections at 23°W in the L200-WIND, L200-meanIMFC and L200-fullIMFC model runs. In all panels, the contour interval for the colour shading is $2.5\,\mathrm{cm\,s^{-1}}$, for the black contours $5\,\mathrm{cm\,s^{-1}}$. Positive velocity values (red colours and solid lines) mean eastward velocity, negative values (blue colours and dashed lines) mean westward velocity.

the IMFC is important for the maintenance of the central EICS, as it is for the EDJ (cf. Chapter 2). That the amplitude of the central EICS is larger in L200-meanIMFC and L200-fullIMFC than in L200-WIND, although the IMFC forcing is diagnosed from the latter and hence should be present there as well, can likely be attributed to dissipative processes that are present in L200-WIND but not in the other two configurations because of the missing wind forcing.
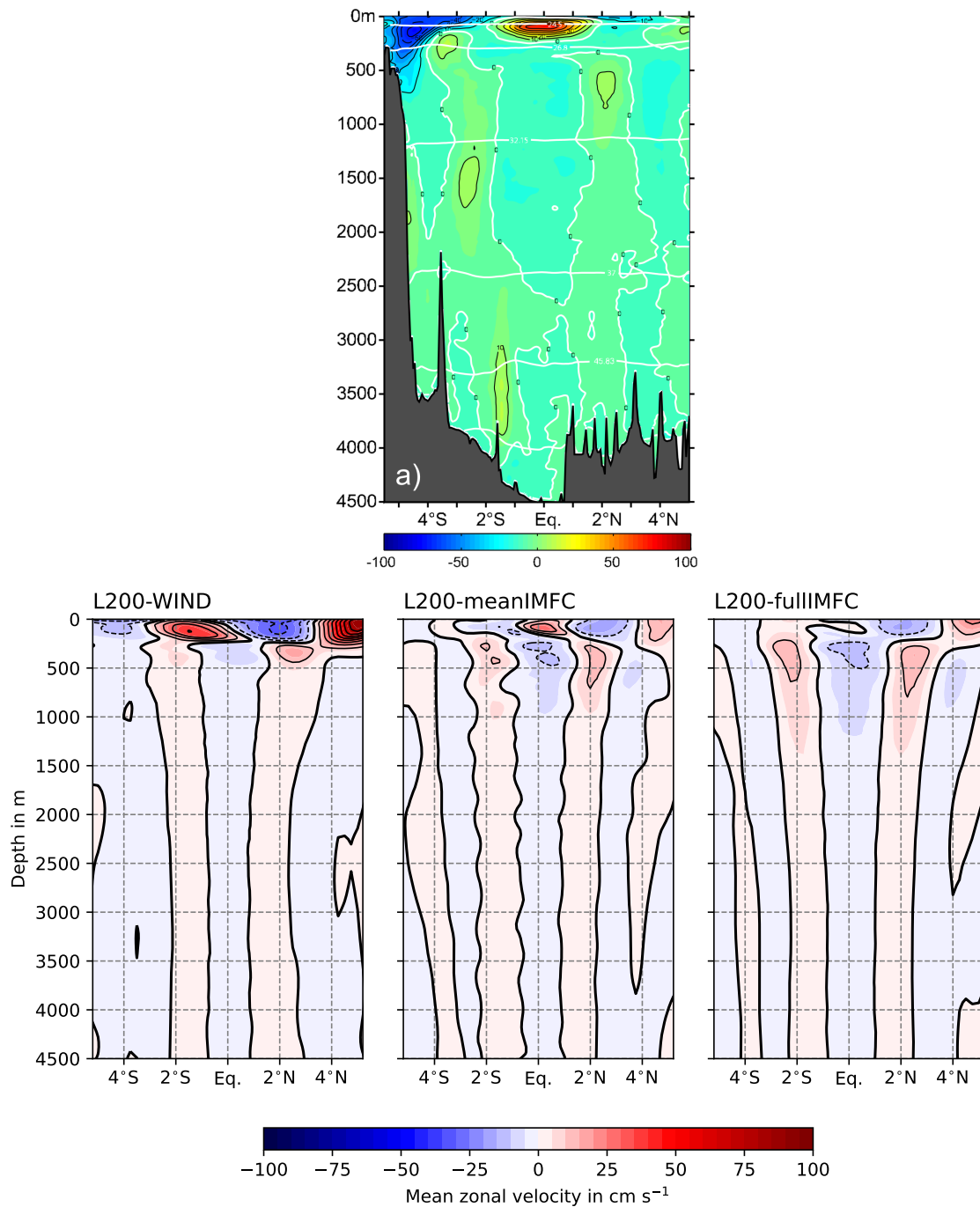
Figure 5.2: Top panel: observed mean zonal velocity section at 35°W, in cm s^{-1} *(from Eden and Dengler, 2008)*. Lower three panels: mean zonal velocity sections at 35°W in the L200-WIND, L200-meanIMFC and L200-fullIMFC model runs. In all panels, the contour interval for the colour shading is 2.5 cm s^{-1}, for the black contours 5 cm s^{-1}. Positive velocity values mean eastward velocity, negative values mean westward velocity.

5.4 Discussion

In this chapter it has been shown that intraseasonal momentum flux convergence possibly associated with the deformation of intraseasonal waves by the central EICS is sufficient to maintain the EICS in an idealised ocean model. The intraseasonal momentum flux convergence (IMFC) due

to the interaction of the EICS with intraseasonal waves is diagnosed from a model configuration forced by surface wind stress, in which both the central EICS and intraseasonal waves are present. In another model configuration that has this IMFC as the only forcing, westward flow on the equator and eastward flow at approximately 2°S/N develop again, with an amplitude exceeding that of the central EICS in the original wind-forced model configuration but very similar to the observed amplitude of the SICC, NICC and the deep mean westward flow on the equator.

Hua et al. (2008) and Ascani et al. (2010) showed that westward flow on the equator and flanking eastward flow can be generated by the destabilisation and dissipation of an intraseasonal Yanai wave beam propagating into the deep ocean. Parts of the power input into the central EICS through the breaking and dissipation of intraseasonal waves might also be contained in the IMFC term used here to force the models. Further research would be necessary to separate these processes from the deformation of intraseasonal waves by the mean currents leading to momentum flux convergence as suggested by Greatbatch et al. (2018). The results presented here nevertheless point to the large importance of the intraseasonal waves at depth in both exciting and maintaining the central part of the EICS.

6 Summary and outlook

This chapter summarises the main findings of this thesis and gives an outlook on the implications of the results as well as emerging open questions and possible directions of future research. As stated in the introduction, the scientific results of this thesis can be divided into five research questions that are answered in the following.

Is the momentum flux convergence that is associated with the deformation of intraseasonal waves by the EDJ enough to maintain them against dissipation?

It has long been noted that the Equatorial Deep Jets (EDJ) need, apart from an excitation mechanism, also a process that supplies them with energy directly at their depth to allow them to vertically propagate over several years and several of their vertical wavelengths in the presence of dissipation (e.g. Muench et al., 1994; Claus et al., 2016). Greatbatch et al. (2018) showed that there is a positive correlation between the Atlantic EDJ and the meridional convergence of the intraseasonal zonal momentum flux, suggesting that the momentum flux convergence arises because the EDJ distort intraseasonal waves. They propose that the deformation of intraseasonal waves by the EDJ could be the mechanism that maintains the EDJ at depth. In Chapter 2 of this thesis, it has been investigated whether the thus generated momentum flux convergence is enough to maintain EDJ with a reasonable amplitude. This research question has been answered with the help of a model experiment comprising two idealised model configurations of the tropical Atlantic Ocean, which differ only in their forcing. The first of the models is forced with surface wind stress and is able to simulate both EDJ and intraseasonal waves, such that the maintenance mechanism to be investigated can occur in the model. From this configuration, the intraseasonal momentum flux convergence (IMFC) associated with the EDJ, i.e. varying at their period of approximately 4.5 years, is diagnosed and put into the second model configuration as the only forcing term. It could then be shown that in the second model, EDJ again develop which have an amplitude and scales very similar to the EDJ in the wind-forced model. This result suggests that the IMFC plays an important role in maintaining the EDJ against dissipation, strongly corroborating the theory by Greatbatch et al. (2018).

In addition to showing that the IMFC associated with the deformation of intraseasonal waves by the EDJ is enough to maintain the jets, the model results also demonstrate that it is possible to include EDJ in an ocean model through a momentum forcing mimicking the maintenance mechanism. This is corroborated by additional model runs shown in Chapter 4, where the IMFC forcing has been successfully used to reproduce EDJ in a wind-forced model configuration with 75 vertical levels that is, without the IMFC forcing, not able to simulate EDJ. These results are a promising starting point for developing an EDJ parameterisation. As described in Chapter 1, the EDJ contribute to the equatorial ventilation of the eastern tropical Atlantic oxygen minimum zone (Brandt et al., 2008, 2012), and are furthermore suggested to drive interannual variation of the surface climate in the tropical Atlantic region (Brandt et al., 2011b). However, current ocean models generally have

problems to simulate the EDJ. If the representation of the EDJ in ocean models were improved through a parameterisation based on the EDJ maintenance mechanism suggested by Greatbatch et al. (2018), this could thus lead to an improved ability of models to simulate oxygen and nutrient distributions in the tropical ocean (cf. Getzlaff and Dietze, 2013; Dietze and Loeptien, 2013), as well as potentially improve seasonal to interannual prediction of the tropical Atlantic surface climate. The results presented in Chapter 2 show conceptually how such a parameterisation could be implemented in an ocean model. Additional sensitivity experiments with changes in vertical resolution and bathymetry have yielded that the amplitude and phase difference of the IMFC forcing and the resulting EDJ vary depending on the model parameters, such that they would need tuning for each model separately to result in realistic EDJ. What is also necessary for the implementation of such a parameterisation is an accurate estimation of the real EDJ scales, which has been provided for the Atlantic EDJ in Chapter 3 of this thesis (see summary section on third research question below). This should ideally be updated regularly for an EDJ parameterisation that is as realistic as possible.

How do the EDJ modify the time mean circulation around the equator, i.e. the central part of the EICS?

Ascani et al. (2015) suggested that energy transfer takes place not only from intraseasonal variability to the EDJ as confirmed in Chapter 2, but also from the EDJ to the time mean zonal currents at intermediate depth around the equator, i.e. the central part of the Equatorial Intermediate Current System (EICS). This has been investigated in detail in Chapter 2 using the idealised model configuration of the tropical Atlantic Ocean that is forced only with the IMFC varying at the 4.5-year period of the EDJ. Despite the forcing only varying at one specific frequency, variability also at other frequencies develops that is generated nonlinearly by the EDJ in the model. This includes time mean zonal flow around the equator. The pattern of the mean zonal currents that are generated nonlinearly by the EDJ resembles the central EICS in the western part of the basin, with westward time mean flow on the equator and flanking eastward mean flow to the north and south. However, this pattern changes sign in the centre and eastern part of the basin, such that there the mean zonal flow generated by the EDJ is eastward on the equator, and westward north and south of the equator. The mean flow generated by the EDJ thus acts to strengthen the central EICS in the western basin, but weakens or reverses it in the eastern basin. From an analysis of the time mean zonal velocity from Argo float data at 1000 m depth, it could be shown in Chapter 2 that the equatorial mean flow is indeed not westward throughout the basin, but becomes eastward in the central equatorial Atlantic and to the east, suggesting that the EDJ reverse the time mean current direction there. The term responsible for the energy transfer from the EDJ to the time mean zonal currents in the model is the zonal self-advection of the EDJ, consistent with the findings of Ascani et al. (2015). In Chapter 3, the acceleration of the mean zonal velocity due to this term has also been calculated from Atlantic Argo float observations at 1000 m depth, which corroborates the findings from the model regarding the pattern of how the EDJ modify the EICS, also showing westward acceleration on the equator in the western part of the basin and eastward acceleration of the mean flow on the equator in the central and eastern part of the basin.

This result might have implications for the equatorial Atlantic oxygen distribution, because it suggests that the EDJ not only contribute to the ventilation of the eastern tropical Atlantic oxygen minimum zone by advecting oxygen themselves, but also by generating equatorial eastward mean flow in the central and eastern parts of the basin. This emphasizes the necessity to include the

EDJ in ocean models to improve the simulation of the distribution of oxygen and nutrients in the tropical Atlantic.

What are the exact scales of the Atlantic EDJ?

Because of their vertical and temporal variability, as well as their location in the subthermocline ocean, measurements of the EDJ have been scarce and their scales not well quantified. In Chapter 3, a comprehensive new scale estimation of the Atlantic EDJ using the increasing amount of Argo float data has been presented. Argo floats do not directly measure velocity, but Lebedev et al. (2007) provide approximately 10-day mean velocity values at the Argo floats' so-called parking depth calculated from the positions of descent and ascent together with the time the float spent at depth. These data are most abundant at a depth of 1000 m, which is located well in the depth range of the EDJ. From these data at 1000 m depth, new estimates of the Atlantic EDJ period, amplitude, phase, zonal wavelength, meridional structure and the amplitude contributions of the Kelvin and Rossby wave components could be obtained. Because no information about the vertical structure of the EDJ could be gained from the Argo float displacement data by Lebedev et al. (2007) due to the few available parking depth values, a second dataset has been used for a new assessment of the vertical scale of the Atlantic EDJ. This second dataset consists of the hydrographic profiles measured by the Argo floats during their descent and/or ascent. From this, information about the vertical structure of the EDJ can be extracted due to the fact that the EDJ are approximately in geostrophic balance.

The period of the Atlantic EDJ has been among the best-known parameters due to the availability of long-term moored velocity measurements from 23°W (e.g. Brandt et al., 2011b; Claus et al., 2016; Greatbatch et al., 2018), and the new estimate of the Atlantic EDJ period from Argo float data presented here (4.60 years, with a 95% confidence interval between 4.56 and 4.64 years) fits well to the earlier estimates. The new Atlantic EDJ amplitude and phase estimates from the Argo float data at 1000 m depth from Chapter 3 of this thesis, however, represent the first detailed assessment of the EDJs' basin-wide horizontal structure. It is consistent with the interpretation of the EDJ as a resonant equatorial basin mode of a high baroclinic mode, with a (harmonic) amplitude maximum of about $11\,\mathrm{cm\,s^{-1}}$ approximately in the centre of the basin (though a little shifted to the west) and decreasing amplitude towards the west and east. The amplitude field is narrower in the centre of the basin than towards the western and eastern boundaries, which indicates Rossby wave focussing due to β-dispersion (Schopf et al., 1981). From the phase field, westward propagation on the equator with a zonal wavelength of 146.7° (with a 95% confidence interval between 126.3° and 177.4°) can be detected, which is between the zonal wavelengths of an equatorial Kelvin wave and a first meridional mode Rossby wave for the particular vertical mode and frequency of the EDJ which are the two dominant components of an equatorial basin mode (Cane and Moore, 1981). The estimate of the zonal wavelength of the Atlantic EDJ confirms the prediction by Claus et al. (2016) from a shallow water model. The meridional structure of the Atlantic EDJ estimated from Argo float displacement data at 1000 m depth resembles that of a first meridional mode Rossby wave of a corresponding vertical normal mode, but widened meridionally by a factor of 1.5. This confirms earlier estimates of the Atlantic EDJs' meridional structure (Johnson and Zhang, 2003; Youngs and Johnson, 2015). However, in accordance with their dynamical explanation as a resonant equatorial basin mode, also a contribution of the equatorial Kelvin wave to the EDJ could be detected. Nevertheless, its equatorial amplitude ($3.18\,\mathrm{cm\,s^{-1}}$) is much smaller than that of the first meridional mode Rossby wave ($11.22\,\mathrm{cm\,s^{-1}}$). This dominance of the Rossby wave

component compared to the Kelvin wave component has also been found by Youngs and Johnson (2015) for the Atlantic EDJ, but curiously not for the Indian Ocean and Pacific EDJ where the two waves seem to have similar amplitudes. The new estimates of the vertical wavelength of the Atlantic EDJ do not show a longitudinal dependence. Since they are quite noisy because they are based on an equatorial geostrophic reconstruction of the zonal velocity from the density field, it is thus suggested to rather rely on estimates of the vertical EDJ scale from the direct velocity measurements from the mooring at 23°W. However, it could be shown from the reconstructed velocity data that the EDJ deepen towards the east, as already suggested by Schmid et al. (2005), by about 80 stretched decibar or a sixth of their vertical wavelength between 40°W and 0°E.

As already described in the above section on the first research question, this new scale estimation of the Atlantic EDJ could be used to develop a parameterisation of the EDJ for ocean models. Since the Argo program is continuously running, the EDJ scale analysis should then be regularly updated to get (a) improved estimates of all parameters due to more available data, and (b) an always up-to-date estimate of the EDJ phase, which is of course essential to get right in the model for assessing the EDJs' potential to improve seasonal to interannual predictions.

Is the enhanced meridional width of the EDJ due to averaging over meandering jets, or a widening through enhanced momentum dissipation?

As described in the introduction, observations of the EDJ have shown that their time mean cross-equatorial width is larger by a factor of 1.5 than theoretically expected. Muench et al. (1994) suggested that this might be caused by time averaging over jets that meander due to meridional advection by intraseasonal waves, whereas Greatbatch et al. (2012) showed that the EDJ could also be widened by an enhanced lateral mixing of momentum combined with small diapycnal mixing of density in the tropical oceans. Greatbatch et al. (2012) noted that the first theory describes a reversible process, unlike the process suggested by themselves which is irreversible. In Chapter 4, the contributions of the two suggested processes to the mean meridional width of the EDJ have been investigated using different idealised models of the tropical Atlantic. The model configurations differ in their forcing, which is composed of surface wind stress forcing and/or zonal momentum forcing in the entire water column that is derived from the meridional convergence of intraseasonal zonal momentum in the base model. There are also differences in the vertical resolution between the models, as well as in the representation of bathymetry. Because the mean cross-equatorial width of the EDJ varies across the model configurations, it is possible to investigate the processes leading to those EDJ width differences. It has been shown that instantaneous meridional widening of the EDJ, as it would be induced by enhanced lateral mixing of momentum, is responsible for a larger contribution to the mean meridional EDJ width than meandering of the EDJ in the models, but that meandering nevertheless also contributes to the time mean EDJ widening. This could be corroborated for the real Atlantic EDJ by looking at shipboard instantaneous (i.e. measured in the course of a few days) zonal velocity sections (Gouriou et al., 2001; Bourlès et al., 2003; Bunge et al., 2006; Eden and Dengler, 2008), which are a bit noisy but generally show an enhanced instantaneous cross-equatorial width of the EDJ approaching the observed time mean EDJ width, and shifts of the jet core away from the equator in only a few cases.

Concerning the origin of the EDJ meandering in the models, it could be shown that a large fraction (80%) of the variance in mean EDJ width due to meandering is explained by the differences in the strength of intraseasonal variability in the models. It thus seems likely that the EDJ meandering

is mostly due to meridional advection by intraseasonal waves, as suggested by Muench et al. (1994). For the instantaneous widening of the EDJ, a positive correlation with the strength of the intraseasonal variability has been found as well, consistent with Greatbatch et al. (2012) mentioning intraseasonal meridional velocity fluctuations as a possible source for the enhanced lateral mixing of momentum. However, the variations of the power of intraseasonal variability can only explain 35% of the variance in instantaneous EDJ widening, much less than for the meandering. This suggests that also other processes and variability on other time scales are important for causing enhanced lateral mixing of momentum in the equatorial Atlantic, e.g. the interaction of the EDJ with the Equatorial Undercurrent (EUC). Further research is necessary to identify and quantify the sources of momentum dissipation that lead to widening of the EDJ, for example by doing a kinetic energy budget analysis of all terms in the governing equations that cause negative power input into the EDJ from variability on any other temporal and spatial scales.

Does meridional momentum flux convergence due to the deformation of intraseasonal waves also maintain the central part of the EICS?

Greatbatch et al. (2018) suggested that all equatorial currents can be maintained through the deformation of intraseasonal waves and the accompanying momentum flux convergence, as long as the currents in question have a smaller meridional scale and a larger time scale than the intraseasonal waves. The mechanism is thus not only important for the maintenance of the EDJ, as shown in Chapter 2, but could also play a role for energy flux into the central part of the Equatorial Intermediate Current System (EICS), consisting of a time mean westward flow on the equator and mean eastward flow at 2°S/N (South/North Intermediate Countercurrent, SICC/NICC). In Chapter 5 it has been investigated whether this is the case, using a similar model experiment setup as for the EDJ in Chapter 2. Again, one model configuration is forced by surface wind stress, and in this model both the central EICS and intraseasonal waves are present such that the deformation mechanism can take place. From the wind-forced model, the IMFC is diagnosed and put into a different model configuration as the only forcing term. It could be shown that also the central EICS can be reproduced with only the IMFC forcing, which suggests that the momentum flux convergence due to deformation of intraseasonal waves proposed by Greatbatch et al. (2018) also maintains the westward mean flow on the equator and the flanking mean eastward SICC and NICC.

Like the EDJ, the SICC and NICC have been shown to ventilate the eastern tropical Atlantic oxygen minimum zone (Brandt et al., 2008, 2015), and their insufficient representation in biogeochemical ocean models has been suggested to lead to errors in the simulated oxygen and nutrient distributions (Getzlaff and Dietze, 2013; Dietze and Loeptien, 2013). The connection to the intraseasonal momentum flux convergence should be looked into for improved modelling also of the central part of the EICS, not only the EDJ as suggested before.

References

Argo, 2020: Argo float data and metadata from Global Data Assembly Centre (Argo GDAC). Tech. rep., https://doi.org/10.17882/42182.

Argo data management team, 2019: Argo User's Manual. Tech. rep., https://doi.org/10.13155/29825.

Ascani, F., Wang, D., Moore, D. W., Firing, E., and McCreary, J. P., 2004: Comments on "A Theory of Equatorial Deep Jets". *Journal of Physical Oceanography*, 34, 1781–1790, https://doi.org/10.1175/1520-0485(2004)034<1781:coatoe>2.0.co;2.

Ascani, F., Firing, E., Dutrieux, P., McCreary, J. P., and Ishida, A., 2010: Deep Equatorial Ocean Circulation Induced by a Forced–Dissipated Yanai Beam. *Journal of Physical Oceanography*, 40, 1118–1142, https://doi.org/10.1175/2010JPO4356.1.

Ascani, F., Firing, E., McCreary, J. P., Brandt, P., and Greatbatch, R. J., 2015: The Deep Equatorial Ocean Circulation in Wind-Forced Numerical Solutions. *Journal of Physical Oceanography*, 45, 1709–1734, https://doi.org/10.1175/JPO-D-14-0171.1.

Bastin, S., Claus, M., Brandt, P., and Greatbatch, R. J.: Atlantic equatorial deep jets in Argo float data. *Submitted to: Journal of Physical Oceanography*.

Bastin, S., Claus, M., Brandt, P., and Greatbatch, R. J., 2020: Equatorial Deep Jets and Their Influence on the Mean Equatorial Circulation in an Idealized Ocean Model Forced by Intraseasonal Momentum Flux Convergence. *Geophysical Research Letters*, 47, https://doi.org/10.1029/2020gl087808.

Behera, S., Brandt, P., and Reverdin, G., 2013: The Tropical Ocean Circulation and Dynamics. In: Ocean Circulation & Climate, edited by Siedler, G., Griffies, S. M., Gould, J., and Church, J. A., chap. 15, pp. 385–412, Academic Press, https://doi.org/10.1016/B978-0-12-391851-2.00015-5.

Bourlès, B., Andrié, C., Gouriou, Y., Eldin, G., du Penhoat, Y., Freudenthal, S., Dewitte, B., Gallois, F., Chuchla, R., Baurand, F., Aman, A., and Kouadio, G., 2003: The deep currents in the Eastern Equatorial Atlantic Ocean. *Geophysical Research Letters*, 30, https://doi.org/10.1029/2002gl015095.

Brandt, P., Schott, F. A., Provost, C., Kartavtseff, A., Hormann, V., Bourlès, B., and Fischer, J., 2006: Circulation in the central equatorial Atlantic: Mean and intraseasonal to seasonal variability. *Geophysical Research Letters*, 33, https://doi.org/10.1029/2005gl025498.

Brandt, P., Hormann, V., Bourlès, B., Fischer, J., Schott, F. A., Stramma, L., and Dengler, M., 2008: Oxygen tongues and zonal currents in the equatorial Atlantic. *Journal of Geophysical Research*, 113, https://doi.org/10.1029/2007jc004435.

Brandt, P., Caniaux, G., Bourlès, B., Lazar, A., Dengler, M., Funk, A., Hormann, V., Giordani, H., and Marin, F., 2011a: Equatorial upper-ocean dynamics and their interaction with the West African monsoon. *Atmospheric Science Letters*, 12, 24–30, https://doi.org/10.1002/asl.287.

Brandt, P., Funk, A., Hormann, V., Dengler, M., Greatbatch, R. J., and Toole, J. M., 2011b: Interannual atmospheric variability forced by the deep equatorial Atlantic Ocean. *Nature*, 473, 497–500, https://doi.org/10.1038/nature10013.

Brandt, P., Greatbatch, R. J., Claus, M., Didwischus, S.-H., Hormann, V., Funk, A., Hahn, J., Krahmann, G., Fischer, J., and Körtzinger, A., 2012: Ventilation of the equatorial Atlantic by the equatorial deep jets. *Journal of Geophysical Research: Oceans*, 117, https://doi.org/10.1029/2012jc008118.

Brandt, P., Bange, H. W., Banyte, D., Dengler, M., Didwischus, S.-H., Fischer, T., Greatbatch, R. J., Hahn, J., Kanzow, T., Karstensen, J., Körtzinger, A., Krahmann, G., Schmidtko, S., Stramma, L., Tanhua, T., and Visbeck, M., 2015: On the role of circulation and mixing in the ventilation of oxygen minimum zones with a focus on the eastern tropical North Atlantic. *Biogeosciences*, 12, 489–512, https://doi.org/10.5194/bg-12-489-2015.

Brandt, P., Claus, M., Greatbatch, R. J., Kopte, R., Toole, J. M., Johns, W. E., and Böning, C. W., 2016: Annual and Semiannual Cycle of Equatorial Atlantic Circulation Associated with Basin-Mode Resonance. *Journal of Physical Oceanography*, 46, 3011–3029, https://doi.org/10.1175/jpo-d-15-0248.1.

Brandt, P., Hahn, J., Schmidtko, S., Tuchen, F. P., Kopte, R., Kiko, R., Bourlès, B., Czeschel, R., and Dengler, M., 2021: Atlantic Equatorial Undercurrent intensification counteracts warming-induced deoxygenation. *Nature Geoscience*, 14, 278–282, https://doi.org/10.1038/s41561-021-00716-1.

Bunge, L., Provost, C., Lilly, J. M., d'Orgeville, M., Kartavtseff, A., and Melice, J.-L., 2006: Variability of the Horizontal Velocity Structure in the Upper 1600 m of the Water Column on the Equator at 10°W. *Journal of Physical Oceanography*, 36, 1287–1304, https://doi.org/10.1175/jpo2908.1.

Bunge, L., Provost, C., Hua, B. L., and Kartavtseff, A., 2008: Variability at Intermediate Depths at the Equator in the Atlantic Ocean in 2000–06: Annual Cycle, Equatorial Deep Jets, and Intraseasonal Meridional Velocity Fluctuations. *Journal of Physical Oceanography*, 38, 1794–1806, https://doi.org/10.1175/2008jpo3781.1.

Cane, M. A. and Moore, D. W., 1981: A Note on Low-Frequency Equatorial Basin Modes. *Journal of Physical Oceanography*, 11, 1578–1584, https://doi.org/10.1175/1520-0485(1981)011<1578:anolfe>2.0.co;2.

Cane, M. A. and Sarachik, E. S., 1977: Forced baroclinic ocean motions: II. The linear equatorial bounded case. *Journal of Marine Research*, 35, 395–432.

Claus, M., Greatbatch, R. J., and Brandt, P., 2014: Influence of the Barotropic Mean Flow on the Width and the Structure of the Atlantic Equatorial Deep Jets. *Journal of Physical Oceanography*, 44, 2485–2497, https://doi.org/10.1175/jpo-d-14-0056.1.

Claus, M., Greatbatch, R. J., Brandt, P., and Toole, J. M., 2016: Forcing of the Atlantic Equatorial Deep Jets Derived from Observations. *Journal of Physical Oceanography*, 46, 3549–3562, https://doi.org/10.1175/jpo-d-16-0140.1.

Crameri, F., Shephard, G. E., and Heron, P. J., 2020: The misuse of colour in science communication. *Nature Communications*, 11, https://doi.org/10.1038/s41467-020-19160-7.

Cravatte, S., Kessler, W. S., and Marin, F., 2012: Intermediate Zonal Jets in the Tropical Pacific Ocean Observed by Argo Floats. *Journal of Physical Oceanography*, 42, 1475–1485, https://doi.org/10.1175/jpo-d-11-0206.1.

Cravatte, S., Kestenare, E., Marin, F., Dutrieux, P., and Firing, E., 2017: Subthermocline and Intermediate Zonal Currents in the Tropical Pacific Ocean: Paths and Vertical Structure. *Journal of Physical Oceanography*, 47, 2305–2324, https://doi.org/10.1175/jpo-d-17-0043.1.

Delpech, A., Cravatte, S., Marin, F., Morel, Y., Gronchi, E., and Kestenare, E., 2020: Observed Tracer Fields Structuration by Middepth Zonal Jets in the Tropical Pacific. *Journal of Physical Oceanography*, 50, 281–304, https://doi.org/10.1175/jpo-d-19-0132.1.

Delpech, A., Ménesguen, C., Morel, Y., Thomas, L. N., Marin, F., Cravatte, S., and Gentil, S. L., 2021: Intra-Annual Rossby Waves Destabilization as a Potential Driver of Low-Latitude Zonal Jets: Barotropic Dynamics. *Journal of Physical Oceanography*, 51, 365–384, https://doi.org/10.1175/jpo-d-20-0180.1.

Dengler, M. and Quadfasel, D., 2002: Equatorial Deep Jets and Abyssal Mixing in the Indian Ocean. *Journal of Physical Oceanography*, 32, 1165–1180, https://doi.org/10.1175/1520-0485(2002)032<1165:edjaam>2.0.co;2.

Dietze, H. and Loeptien, U., 2013: Revisiting "nutrient trapping" in global coupled biogeochemical ocean circulation models. *Global Biogeochemical Cycles*, 27, 265–284, https://doi.org/10.1002/gbc.20029.

d'Orgeville, M., Hua, B. L., and Sasaki, H., 2007: Equatorial deep jets triggered by a large vertical scale variability within the western boundary layer. *Journal of Marine Research*, 65, 1–25, https://doi.org/10.1357/002224007780388720.

Edelson, R. A. and Krolik, J. H., 1988: The discrete correlation function - A new method for analyzing unevenly sampled variability data. *The Astrophysical Journal*, 333, 646–659, https://doi.org/10.1086/166773.

Eden, C. and Dengler, M., 2008: Stacked jets in the deep equatorial Atlantic Ocean. *Journal of Geophysical Research*, 113, https://doi.org/10.1029/2007jc004298.

Efron, B., 1979: Bootstrap Methods: Another Look at the Jackknife. *The Annals of Statistics*, 7, 1–26.

Eriksen, C. C., 1981: Deep Currents and Their Interpretation as Equatorial Waves in the Western Pacific Ocean. *Journal of Physical Oceanography*, 11, 48–70, https://doi.org/10.1175/1520-0485(1981)011<0048:dcatia>2.0.co;2.

Eriksen, C. C., 1982: Geostrophic equatorial deep jets. *Journal of Marine Research*, 40, 143–156.

Firing, E., 1987: Deep zonal currents in the central equatorial Pacific. *Journal of Marine Research*, 45, 791–812, https://doi.org/10.1357/002224087788327163.

Getzlaff, J. and Dietze, H., 2013: Effects of increased isopycnal diffusivity mimicking the unresolved equatorial intermediate current system in an earth system climate model. *Geophysical Research Letters*, 40, 2166–2170, https://doi.org/10.1002/grl.50419.

Gill, A. E., 1982: Atmosphere-Ocean Dynamics. Academic Press, International Geophysics Series Volume 30.

Gouriou, Y., Bourlès, B., Mercier, H., and Chuchla, R., 1999: Deep jets in the equatorial Atlantic Ocean. *Journal of Geophysical Research: Oceans*, 104, 21 217–21 226, https://doi.org/10.1029/1999jc900057.

Gouriou, Y., Andrié, C., Bourlès, B., Freudenthal, S., Arnault, S., Aman, A., Eldin, G., du Penhoat, Y., Baurand, F., Gallois, F., and Chuchla, R., 2001: Deep circulation in the equatorial Atlantic Ocean. *Geophysical Research Letters*, 28, 819–822, https://doi.org/10.1029/2000gl012326.

Greatbatch, R. J., Brandt, P., Claus, M., Didwischus, S.-H., and Fu, Y., 2012: On the Width of the Equatorial Deep Jets. *Journal of Physical Oceanography*, 42, 1729–1740, https://doi.org/10.1175/jpo-d-11-0238.1.

Greatbatch, R. J., Claus, M., Brandt, P., Matthießen, J.-D., Tuchen, F. P., Ascani, F., Dengler, M., Toole, J., Roth, C., and Farrar, J. T., 2018: Evidence for the Maintenance of Slowly Varying Equatorial Currents by Intraseasonal Variability. *Geophysical Research Letters*, 45, 1923–1929, https://doi.org/10.1002/2017gl076662.

Gregg, M. C., Sanford, T. B., and Winkel, D. P., 2003: Reduced mixing from the breaking of internal waves in equatorial waters. *Nature*, 422, 513–515, https://doi.org/10.1038/nature01507.

Grodsky, S. A., Carton, J. A., Provost, C., Servain, J., Lorenzzetti, J. A., and McPhaden, M. J., 2005: Tropical instability waves at 0°N, 23°W in the Atlantic: A case study using Pilot Research Moored Array in the Tropical Atlantic (PIRATA) mooring data. *Journal of Geophysical Research*, 110, https://doi.org/10.1029/2005jc002941.

Hahn, J., Brandt, P., Greatbatch, R. J., Krahmann, G., and Körtzinger, A., 2014: Oxygen variance and meridional oxygen supply in the Tropical North East Atlantic oxygen minimum zone. *Climate Dynamics*, 43, 2999–3024, https://doi.org/10.1007/s00382-014-2065-0.

Hayes, S. P. and Milburn, H. B., 1980: On the Vertical Structure of Velocity in the Eastern Equatorial Pacific. *Journal of Physical Oceanography*, 10, 633–635, https://doi.org/10.1175/1520-0485(1980)010<0633:otvsov>2.0.co;2.

Hua, B. L., d'Orgeville, M., Fruman, M. D., Ménesguen, C., Schopp, R., Klein, P., and Sasaki, H., 2008: Destabilization of mixed Rossby gravity waves and the formation of equatorial zonal jets. *Journal of Fluid Mechanics*, 610, 311–341, https://doi.org/10.1017/s0022112008002656.

Hummels, R., Dengler, M., Brandt, P., and Schlundt, M., 2014: Diapycnal heat flux and mixed layer heat budget within the Atlantic Cold Tongue. *Climate Dynamics*, 43, 3179–3199, https://doi.org/10.1007/s00382-014-2339-6.

Hunter, J. D., 2007: Matplotlib: A 2D Graphics Environment. *Computing in Science & Engineering*, 9, 90–95, https://doi.org/10.1109/mcse.2007.55.

Jayne, S., , Roemmich, D., Zilberman, N., Riser, S., Johnson, K., Johnson, G., and Piotrowicz, S., 2017: The Argo Program: Present and Future. *Oceanography*, 30, 18–28, https://doi.org/10.5670/oceanog.2017.213.

Johnson, G. C. and Zhang, D., 2003: Structure of the Atlantic Ocean Equatorial Deep Jets. *Journal of Physical Oceanography*, 33, 600–609, https://doi.org/10.1175/1520-0485(2003)033<0600:sotaoe>2.0.co;2.

Johnson, G. C., Kunze, E., McTaggart, K. E., and Moore, D. W., 2002: Temporal and Spatial Structure of the Equatorial Deep Jets in the Pacific Ocean. *Journal of Physical Oceanography*, 32, 3396–3407, https://doi.org/10.1175/1520-0485(2002)032<3396:tassot>2.0.co;2.

Joyce, T. M., Frankignoul, C., Yang, J., and Phillips, H. E., 2004: Ocean Response and Feedback to the SST Dipole in the Tropical Atlantic. *Journal of Physical Oceanography*, 34, 2525–2540, https://doi.org/10.1175/jpo2640.1.

Kalnay, E., Kanamitsu, M., Kistler, R., Collins, W., Deaven, D., Gandin, L., Iredell, M., Saha, S., White, G., Woollen, J., Zhu, Y., Chelliah, M., Ebisuzaki, W., Higgins, W., Janowiak, J., Mo, K. C., Ropelewski, C., Wang, J., Leetmaa, A., Reynolds, R., Jenne, R., and Joseph, D., 1996: The NCEP/NCAR 40-Year Reanalysis Project. *Bulletin of the American Meteorological Society*, 77, 437–471, https://doi.org/10.1175/1520-0477(1996)077<0437:TNYRP>2.0.CO;2.

Karstensen, J., Stramma, L., and Visbeck, M., 2008: Oxygen minimum zones in the eastern tropical Atlantic and Pacific oceans. *Progress in Oceanography*, 77, 331–350, https://doi.org/10.1016/j.pocean.2007.05.009.

Kiko, R., Biastoch, A., Brandt, P., Cravatte, S., Hauss, H., Hummels, R., Kriest, I., Marin, F., McDonnell, A. M. P., Oschlies, A., Picheral, M., Schwarzkopf, F. U., Thurnherr, A. M., and Stemmann, L., 2017: Biological and physical influences on marine snowfall at the equator. *Nature Geoscience*, 10, 852–858, https://doi.org/10.1038/ngeo3042.

Kistler, R., Collins, W., Saha, S., White, G., Woollen, J., Kalnay, E., Chelliah, M., Ebisuzaki, W., Kanamitsu, M., Kousky, V., van den Dool, H., Jenne, R., and Fiorino, M., 2001: The NCEP–NCAR 50–Year Reanalysis: Monthly Means CD–ROM and Documentation. *Bulletin of the American Meteorological Society*, 82, 247–267, https://doi.org/10.1175/1520-0477(2001)082<0247:tnnyrm>2.3.co;2.

Kundu, P. K., Cohen, I. M., and Dowling, D. R., 2012: Fluid Mechanics. Academic Press, 5th edn.

Leaman, K. D. and Sanford, T. B., 1975: Vertical Energy Propagation of Inertial Waves: A Vector Spectral Analysis of Velocity Profiles. *Journal of Geophysical Research*, 80, 1975–1978, https://doi.org/10.1029/jc080i015p01975.

Lebedev, K. V., Yoshinari, H., Maximenko, N. A., and Hacker, P. W., 2007: YoMaHa'07: Velocity data assessed from trajectories of Argo floats at parking level and at the sea surface. Tech. Rep. No.4(2), IPRC Technical Note, updated as of July 1, 2020.

Leetmaa, A. and Spain, P. F., 1981: Results from a Velocity Transect Along the Equator from 125 to 159°W. *Journal of Physical Oceanography*, 11, 1030–1033, https://doi.org/10.1175/1520-0485(1981)011<1030:rfavta>2.0.co;2.

Locarnini, R. A., Mishonov, A. V., Baranova, O. K., Boyer, T. P., Zweng, M. M., Garcia, H. E., Reagan, J. R., Seidov, D., Weathers, K. W., Paver, C. R., and Smolyar, I. V., 2019: World Ocean Atlas 2018, Volume 1: Temperature. Tech. rep., NOAA Atlas NESDIS 81, A. Mishonov, Technical Editor.

Lomb, N. R., 1976: Least-squares frequency analysis of unequally spaced data. *Astrophysics and Space Science*, 39, 447–462, https://doi.org/10.1007/bf00648343.

Luyten, J. R. and Swallow, J., 1976: Equatorial undercurrents. *Deep Sea Research and Oceanographic Abstracts*, 23, 999–1001, https://doi.org/10.1016/0011-7471(76)90830-5.

Luyten, J. R., Pedlosky, J., and Stommel, H., 1983: The Ventilated Thermocline. *Journal of Physical Oceanography*, 13, 292–309, https://doi.org/10.1175/1520-0485(1983)013<0292:TVT>2.0.CO;2.

Lübbecke, J. F., Rodríguez-Fonseca, B., Richter, I., Martín-Rey, M., Losada, T., Polo, I., and Keenlyside, N. S., 2018: Equatorial Atlantic variability—Modes, mechanisms, and global teleconnections. *WIREs Climate Change*, 9, https://doi.org/10.1002/wcc.527.

MacLachlan, C., Arribas, A., Peterson, K. A., Maidens, A., Fereday, D., Scaife, A. A., Gordon, M., Vellinga, M., Williams, A., Comer, R. E., Camp, J., Xavier, P., and Madec, G., 2015: Global Seasonal forecast system version 5 (GloSea5): a high-resolution seasonal forecast system. *Quarterly Journal of the Royal Meteorological Society*, 141, 1072–1084, https://doi.org/10.1002/qj.2396.

Madec, G., Bourdallé-Badie, R., Bouttier, P.-A., Bricaud, C., Bruciaferri, D., Calvert, D., Chanut, J., Clementi, E., Coward, A., Delrosso, D., Ethé, C., Flavoni, S., Graham, T., Harle, J., Iovino, D., Lea, D., Lévy, C., Lovato, T., Martin, N., Masson, S., Mocavero, S., Paul, J., Rousset, C., Storkey, D., Storto, A., and Vancoppenolle, M., 2017: NEMO ocean engine. *Notes du Pôle de modélisation de l'Institut Pierre-Simon Laplace (IPSL)*, https://doi.org/10.5281/ZENODO.3248739.

Matthießen, J.-D., 2017: Modelling the Equatorial Deep Jets. Ph.D. thesis, Christian-Albrechts-Universität zu Kiel.

Matthießen, J.-D., Greatbatch, R. J., Brandt, P., Claus, M., and Didwischus, S.-H., 2015: Influence of the equatorial deep jets on the north equatorial countercurrent. *Ocean Dynamics*, 65, 1095–1102, https://doi.org/10.1007/s10236-015-0855-5.

Matthießen, J.-D., Greatbatch, R. J., Claus, M., Ascani, F., and Brandt, P., 2017: The emergence of equatorial deep jets in an idealised primitive equation model: an interpretation in terms of basin modes. *Ocean Dynamics*, 67, 1511–1522, https://doi.org/10.1007/s10236-017-1111-y.

McCreary, J. P., 1984: Equatorial beams. *Journal of Marine Research*, 42, 395–430, https://doi.org/10.1357/002224084788502792.

Ménesguen, C., Hua, B. L., Fruman, M. D., and Schopp, R., 2009: Dynamics of the combined extra-equatorial and equatorial deep jets in the Atlantic. *Journal of Marine Research*, 67, 323–346, https://doi.org/10.1357/002224009789954766.

Ménesguen, C., Delpech, A., Marin, F., Cravatte, S., Schopp, R., and Morel, Y., 2019: Observations and Mechanisms for the Formation of Deep Equatorial and Tropical Circulation. *Earth and Space Science*, 6, 370–386, https://doi.org/10.1029/2018ea000438.

Muench, J., Kunze, E., and Firing, E., 1994: The Potential Vorticity Structure of Equatorial Deep Jets. *Journal of Physical Oceanography*, 24, 418–428, https://doi.org/10.1175/1520-0485(1994)024<0418:tpvsoe>2.0.co;2.

Najjar, R. G., Sarmiento, J. L., and Toggweiler, J. R., 1992: Downward transport and fate of organic matter in the ocean: Simulations with a general circulation model. *Global Biogeochemical Cycles*, 6, 45–76, https://doi.org/10.1029/91gb02718.

Pacanowski, R. C. and Philander, S. G. H., 1981: Parameterization of Vertical Mixing in Numerical Models of Tropical Oceans. *Journal of Physical Oceanography*, 11, 1443–1451, https://doi.org/10.1175/1520-0485(1981)011<1443:povmin>2.0.co;2.

Pedlosky, J., 2002: A Theory of Equatorial Deep Jets. *Journal of Physical Oceanography*, 32, 3551–3561, https://doi.org/10.1175/1520-0485(2002)032<3551:atoedj>2.0.co;2.

Ponte, R. M., Luyten, J., and Richardson, P. L., 1990: Equatorial deep jets in the Atlantic Ocean. *Deep Sea Research Part A. Oceanographic Research Papers*, 37, 711–713, https://doi.org/10.1016/0198-0149(90)90100-a.

Qiu, B., Chen, S., and Sasaki, H., 2013: Generation of the North Equatorial Undercurrent Jets by Triad Baroclinic Rossby Wave Interactions. *Journal of Physical Oceanography*, 43, 2682–2698, https://doi.org/10.1175/jpo-d-13-099.1.

Scargle, J. D., 1982: Studies in astronomical time series analysis. II - Statistical aspects of spectral analysis of unevenly spaced data. *The Astrophysical Journal*, 263, 835, https://doi.org/10.1086/160554.

Schmid, C., Bourlès, B., and Gouriou, Y., 2005: Impact of the equatorial deep jets on estimates of zonal transports in the Atlantic. *Deep Sea Research Part II: Topical Studies in Oceanography*, 52, 409–428, https://doi.org/10.1016/j.dsr2.2004.12.008.

Schopf, P. S., Anderson, D. L. T., and Smith, R., 1981: Beta-dispersion of low-frequency Rossby waves. *Dynamics of Atmospheres and Oceans*, 5, 187–214, https://doi.org/10.1016/0377-0265(81)90011-7.

Schott, F. A., Dengler, M., Brandt, P., Affler, K., Fischer, J., Bourlès, B., Gouriou, Y., Molinari, R. L., and Rhein, M., 2003: The zonal currents and transports at 35°W in the tropical Atlantic. *Geophysical Research Letters*, 30, https://doi.org/10.1029/2002gl016849.

Stramma, L., Visbeck, M., Brandt, P., Tanhua, T., and Wallace, D., 2009: Deoxygenation in the oxygen minimum zone of the eastern tropical North Atlantic. *Geophysical Research Letters*, 36, https://doi.org/10.1029/2009gl039593.

Talley, L. D., Pickard, G. L., Emery, W. J., and Swift, J. H., 2011: Descriptive Physical Oceanography: An Introduction. Academic Press.

Tuchen, F. P., Brandt, P., Claus, M., and Hummels, R., 2018: Deep Intraseasonal Variability in the Central Equatorial Atlantic. *Journal of Physical Oceanography*, 48, 2851–2865, https://doi.org/10.1175/jpo-d-18-0059.1.

von Schuckmann, K., Brandt, P., and Eden, C., 2008: Generation of tropical instability waves in the Atlantic Ocean. *Journal of Geophysical Research*, 113, https://doi.org/10.1029/2007jc004712.

Weisberg, R. H. and Weingartner, T. J., 1988: Instability Waves in the Equatorial Atlantic Ocean. *Journal of Physical Oceanography*, 18, 1641–1657, https://doi.org/10.1175/1520-0485(1988)018<1641:iwitea>2.0.co;2.

Youngs, M. K. and Johnson, G. C., 2015: Basin-Wavelength Equatorial Deep Jet Signals across Three Oceans. *Journal of Physical Oceanography*, 45, 2134–2148, https://doi.org/10.1175/jpo-d-14-0181.1.

Zweng, M., Reagan, J., Seidov, D., Boyer, T., Locarnini, R., Garcia, H., Mishonov, A., Baranova, O., Weathers, K., Paver, C., and Smolyar, I., 2019: World Ocean Atlas 2018,Volume 2: Salinity. techreport 82, NOAA Atlas NESDIS, A. Mishonov, Technical Editor.

Acknowledgements

Finally, a big thank you to Michi for always being there for me!

Erklärung

Die vorliegende Abhandlung ist – abgesehen von der Beratung durch meinen Betreuer – in Inhalt und Form meine eigene, nur mit den angegebenen Hilfsmitteln verfasste Arbeit. Diese Arbeit hat noch keiner anderen Stelle im Rahmen eines Prüfungsverfahrens vorgelegen, weder ganz noch zum Teil. Teile dieser Arbeit sind, wie im Text gekennzeichnet, schon in Fachzeitschriften veröffentlicht bzw. zur Veröffentlichung eingereicht. Diese Arbeit ist unter Einhaltung der Regeln guter wissenschaftlicher Praxis der Deutschen Forschungsgemeinschaft entstanden. Mir wurde noch kein akademischer Grad entzogen.

13.09.2021, Swantje Bastin